

A study of the influence of vorticity, capillarity and slope angle on the properties of shoaling and breaking waves

Maria Bjørnestad

Thesis for the degree of Philosophiae Doctor (PhD)
University of Bergen, Norway
2021

UNIVERSITY OF BERGEN



A study of the influence of vorticity, capillarity and slope angle on the properties of shoaling and breaking waves

Maria Bjørnstad



Thesis for the degree of Philosophiae Doctor (PhD)
at the University of Bergen

Date of defense: 28.10.2021

© Copyright Maria Bjørnstad

The material in this publication is covered by the provisions of the Copyright Act.

Year: 2021

Title: A study of the influence of vorticity, capillarity and slope angle on the properties of shoaling and breaking waves

Name: Maria Bjørnstad

Print: Skipnes Kommunikasjon / University of Bergen

Preface

This dissertation is submitted as a partial fulfillment of the requirements for the degree of Doctor of Philosophy (PhD) in Applied Mathematics at the Department of Mathematics, University of Bergen. The scientific work in the thesis have been conducted under the supervision of Professor Henrik Kalisch and Professor Guttorm Alendal at the Department of Mathematics at the University of Bergen, Norway.

The observations of Paper C were obtained at Stemmevika at the west coast of Norway. The lab work of Paper D was conducted at the laboratory at Department of Civil Engineering, National Chung Hsing University, Taichung 40227, Taiwan, in collaboration with Professor Chang Lin. The field campaign of Paper F was located of the island of Sylt, Germany, in collaboration with Institute of Coastal Ocean Dynamics, Helmholtz-Zentrum Hereon, 21502 Geesthacht, Germany.

Acknowledgements

I am very grateful that I got the opportunity to be a research fellow at the Department of Mathematics and to be supervised by Prof. Henrik Kalisch. We have had numerous great discussions and a lot of fun, and I really appreciate his patience and curiosity, and that he is encouraging and inspiring.

I would like to say thank you to all the co-authors for interesting conversations and productive collaborations. Especially, to Prof. Lin for generous hospitality and guidance during my stay in Taichung, Taiwan. In addition, Wei Ying Wong, Prof. Yuan and Dr. Kao to take care of me in the city of Taichung and in the laboratory, with all their valuable qualities both professionally and personally. I am also thankful to Prof. Kharif and Prof. Abid for discussions, good ideas and our many visits. Thank very much to Dr. Buckley, Dr. Streßer, Dr. Horstmann who gave me the opportunity to be a part of a field campaign and to learn the essence of field work from their experience.

Thanks to the co-workers at the department for making the social environment at work funny and interesting, and thank you so much for being there when help has been needed. Finally, I could not have done anything in my life without the support and cheering from my friends and family. Forever grateful for them.

Abstract

Fluid motion and wave patterns have fascinated humans for centuries if not millennia. Water waves have been studied out of curiosity such as observing the ripples created by a stone dropped in a pond as well as practical need. Designing a breakwater to shield a harbor from incoming waves and predicting sediment erosion at a beach are typical engineering problems which arise in the protection of the coast, and require advanced knowledge of the underlying wave motion.

One fundamental problem in the study of water waves is the transition of the waves from large or intermediate depth to shallower waters, and the subsequent breaking. While this situation has been studied from various angles by a large number of authors, many issues remain unresolved, and there is not a single mathematical theory which has been found to work generally in all cases that arise.

In the present thesis, we focus on the shoaling of waves on plane slopes in different cases. The properties of these waves are described mathematically and compared with measurements and observations. It is found that if an appropriate model equation is used for the description of the wave properties, then it is possible to obtain good comparisons between these models and laboratory experiments, field measurements and observations. In some cases, shear flows are a dominant factor while in other cases, capillarity or the steepness of the bed slope are the most important features.

In the first three papers, the shallow-water equations on a shoaling beach are considered. Following the method of Carrier and Greenspan (1958), exact solutions are found and compared with field observations (Paper C). The method of Carrier and Greenspan is extended to flows which may include background shear flows such as for example caused by wind set-up and the required return flow at the coast (Paper A, Paper B)

A laboratory study of the run-up of a solitary wave is given in Paper D. These experiments were set to produce a collapsing breaker on a slope of moderate steepness (1:20), and the breaking wave was dominated by capillarity. The flow field under the collapsing breaker is studied, and a qualitative analysis of this flow is explained using the Navier-Stokes equations.

In Paper E, breaking of an undular bore is considered. The KdV equation is used in the context of background shear, and the onset of breaking is found by analyzing the underlying flow field. The results are compared with an experiment conducted

by Favre (1935), and the comparison suggest that the KdV theory may be used to give an approximate prediction of the incipient of wave breaking of the leading wave in the bore.

In paper F, a field campaign is conducted in order to study shoaling waves in the surf zone. Measured Eulerian and Lagrangian orbital velocities are obtained and the correlated relation to wave-by-wave variations in mean-water level, wave height and incipient wave breaking are considered. By using buoyant traces, Lagrangian mass transport at the free surface is studied and it is shown that the KdV equation gives good predictions of the particle motions relative to the mean-water level.

Outline

This thesis is organized in two parts.

Part I contains general background theory on fluid mechanics and shallow-water waves, and some technical aspects which were not detailed in publications.

Part II contains the scientific results and the contribution consists of the following six scientific papers:

- Paper A** M. Bjørnestad and H. Kalisch, *Shallow Water Dynamics on Linear Shear Flows and Plane Beaches*, *Physics of Fluids* **29** (2017), 073602.
- Paper B** M. Bjørnestad, *Run-up of long waves on background shear currents*, *Wave Motion* **96** (2020), 102551.
- Paper C** M. Bjørnestad and H. Kalisch, *Extreme wave runup on a steep coastal profile*, *AIP Advances* **10** (2020), 105205.
- Paper D** M. Bjørnestad, H. Kalisch, M. Abid, C. Kharif and M. Brun, *Wave Breaking in Undular Bores with Shear Flows*. *Water Waves* (2021), 1–18.
- Paper E** W.Y. Wong, M. Bjørnestad, C. Lin, M.J. Kao, H. Kalisch, P. Guyenne, V. Roeber, and J.M. Yuan, *Internal flow properties in a capillary bore*, *Physics of Fluids* **31** (2019), 113602.
- Paper F** M. Bjørnestad, M. Buckley, H. Kalisch, M. Streßer, J. Horstmann, H.G. Frøysa, O.E. Ige, M. Cysewski and R. Carrasco-Alvarez, *Lagrangian Measurements of Orbital Velocities in the Surf Zone*, *Geophysical Research Letters*, revision submitted (2021).

Contents

Preface	iii
Acknowledgements	v
Abstract	vii
Outline	ix
I Background theory	1
1 Introduction	3
1.1 Conservation laws	3
1.2 Potential flow and boundary conditions	5
1.3 Linear waves over a constant depth	6
1.4 Particle paths	7
1.5 Surface tension	8
2 Shallow-water waves	11
2.1 Shallow water theory	11
2.2 Influence of bathymetry	13
2.3 The method of Carrier and Greenspan	14
2.4 Background shear flows	17
2.4.1 Shear flows over a flat seabed	18
2.4.2 Shear flows on a sloping beach	21
2.5 Boussinesq system and the Korteweg-deVries equation	24
3 Velocities in the surf zone	29
3.1 Field campaign	29
3.2 Orbital orange paths	31
3.3 Data analysis	37

II	Included papers	47
A	Shallow water dynamics on linear shear flows and plane beaches	
B	Run-up of long waves on background shear currents	
C	Extreme wave runup on a steep coastal profile	
D	Internal flow properties in a capillary bore	
E	Wave Breaking in Undular Bores with Shear Flows	
F	Lagrangian Measurements of Orbital Velocities in the Surf Zone	

Part I

Background theory

Chapter 1

Introduction

General background theory on surface water waves will be introduced. Conservation laws of mass and momentum will be described, and we will see how different assumptions and boundary conditions will lead to the surface wave problem. Considering linear wave theory, a solution can be found and by that the dispersion relation is obtained. Lastly, brief descriptions of particle paths and surface tension will be given. In this chapter, we will follow the theory written in [21] and [33].

1.1 Conservation laws

The conservation laws of mass and linear momentum are commonly used in descriptions of fluid dynamics. A brief introduction to these principles will be given here. Within a material control volume $V(t)$, the law of conservation of mass states that

$$\frac{d}{dt} \int_{V(t)} \rho dV = 0,$$

where $\rho(\mathbf{x}, t)$ is the fluid density at the position $\mathbf{x} = [x, y, z]$ at time t . If we consider a fixed control volume V , the equation representing conservation of mass is expressed such that the change of mass inside the volume equals the mass flux crossing the boundary surface A , that is

$$\frac{d}{dt} \int_V \rho dV = - \int_A \rho \mathbf{u} \cdot \mathbf{n} dA,$$

where \mathbf{n} is the outward normal vector to the surface A . The vector $\mathbf{u}(\mathbf{x}, t)$ denotes the fluid velocity vector including the components $[u_1, u_2, u_3]$ representing the velocities in x-, y- and z-directions, respectively. Using the Leibniz rule and applying the Gauss divergence theorem, the equation can be rewritten as

$$\int_V \frac{\partial \rho}{\partial t} + \nabla \cdot (\rho \mathbf{u}) dV = 0,$$

and as the integrand must vanish at every point (\mathbf{x}, t) since the volume boundaries can be chosen arbitrary, this equation requires that

$$\frac{\partial \rho}{\partial t} + \nabla \cdot (\rho \mathbf{u}) = 0.$$

With the relation $\nabla \cdot (\rho \mathbf{u}) = \rho \nabla \cdot \mathbf{u} + \mathbf{u} \cdot \nabla \rho$ and the operator $\frac{D}{Dt} = \frac{\partial}{\partial t} + \mathbf{u} \cdot \nabla$, the equation can be written as

$$\frac{1}{\rho} \frac{D\rho}{Dt} + \nabla \cdot \mathbf{u} = 0.$$

By assuming that the density remains constant, for an incompressible fluid the material derivative of the density will be zero and the equation becomes

$$\nabla \cdot \mathbf{u} = 0. \quad (1.1)$$

This equation is called the equation of continuity.

The law of conservation of momentum is based on Newton's second law and states that the rate of change of the momentum in a control volume V equals the sum of the external forces acting on the volume. The momentum equation in integral form is written as

$$\int_V \frac{\partial}{\partial t} (\rho \mathbf{u}) dV + \int_A \rho \mathbf{u} (\mathbf{u} \cdot \mathbf{n}) dA = \int_V \rho \mathbf{g} dV + \int_A \mathbf{F} dA.$$

The terms on the left-hand side represents the rate of change of momentum inside V and the flux of momentum across the material surface A . The external forces are divided into a body force \mathbf{g} per unit mass and a surface force \mathbf{F} per unit area acting on the volume boundary. The vector \mathbf{F} is given by $\mathbf{F} = n_i \cdot \sigma_{ij}$, where σ_{ij} is the stress tensor. This tensor is conveniently divided into a normal stress $-p\delta_{ij}$, where p is the pressure in the fluid and δ_{ij} is the identity matrix, and the shear stress τ_{ij} . Applying the Gauss theorem, the momentum balance becomes

$$\int_V \frac{\partial}{\partial t} (\rho \mathbf{u}) + \nabla \cdot (\rho \mathbf{u} \mathbf{u}) dV = \int_V \rho \mathbf{g} + \nabla \cdot (-p\delta_{ij} + \tau_{ij}) dV.$$

The stress tensor τ_{ij} for a Newtonian fluid is a linear function of $\frac{\partial u_i}{\partial x_j}$, so $\tau_{ij} = 2\mu d_{ij}$ when $d_{ij} = \left(\frac{\partial u_j}{\partial x_i} + \frac{\partial u_i}{\partial x_j} \right)$, see [21] for more details. Note that

$$\frac{\partial}{\partial t} (\rho \mathbf{u}) + \nabla \cdot (\rho \mathbf{u} \mathbf{u}) = \rho \frac{\partial \mathbf{u}}{\partial t} + \mathbf{u} \left[\frac{\partial \rho}{\partial t} + \nabla \cdot (\rho \mathbf{u}) \right] + \rho \mathbf{u} \cdot \nabla \mathbf{u} = \rho \frac{D\mathbf{u}}{Dt},$$

and since the control volume can be chosen arbitrary, the integrand must be zero for every point (\mathbf{x}, t) , that is

$$\rho \frac{D\mathbf{u}}{Dt} = \rho \mathbf{g} - \nabla p + \mu \nabla^2 \mathbf{u}. \quad (1.2)$$

In the above equation the shear stress has been rewritten to the net viscous force as $\mu \nabla^2 \mathbf{u}$ where μ is a coefficient given from the thermodynamic state. The equation is named Navier-Stokes equation for an incompressible Newtonian fluid.

Recall that $\frac{D\mathbf{u}}{Dt} = \frac{\partial\mathbf{u}}{\partial t} + \mathbf{u} \cdot \nabla\mathbf{u}$ is called the total derivative or material derivative, or sometimes called the Lagrangian acceleration. The latter label is due to the second term called convective (or advective) and is the rate of change of \mathbf{u} that occurs as the fluid particles move from one position (\mathbf{x}, t) to another, while the first term is a local rate of change of \mathbf{u} at the position \mathbf{x} .

1.2 Potential flow and boundary conditions

Let us consider surface gravity waves propagating at an air-water interface where the gravity force is the main restoring force. The gravitational field is assumed to be constant and considered to be the only body force acting on the fluid volume. The gravity force is conservative and can be expressed in terms of a potential function as $\mathbf{g} = \nabla\Phi$. With positive z-axis pointing vertically upwards, Φ can be written as $-gz$ where g is the acceleration of gravity. By the assumption of an incompressible and inviscid flow, the conservation of mass and linear momentum can be expressed as (Euler eqs.)

$$\nabla \cdot \mathbf{u} = 0, \quad (1.3)$$

$$\frac{\partial\mathbf{u}}{\partial t} + (\mathbf{u} \cdot \nabla)\mathbf{u} = -\frac{1}{\rho}\nabla p - g\mathbf{k}, \quad (1.4)$$

where \mathbf{k} is the unit vector in the z-direction.

If the flow is irrotational, that is $\text{curl } \mathbf{u} = 0$, the flow velocity vector can be defined as a potential vector as $\mathbf{u} = \nabla\phi$, and equation (1.3) turns into the Laplac's equation $\Delta\phi = 0$. Following the theory in [Stoker, Whitham], integration of eq.(1.4) with respect to \mathbf{x} , leads us to Bernoulli's law:

$$\phi_t + \frac{1}{2}(\nabla\phi)^2 + \frac{p - p_0}{\rho} + gz = C(t), \quad (1.5)$$

where $C(t)$ is an integration constant that is not depending on \mathbf{x} and p_0 is an arbitrary constant different from $C(t)$. Without any essential loss of generality, $C(t)$ may be included in a new potential function and in that way ignored.

Let us define the air-water interface by $f(x, y, z, t) = 0$ and the free surface to be $z = \eta(x, y, t)$, where $\eta(x, y, t)$ denotes the vertical elevation of the free surface. By assuming that the fluid can neither cross or leave the interface, a surface boundary condition can be stated as $(\mathbf{n} \cdot \mathbf{u})_{z=\eta} = \mathbf{n} \cdot \mathbf{U}_{\text{interface}}$, where \mathbf{n} is the surface normal and $\mathbf{U}_{\text{interface}}$ is the velocity of the interface itself which is assumed to be $\mathbf{U}_{\text{interface}} = \eta_t\mathbf{k}$. A second boundary condition at the free surface can be obtained by considering the interface to have no mass, which means that the force in the fluids just above and underneath the surface must be equal. This means that the pressure should be the same on the two sides of the boundary. Note that in the present case the surface tension is neglected. The motion of the air will change the pressure, but the changes are small enough to be neglected and it is therefore reasonable to let the constant p_0 to be the atmospheric pressure. This boundary condition is known as the dynamic

condition. The third boundary condition is located at the bottom which is defined as a solid fixed boundary. The undisturbed water-surface is at $z = 0$ and the distance to the sea bed is defined as $h(x, y)$. No fluid can cross the boundary, and this give us the last condition as $\mathbf{n} \cdot \mathbf{u} = 0$. The three boundary conditions are then given as

$$\eta_t + \phi_x \eta_x + \phi_y \eta_y = \phi_z \quad \text{at } z = \eta(x, y, t), \quad (1.6)$$

$$\phi_t + \frac{1}{2}(\phi_x^2 + \phi_y^2 + \phi_z^2) + g\eta = 0 \quad \text{at } z = \eta(x, y, t), \quad (1.7)$$

$$\phi_z + \phi_x h_x + \phi_y h_y = 0 \quad \text{at } z = -h(x, y). \quad (1.8)$$

1.3 Linear waves over a constant depth

For propagating water waves with the properties of small amplitude, the problem presented in the last section may be linearized in order to obtain a solution of the problem and to derive the dispersion relation. The basis for this limitation is that the wave amplitude a must be much smaller then the wavelength λ , and the quantities of the velocity components, as well as the surface elevation $\eta(x, y, t)$ and their derivatives, should be small.

Let us consider the case where the surface waves propagate in a one-dimensional x-direction only and that the depth is constant denoted by h_0 , see Figure 1.1. The

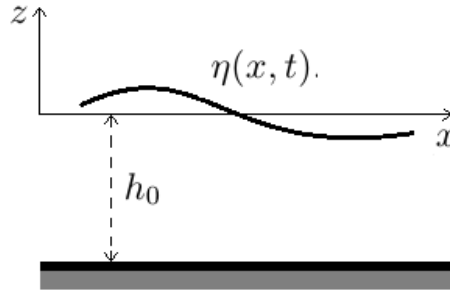


Figure 1.1: Definition sketch the surface elevation $\eta(x, t)$ and the constant water depth h_0 .

Laplace equation and the boundary condition (1.8) are already linear equations if the bottom is uniform. The two boundary conditions at the free surface can be linearized by neglecting the non-linear terms to obtain $\eta_t = \phi_z$ and $\phi_t + g\eta = 0$ at $z = \eta(x, t)$. Combining these to equations, $\eta(x, t)$ can be eliminated and the linear problem becomes

$$\phi_{xx} + \phi_{zz} = 0 \quad \text{at } z = -h_0 < z < 0, \quad (1.9)$$

$$\phi_{tt} + g\phi_z = 0 \quad \text{at } z = 0, \quad (1.10)$$

$$\phi_z = 0 \quad \text{at } z = -h_0, \quad (1.11)$$

where the free surface boundary conditions are applied at $z = 0$ rather than at $z = \eta(x, t)$. Even with linear boundary conditions, this problem is not fully defined without an appropriate initial condition for the surface shape. According to [21], it is reasonable to choose a sinusoidal wave with the amplitude a and with phase $(kx - \omega t)$, where k is the wave number and ω is the angular frequency. Along with the boundary condition, this choice of the surface as $\eta = a \cos(kx - \omega t)$ leads to a velocity potential with a separated solution in the form

$$\phi = Z(z) \sin(kx - \omega t).$$

Substitution of the expression for ϕ into the Laplace equation gives us $Z'' - k^2 Z = 0$, and due to the linearized free surface boundary conditions and (1.11), the coefficient is given by

$$Z(z) = \frac{a\omega}{k} \frac{\cosh k(z + h_0)}{\sinh kh_0}.$$

With the obtained potential function, the velocity components are found by $\mathbf{u} = \nabla\phi$, as

$$u = a\omega \frac{\cosh k(z + h_0)}{\sinh kh_0} \cos(kx - \omega t), \quad (1.12)$$

$$w = a\omega \frac{\sinh k(z + h_0)}{\sinh kh_0} \sin(kx - \omega t). \quad (1.13)$$

The remaining boundary condition (1.10) together with the expressions for η and ϕ defines the angular frequency ω as a function of the wave number k as

$$\omega^2 = gk \tanh(kh_0).$$

This equation is called the dispersion relation. Recall that $k = 2\pi/\lambda$, where λ is the wavelength, and that the phase speed is defined by $c = \omega/k$. In terms of the phase speed, the dispersion relation can be rewritten as

$$c = \sqrt{\frac{g}{k} \tanh(kh_0)}, \quad (1.14)$$

and this relation shows that the phase speed depends on the wavelength $\lambda = \frac{2\pi}{k}$ i.e., the waves are dispersive.

1.4 Particle paths

In general, the water particles move in orbitals when a surface gravity wave passes. The Lagrangian coordinates are based on the movement of a fluid particle and should be used in this description. As an initial condition at $t = 0$, let (x_0, z_0) be a particle position when the particle is at rest, and let the functions $\xi(t)$ and $\zeta(t)$ be the x- and z-coordinate, respectively. Each path is identified by the center of the orbit (x_0, z_0) , and the path is in Lagrangian form as $\xi(x_0, z_0, t)$ and $\zeta(x_0, z_0, t)$. The position of

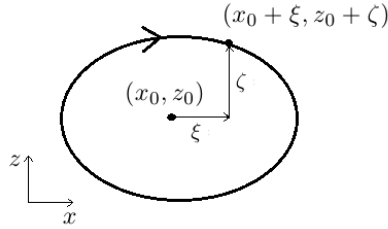


Figure 1.2: Definition sketch of an orbital particle path whose the average position is (x_0, z_0) and the $\xi(t)$ and $\zeta(t)$ is the time-dependent displacement.

a fluid particle is then given by $(x_0 + \xi, z_0 + \zeta)$, see Figure 1.2, and the velocity components of the particle is given by the differential equations

$$\begin{aligned}\frac{\partial \xi}{\partial t} &= u(\xi(t), \zeta(t), t), \\ \frac{\partial \zeta}{\partial t} &= w(\xi(t), \zeta(t), t).\end{aligned}$$

In the case of linear waves described in the last section, the particle excursion (ξ, ζ) is small when the amplitude is much smaller than the wavelength, and the Lagrangian velocity is nearly equal to the fluid velocity at the average position (x_0, z_0) at that instant. In this case, the velocity components are approximated by $\frac{\partial \xi}{\partial t} = u(x_0, z_0, t)$ and $\frac{\partial \zeta}{\partial t} = w(x_0, z_0, t)$. Integrating (1.12) and (1.13) in time, the particle position is

$$\begin{aligned}\xi &= -a \frac{\cosh k(z_0 + h_0)}{\sinh kh_0} \sin(kx_0 - \omega t), \\ \zeta &= a \frac{\sinh k(z_0 + h_0)}{\sinh kh_0} \cos(kx_0 - \omega t).\end{aligned}$$

Combining these two equations by the elimination of $(kx_0 - \omega t)$, gives us an equation representing an ellipse, written as

$$\frac{\xi^2}{\left[a \frac{\cosh k(z_0 + h_0)}{\sinh kh_0} \right]^2} + \frac{\zeta^2}{\left[a \frac{\sinh k(z_0 + h_0)}{\sinh kh_0} \right]^2} = 1.$$

1.5 Surface tension

So far surface tension has been neglected. In this section, surface tension is considered as an additional restoring force. Wave where the shape of the free surface and the fluid velocity field are affected by the capillary effects are called capillary waves. The surface tension τ is the tensile force per unit length of a line on the interface and depends on the temperature and the fluids content, see [21]. With a nonzero surface tension, there will be a pressure difference (or a jump) across the curved

interface. The pressure difference, at the surface is $p_{z=\eta} - p_0$ where $p_{z=\eta}$ denotes the pressure just inside the interface and p_0 is the atmospheric pressure. From the force balance, it is found that the pressure difference is equal to the curvature times the surface tension parameter τ . By definition the curvature at one point at some

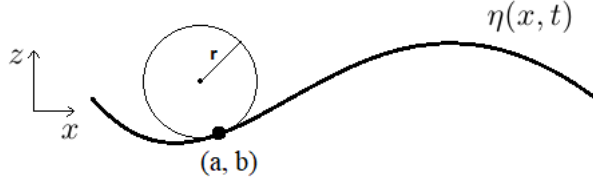


Figure 1.3: A drawing of the free surface elevation $\eta(x, t)$ and a circle with radius r which is tangential to the point (a, b) at the surface to illustrate a definition of the curvature as $1/r$.

continuous curve is $1/r$ where r is the radius of a circle that is tangential to that point, see Figure 1.3. Considering a free surface $\eta(x, t)$, the curvature $1/r$ is given by the definition

$$\frac{1}{r} = \frac{\frac{\partial^2 \eta}{\partial x^2}}{\left[1 + \left(\frac{\partial \eta}{\partial x}\right)^2\right]^{3/2}},$$

and the pressure difference can be expressed as

$$p_0 - p_{z=\eta} = \tau \frac{\frac{\partial^2 \eta}{\partial x^2}}{\left[1 + \left(\frac{\partial \eta}{\partial x}\right)^2\right]^{3/2}}.$$

In the case where the slope $\partial\eta/\partial x$ is small, the dispersion relation can be found by changing the dynamic boundary condition according to the pressure balance in the above equation. Setting p_0 to be zero together with the assumption of linear waves, the pressure becomes $p = -\tau\partial^2\eta/\partial x^2$ at $z = 0$. Using a linear version of the Bernoulli equation (1.5), the dynamic condition turns into

$$\frac{\partial\phi}{\partial t} = \frac{\tau}{\rho} \frac{\partial^2 \eta}{\partial x^2} - g\eta \quad \text{at } z = 0.$$

Following the same steps as in Section 1.3, the dispersion relation is found to be

$$\omega = \left(k \left(g + \frac{\sigma k^2}{\rho}\right) \tanh kh_0\right)^{1/2}.$$

Chapter 2

Shallow-water waves

In order to use mathematical modelling for predictions and understanding of water waves properties, we often make assumptions. In the present work, we focus on shallow-water waves where shallow-water theory and Boussinesq theory are used. The shallow-water theory results in hyperbolic equations [22] and is suitable for the studying of non-dispersive long waves. The Boussinesq theory is a better approach when the waves are a bit shorter and the dispersion effects are more dominant, see [38].

In this chapter we initially outline the shallow water theory where the shallow-water equations are derived from the Benney equations. Using the control volume approach, the shallow-water equations with the inclusion of non-uniform bathymetry will be derived, and a description of how Carrier and Greenspan [19] manage to solve these equations will be given. The inclusion of background shear flows over a flat bed and a sloping beach are described and we will see how the Riemann invariant can be obtained. The Boussinesq theory and the KdV equation are the focus in the last section in this chapter.

2.1 Shallow water theory

In the theory of nonlinear long waves in shallow water, following the theory in [21, 33], the wavelength λ is assumed to be much larger than the undisturbed water depth h_0 , see [21]. That is, a wave is regarded as a shallow-water wave if $\frac{\lambda}{h_0} \gg 1$, or equivalent written in terms of the wave number $k = \frac{2\pi}{\lambda}$ as $kh_0 \rightarrow 0$. With this assumption, the dispersion relation found by applying linear wave theory indicates that the equation (1.14) reduces to $c = \sqrt{gh_0}$ which shows that the waves are non-dispersive. As explained in [26, 33], combining nonlinear theory with the long wave assumption, the propagation speed is assumed to be $c = \sqrt{g(h_0 + \eta)}$, where $\eta(x, t)$ is the free-surface elevation.

In order to derive the shallow-water equations we start with the case of two-dimensional flows over a constant depth. If no assumptions are made, the Euler

equations (1.3) and (1.4) can be written as

$$\begin{aligned} u_x + w_z &= 0, \\ \frac{Du}{Dt} &= u_t + uu_x + wu_z = -\frac{1}{\rho}p_x, \\ \frac{Dw}{Dt} &= w_t + uw_x + ww_z = -\frac{1}{\rho}p_z - g, \end{aligned}$$

where the velocity components are $u(x, z, t)$ and $w(x, z, t)$, the pressure is denoted $p(x, z, t)$ and g is the constant of gravity. The shallow-water approximation entails the assumption that the vertical acceleration is small compared to the horizontal acceleration. Thus, the material derivative of w can be neglected and the vertical component of the momentum balance becomes

$$-\frac{1}{\rho}p_z - g = 0.$$

By integrating from z to η with respect to z implies the hydrostatic law

$$p - p_0 = \rho g(\eta - z), \quad (2.1)$$

which agrees with the dynamic boundary condition at the free surface. Excluding the pressure from the horizontal momentum equation, gives us the following system of equations:

$$u_x + w_z = 0, \quad (2.2)$$

$$u_t + uu_x + wu_z + g\eta_x = 0. \quad (2.3)$$

As explained in [25], the free surface boundary condition can be used to arrive at the Benney equations from equation (2.2) and (2.3). Recall Figure 1.1 where the water equilibrium is located at $z = 0$ and that there is a constant depth h_0 . The surface boundary condition stating that $(\mathbf{n} \cdot \mathbf{u})_{z=\eta} = \mathbf{n} \cdot \mathbf{U}_{\text{interface}}$. With the defined air-water interface $f(x, z, t) = \eta(x, t) - z$, where $\eta(x, t)$ is the surface elevation, the boundary condition at $z = \eta(x, t)$ can be written as $w = \eta_t + \eta_x u$. Using this boundary condition and integrating equation (2.2) over the water depth, that is from $-h_0$ to $\eta(x, t)$ with respect to z , the first Benney equation is obtained as

$$\eta_t + \frac{\partial}{\partial x} \int_{-h_0}^{\eta} u \, dz = 0.$$

The second Benney equation is the same as equation (2.3), and the third is obtained by a combination of the integration $\int_{-h_0}^z u_x + w_z \, dz = 0$ and the bottom boundary condition. At $z = -h_0$ the vertical velocity component equals zero and the integral equation becomes

$$w = - \int_{-h_0}^z u_x \, dz.$$

Note that these Benney equations are also called shallow-water equations for shear flows since the velocity components are depending on both x and z . By assuming that the horizontal velocity is independent of z , the Benney equations are reduced to the classical shallow-water equations

$$\begin{aligned}\eta_t + [u(\eta + h_0)]_x &= 0, \\ u_t + uu_x + g\eta_x &= 0.\end{aligned}$$

2.2 Influence of bathymetry

The shallow-water equations on non-uniform bathymetry will be derived by using the control volume approach directly. This derivation is based on the detailed description in [10]. Consider long waves propagating towards the beach only in the x -direction. The sloping beach is given by $b(x)$ and the total water depth is $H(x, t) = \eta(x, t) + h(x)$, where $\eta(x, t)$ is the surface elevation and $h(x) = -b(x)$ is the undisturbed water depth where the x -axis is located at the undisturbed level, see Figure 2.1. The

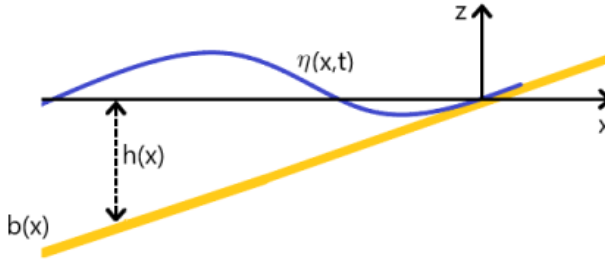


Figure 2.1: A sketch for illustration of the surface elevation $\eta(x, t)$ on the sloping beach denoted $b(x)$ when $b(x) = -\alpha x$, where $z = 0$ at the undisturbed level and $h(x)$ is the undisturbed water depth.

flow is considered to be irrotational, inviscid, homogeneous and incompressible, and the flow velocity in the x -direction is $u = u(x, t)$. The control volume is given by constant width $\int dy = B$, height from $-h(x)$ to $\eta(x, t)$ and the interval between x_1 and x_2 . Similar to the previous chapter, the conservation of mass written in integral form is

$$\frac{d}{dt} \int_{x_1}^{x_2} \int_{-h}^{\eta} \rho B dz dx + \left[\int_{-h}^{\eta} \rho u(x, t) B dz \right]_{x_1}^{x_2} = 0,$$

where ρ denotes the constant density. As before, since the boundaries x_1 and x_2 are arbitrary, and the integrand must vanish at every point (x, z, t) , the above equation turns into

$$\eta_t + [u(\eta + h)]_x = 0. \quad (2.4)$$

In integral form, the conservation law of linear momentum can be written as

$$\begin{aligned} \frac{d}{dt} \int_{x_1}^{x_2} \int_{-h}^{\eta} \rho u B \, dx dz + \left[\int_{-h}^{\eta} \rho u^2 B \, dz \right]_{x_1}^{x_2} + \left[\int_{-h}^{\eta} \rho g(\eta - z) B \, dz \right]_{x_1}^{x_2} \\ = - \int_{x_1}^{x_2} b_x \rho g(\eta + h) B \, dx, \end{aligned}$$

where the first two terms are the change of momentum with respect to time and the flux of momentum through the interval. The third term represents the pressure force where the pressure is assumed to be hydrostatic and the term on the right-hand side is the bottom force. With an inclined bottom profile, there will be a pressure from the seabed into the flow in the negative x-direction which opposes the flow. Again, since the interval between x_1 and x_2 is arbitrary, the momentum balance equation can be written in differential form as

$$(uH)_t + (u^2 H)_x + \left(\frac{1}{2}gH^2\right)_x = -b_x gH.$$

Rewriting the above equation using equation (2.4) gives us the second shallow-water equation:

$$u_t + uu_x + g\eta_x = 0. \quad (2.5)$$

2.3 The method of Carrier and Greenspan

Carrier and Greenspan (1958), obtained explicit solutions to the non-linear shallow-water equations on a uniform sloping beach. In this section, a brief description will be given of their methodology [19] of how to reduce the two non-linear equations to one linear equation which can be solved exactly. The sloping beach will from now on be defined as $b(x) = \alpha x$. The balance equations of mass and momentum found in the last section are

$$\begin{aligned} \eta_t + [u(\eta + h)]_x &= 0, \\ u_t + uu_x + g\eta_x &= 0, \end{aligned}$$

and we will see how these are transformed into a linear equation. Initially, the non-linear shallow-water equations are converted into non-dimensional equations by substituting the non-dimensional variables $u^* = \frac{u}{u_0}$, $\eta^* = \frac{\eta}{\alpha l_0}$, $h^* = \frac{h}{\alpha l_0}$, $x^* = \frac{x}{l_0}$ and $t^* = \frac{t}{T}$, where $T = \sqrt{l_0/\alpha g}$, $u_0 = \sqrt{gl_0\alpha}$ and the l_0 is a characteristic length. By this scaling, the equations become

$$u_{t^*}^* + u^* u_{x^*}^* + \eta_{x^*}^* = 0, \quad (2.6)$$

$$\eta_{t^*}^* + [u^*(\eta^* - x^*)]_{x^*} = 0. \quad (2.7)$$

The first step in the Carrier and Greenspan methodology is the important step to rewrite these equations in characteristic form. In order to do that, it is convenient

to use the expression to the phase speed $c = \sqrt{g(\eta + h)}$ which was found in the combination of non-linear theory and the shallow-water approximation. The phase speed is assumed to be $c \neq 0$ and the non-dimensional variable is given by $c^* = c/u_0$. The equations can now be written in terms of $u(x, t)$ and $c(x, t)$ as

$$\begin{aligned}u_t + uu_x + 2cc_x + 1 &= 0, \\2c_t + cu_x + 2uc_x &= 0,\end{aligned}$$

where the stars for simplicity have been disregarded and will continue to be from now on. This substitution is a good choice since one c was eliminated from the latter equation. With this system of equations, the characteristics form can be obtained by adding and subtracting the two equations, resulting in

$$\left\{ \frac{\partial}{\partial t} + (u + c) \frac{\partial}{\partial x} \right\} (u + 2c + t) = 0, \quad (2.8)$$

$$\left\{ \frac{\partial}{\partial t} + (u - c) \frac{\partial}{\partial x} \right\} (u - 2c + t) = 0. \quad (2.9)$$

The above equations can be seen in the view of the method of characteristic, see for example [1, 26, 32], and can be expressed as

$$\begin{cases} u + 2c + t = \text{constant along curves } C^+ : \frac{dx}{dt} = u + c \\ u - 2c + t = \text{constant along curves } C^- : \frac{dx}{dt} = u - c. \end{cases}$$

To make sense of this, let us consider a curve C^+ and that this curve satisfies $\frac{dx}{dt} = u + c$ in the (x, t) -plane. The material derivative of the function $u + 2c + t$ along this curve is

$$\frac{D}{Dt}(u + 2c + t) = \frac{\partial}{\partial t}(u + 2c + t) + (u + c) \frac{\partial}{\partial x}(u + 2c + t),$$

and by consulting eq.(2.8), we see that $\frac{D}{Dt}(u + 2c + t) = 0$. This function $u + 2c + t$ is called Riemann invariant and must remain constant at every point along the characteristic curve C^+ which satisfies the characteristics speed $\frac{dx}{dt} = u + c$. Equation (2.9) have the same properties. There will be a set of characteristic curves where C^+ and C^- are distinct since $c \neq 0$. The Riemann invariants can be chosen to be equal any arbitrary function as long as it is constant along the characteristic curves, so

$$\begin{aligned}\alpha &= u + 2c + t, \\ -\beta &= u - 2c + t,\end{aligned}$$

where α and β are named characteristics variables.

In order to reduce the non-linear equations (2.8) and (2.9) to a linear system of equations, a convenient tool is the hodograph transformation, which is to invert the roles of the independent variables with the dependent variables. For a two-by-two systems of non-linear equation written in the form $\mathbf{u}_t + \mathbf{f}(\mathbf{u})_x = \mathbf{0}$, where $\mathbf{u} = [\eta, u]^T$

and with a Jacobian matrix only depending on \mathbf{u} , the system is reducible, and a hodograph transformation will resolve it to a linear system of equations. However, in the case presented here, reviewing equation (2.6) and (2.7), the Jacobian matrix is depending on both \mathbf{u} and x . Therefore, an explicit hodograph transformation will not reduce the system. As an alternative, Carrier and Greenspan did the transformation using the characteristics variables as the dependent variables instead of $\eta(x, t)$ and $c(x, t)$. That is to transform $\alpha = \alpha(x, t)$ and $\beta = \beta(x, t)$ to $x = x(\alpha, \beta)$ and $t = t(\alpha, \beta)$, and the Jacobian $\frac{\partial(x, t)}{\partial(\alpha, \beta)}$ should be nonzero. Applying this proper hodograph transformation on our system of equation, leads to

$$\begin{aligned}x_\beta - (u + c)t_\beta &= 0, \\x_\alpha - (u - c)t_\alpha &= 0.\end{aligned}$$

By rewriting them in terms of the characteristic variables, we can see that the equations still are non-linear in t . An addition step is required in order to obtain linearity. In order to do a change of variables, we define new independent variables as

$$\begin{aligned}\alpha - \beta &= \lambda, \\ \alpha + \beta &= \sigma,\end{aligned}$$

and with some calculations, the system of equations become

$$x_\sigma - ut_\sigma + ct_\lambda = 0, \tag{2.10}$$

$$x_\lambda + ct_\sigma - ut_\lambda = 0. \tag{2.11}$$

Using the relations $u + t = \frac{\lambda}{2}$ and $c = \frac{\sigma}{4}$, reveals that the equations are non-linear because of the terms ut_σ and ut_λ . However, by assuming that $x(\sigma, \lambda)$ and $t(\sigma, \lambda)$ are smooth functions, which means that $x_{\sigma\lambda} = x_{\lambda\sigma}$ and $t_{\sigma\lambda} = t_{\lambda\sigma}$, and by differentiating the equation (2.10) and (2.11), the obtained equation is

$$u_\lambda t_\sigma - u_\sigma t_\lambda - c_\lambda t_\lambda + c_\sigma t_\sigma = c(t_{\lambda\lambda} - t_{\sigma\sigma}),$$

where x has been eliminated. Once again, using the relations $u + t = \frac{\lambda}{2}$ and $c = \frac{\sigma}{4}$, the equation is written in linear form as

$$\sigma(t_{\lambda\lambda} - t_{\sigma\sigma}) - 3t_\sigma = 0.$$

This is a linear second-order differential equation, and it can be solved for $t(\sigma, \lambda)$ by the method of separation of variables. However, it would not be easy to find a solution of $x(\sigma, \lambda)$ since only the differentiated functions of x are appearing in the equations (2.10) and (2.11). Therefore, in order to deal with this difficulty, rewriting the equation in terms of $u(\sigma, \lambda)$ as

$$\sigma(u_{\sigma\sigma} - u_{\lambda\lambda}) + 3u_\sigma = 0,$$

for then to introduce a potential function

$$u(\sigma, \lambda) = \frac{1}{\sigma} \phi_\sigma(\sigma, \lambda),$$

gives us the equation

$$(\sigma \phi_\sigma)_\sigma - \sigma \phi_{\lambda\lambda} = 0.$$

The solution of $\phi(\sigma, \lambda)$ can be found by the method of separation, and with this potential function at hand, integration of equation (2.10) gives us an expression of $x(\sigma, \lambda)$ written as

$$x = \frac{\phi_\lambda}{4} - \frac{\sigma^2}{16} - \frac{u^2}{2}.$$

The remaining variables are then given by

$$u = \frac{1}{\sigma} \phi_\sigma, \quad \eta = \frac{\phi_\lambda}{4} - \frac{u^2}{2}, \quad t = \frac{\lambda}{2} - u.$$

Various improvements of the method have been provided [4, 5, 23, 29] since the work done by Carrier and Greenspan in 1958.

2.4 Background shear flows

So far the flow has been assumed to be irrotational. Near shore there might be a wind blowing towards the coast, underlying currents will be created [37] and there will be a required return flow [34] which might be in the form of an undertow. This was just one example of a creation of underlying currents, but currents can occur in numerous ways and such shear currents have an influence on the wave properties. If the waves are long compared to the water depth, it is reasonable to use a shear profile that is linear [36] and that the current is unaffected by the wave motion. In this way, the choice of constant vorticity may give a good description of the influence on wave dynamics [2, 35] and it simplifies the mathematical problems.

In the previous section we saw how Carrier and Greenspan first found the Riemann invariants and then used these to carry out a hodograph transformation. In this section we will elaborate on the problem by finding the Riemann invariants when a background shear flow is present. This is written in Paper A, but in this section we intend to give a more in depth description. First the case of water waves propagating over a flat seabed will be considered. A description on how the Riemann invariants can be obtained when a shear flow is present over a flat bed will be shown in detail. Then the case where the waves propagating towards a sloping beach over a shear current is presented, and we will see how the Riemann invariants are obtained with the advantage of the flat seabed scenario. Lastly, brief explanation on how the analogy to the gas dynamics equations can be used to obtain the Riemann invariants when both shear flow and sloping beach are included in the shallow-water equations.

2.4.1 Shear flows over a flat seabed

Consider long waves propagating over a flat seabed where a background linear shear current is present. The x-axis is placed at the sea bottom and water depth is defined as $H(x, t) = \eta(x, t) + h_0$, where $\eta(x, t)$ is the surface excursion and h_0 is the constant undisturbed depth. The waves are only travelling in the x-direction and the flow is considered to be homogeneous, inviscid and incompressible. Let us use the expression $-\Gamma_0 + \Gamma_1 z$, where $-\Gamma_0$ and Γ_1 are constants, to describe a background shear flow with a constant clockwise vorticity. In the x-direction, the velocity component will then consist of the depth average flow $u(x, t)$ and the uniform shear flow described as $-\Gamma_0 + \Gamma_1 z$. Including this new expression of the horizontal velocity component, the shallow-water equation with the presents of shear flow over a flat bed can be derived in a similar way as in the last section, providing

$$\begin{aligned} H_t + \left(-\Gamma_0 H + \frac{\Gamma_1}{2} H^2 + uH \right)_x &= 0, \\ u_t + \left(-\Gamma_0 u + \frac{1}{2} u^2 + gH \right)_x &= 0. \end{aligned}$$

Note that in the case of flat bed there is no need to include a bottom force in the momentum balance. The equations can be written in non-dimensional form in line of non-dimensional variables $u^* = \frac{u}{u_0}$, $\eta^* = \frac{\eta}{h_0}$, $x^* = \frac{x}{h_0}$, $t^* = \frac{t}{T}$, $\Gamma_0^* = \frac{\Gamma_0}{u_0}$, $\Gamma_1^* = \frac{\Gamma_1}{1/T}$, where $T = \sqrt{h_0/g}$ and $u_0 = \sqrt{gh_0}$, as non-dimensional form

$$H_{t^*}^* + \left(-\Gamma_0^* H^* + \frac{\Gamma_1^*}{2} H^{*2} + u^* H^* \right)_{x^*} = 0, \quad (2.12)$$

$$u_{t^*}^* + \left(-\Gamma_0^* u^* + \frac{1}{2} u^{*2} + H^* \right)_{x^*} = 0. \quad (2.13)$$

As in the last section where the Carrier and Greenspan methodology was followed, let us substitute the phase speed $c = \sqrt{gH}$ with the non-dimensional variable $c^* = \frac{c}{u_0}$ into the equations. By adding and subtracting the two equations, gives

$$\left\{ \frac{\partial}{\partial t} + (u - \Gamma_0 + c) \frac{\partial}{\partial x} \right\} (u + 2c) = -2\Gamma_1 c^2 c_x, \quad (2.14)$$

$$\left\{ \frac{\partial}{\partial t} + (u - \Gamma_0 - c) \frac{\partial}{\partial x} \right\} (u - 2c) = 2\Gamma_1 c^2 c_x. \quad (2.15)$$

The stars will be omitted from now on. The above equations are not written in characteristic form since the term $2\Gamma_1 c^2 c_x$ is not included in the structure on the left-hand side. With this term incorporated, the Riemann invariants could have been found directly, but in this case, it is a dead end.

By defining $\mathbf{u} = [u_1, u_2]^T = [H, u]^T$, the equation (2.12) and (2.13) can be rewritten as

$$\mathbf{u}_t + \mathbf{f}(\mathbf{u})_x = \mathbf{0}, \quad (2.16)$$

and with the relation $\mathbf{f}(\mathbf{u})_x = \mathbf{f}'(\mathbf{u})\mathbf{u}_x$, the Jacobian is found to be

$$\mathbf{f}'(\mathbf{u}) = \begin{bmatrix} -\Gamma_0 + \Gamma_1 u_1 + u_2 & u_1 \\ 1 & -\Gamma_0 + u_2 \end{bmatrix}.$$

We can see that this non-linear system is reducible since the Jacobian only depends on \mathbf{u} . As stated in [1, 22], the Riemann invariants exists since the system is reducible. In order to find the Riemann invariants, we will follow the theory in [1, 22]. Assume that the Jacobian has eigenvalues ξ_i , where $i = 1, 2$, with the corresponding eigenvectors \mathbf{r}_i which is linear independent, then $\mathbf{f}'(\mathbf{u})\mathbf{r}_i = \xi_i\mathbf{r}_i$. With the matrix $\mathbf{R} = [\mathbf{r}_1, \mathbf{r}_2]$, and the diagonal matrix $\mathbf{\Lambda}$ whose diagonal elements are the two corresponding eigenvalues, the right eigenproblem can be written as $\mathbf{f}'(\mathbf{u})\mathbf{R} = \mathbf{R}\mathbf{\Lambda}$. First the eigenvalues of the Jacobian are obtained by the characteristic polynomial $\det((\mathbf{f}'(\mathbf{u}) - \xi\mathbf{I})) = 0$ and there after the eigenvectors are found by the equation $\mathbf{f}'(\mathbf{u})\mathbf{r}_i = \xi_i\mathbf{r}_i$. The eigenvalues are

$$\begin{aligned} \xi_1 &= u_2 - \Gamma_0 + \frac{1}{2}\Gamma_1 u_1 + \frac{1}{2}\sqrt{(\Gamma_1 u_1)^2 + 4u_1}, \\ \xi_2 &= u_2 - \Gamma_0 + \frac{1}{2}\Gamma_1 u_1 - \frac{1}{2}\sqrt{(\Gamma_1 u_1)^2 + 4u_1}, \end{aligned}$$

and the corresponding eigenvectors are

$$\begin{aligned} \mathbf{r}_1 &= \begin{bmatrix} \Gamma_1 u_1 + \frac{1}{2}\sqrt{(\Gamma_1 u_1)^2 + 4u_1} \\ 2 \end{bmatrix}, \\ \mathbf{r}_2 &= \begin{bmatrix} \Gamma_1 u_1 - \frac{1}{2}\sqrt{(\Gamma_1 u_1)^2 + 4u_1} \\ 2 \end{bmatrix}. \end{aligned}$$

Note that the system of equations is strictly hyperbolic since the eigenvalues are real and distinct. Since the determinant of the matrix \mathbf{R} is nonzero, the inverse of \mathbf{R} exists [27] and by multiplying with \mathbf{R}^{-1} , the left eigenproblem appears as $\mathbf{R}^{-1}\mathbf{f}'(\mathbf{u}) = \mathbf{\Lambda}\mathbf{R}^{-1}$. If we define a matrix \mathbf{L} such as

$$\mathbf{R}^{-1} = \mathbf{L} = \begin{bmatrix} \mathbf{l}_1^T \\ \mathbf{l}_2^T \end{bmatrix},$$

the matrix equation becomes $\mathbf{L}\mathbf{f}'(\mathbf{u}) = \mathbf{\Lambda}\mathbf{L}$. The inverse matrix of \mathbf{R} is

$$\mathbf{R}^{-1} = \frac{1}{\sqrt{(\Gamma_1 u_1)^2 + 4u_1}} \begin{bmatrix} 2 & -\Gamma_1 u_1 + \frac{1}{2}\sqrt{(\Gamma_1 u_1)^2 + 4u_1} \\ -2 & \Gamma_1 u_1 + \frac{1}{2}\sqrt{(\Gamma_1 u_1)^2 + 4u_1} \end{bmatrix},$$

which means that the left eigenvectors are

$$\begin{aligned} \mathbf{l}_1 &= \begin{bmatrix} 2 \\ -\Gamma_1 u_1 + \frac{1}{2}\sqrt{(\Gamma_1 u_1)^2 + 4u_1} \end{bmatrix}, \\ \mathbf{l}_2 &= \begin{bmatrix} 2 \\ -\Gamma_1 u_1 - \frac{1}{2}\sqrt{(\Gamma_1 u_1)^2 + 4u_1} \end{bmatrix}. \end{aligned}$$

The corresponding left eigenproblem written in index notation is $\mathbf{l}_i^T \mathbf{f}'(\mathbf{u}) = \xi_i \mathbf{l}_i^T$, and by multiplying equation (2.16) by \mathbf{l}_i^T , it becomes

$$\mathbf{l}_i^T \mathbf{u}_t + \xi_i \mathbf{l}_i^T \mathbf{u}_x = \mathbf{0}. \quad (2.17)$$

We want to write this equation in characteristic form. For such a purpose, we introduce an auxiliary function $\mu(\mathbf{u})$ that satisfies

$$\nabla \omega_i(\mathbf{u}) = \left[\frac{\partial \omega_i}{\partial u_1}, \quad \frac{\partial \omega_i}{\partial u_2} \right] = \mu_i(\mathbf{u}) \mathbf{l}_i^T. \quad (2.18)$$

In this way, equation (2.17) becomes

$$\nabla \omega_i(\mathbf{u}) \mathbf{u}_t + \xi_i \nabla \omega_i(\mathbf{u}) \mathbf{u}_x = 0,$$

which can be written in characteristic form as

$$\left\{ \frac{\partial}{\partial t} + \xi_i \frac{\partial}{\partial x} \right\} \omega_i(\mathbf{u}) = 0.$$

Recall that with the equation written in this form, ξ_i is the characteristic speed and the function $\omega_i(\mathbf{u})$ is the Riemann invariant. At this point, the stage is set to find the two Riemann invariant ω_1 and ω_2 , nevertheless it is not straight forward. Let us first concentrate on finding the first one. By the equation (2.18), we have that

$$\frac{\partial \omega_1}{\partial u_1} = \mu_1(\mathbf{u}) 2, \quad (2.19)$$

$$\frac{\partial \omega_1}{\partial u_2} = \mu_1(\mathbf{u}) \left(-\Gamma_1 u_1 + \frac{1}{2} \sqrt{(\Gamma_1 u_1)^2 + 4u_1} \right). \quad (2.20)$$

The problem here is that we do not know what $\mu_1(\mathbf{u})$ is nor the derivatives of ω_1 . In order to handle this difficulty, we assume that the second order partial derivatives of $\omega_i(\mathbf{u})$ exist and are continuous functions for every $u_1, u_2 \in \mathbb{R}$, such that

$$\frac{\partial^2 \omega_i}{\partial u_1 \partial u_2} = \frac{\partial^2 \omega_i}{\partial u_2 \partial u_1}. \quad (2.21)$$

The auxiliary function $\mu_1(\mathbf{u})$ must satisfy this relation, and with some consideration we choose it to be

$$\mu_1(\mathbf{u}) = \Gamma_1 + \frac{1}{u_1} \sqrt{(\Gamma_1 u_1)^2 + 4u_1}.$$

With this particular function, equation (2.19) and (2.20) can be written as

$$\begin{aligned} \frac{\partial \omega_1}{\partial u_1} &= 2\left(\Gamma_1 + \frac{1}{u_1} \sqrt{(\Gamma_1 u_1)^2 + 4u_1}\right), \\ \frac{\partial \omega_1}{\partial u_2} &= 4, \end{aligned}$$

and we can see that the required relation in equation (2.21) is fulfilled. Integrating these two equations, we obtain

$$\omega_1 = 2\Gamma_1 u_1 + 2\sqrt{(\Gamma_1 u_1)^2 + 4u_1} + \frac{8}{\Gamma_1} \sinh^{-1} \left(\frac{\Gamma_1 \sqrt{u_1}}{2} \right) + K(u_2)$$

$$\omega_1 = 4u_2 + K(u_1),$$

where $K(u_2)$ and $K(u_1)$ are the constants of integration, and from this we can see that the first Riemann invariant can be as following

$$\omega_1 = u_2 - \Gamma_0 + \frac{1}{2}\Gamma_1 u_1 + \frac{1}{2}\sqrt{(\Gamma_1 u_1)^2 + 4u_1} + \frac{2}{\Gamma_1} \sinh^{-1} \left(\frac{\Gamma_1 \sqrt{u_1}}{2} \right).$$

Here, adjustment as dividing by 4 and subtracting Γ_0 have been done to simplify later work. By choosing $\mu_2(\mathbf{u})$ as

$$\mu_2(\mathbf{u}) = \Gamma_1 - \frac{1}{u_1} \sqrt{(\Gamma_1 u_1)^2 + 4u_1},$$

we can proceed in a similar way to find $\omega_2(\mathbf{u})$, and that gives

$$\omega_2 = u_2 - \Gamma_0 + \frac{1}{2}\Gamma_1 u_1 - \frac{1}{2}\sqrt{(\Gamma_1 u_1)^2 + 4u_1} - \frac{2}{\Gamma_1} \sinh^{-1} \left(\frac{\Gamma_1 \sqrt{u_1}}{2} \right).$$

To summarize, instead of the pre-characteristic structure in equation (2.14) and (2.15), we are now able to write the equations in characteristic form as

$$\begin{cases} \frac{\partial}{\partial t} + \xi_1 \frac{\partial}{\partial x} \end{cases} \omega_1 = 0,$$

$$\begin{cases} \frac{\partial}{\partial t} + \xi_2 \frac{\partial}{\partial x} \end{cases} \omega_2 = 0,$$

where the characteristic speed are

$$\xi_1 = u - \Gamma_0 + \frac{1}{2}\Gamma_1 H + \frac{1}{2}\sqrt{(\Gamma_1 H)^2 + 4H},$$

$$\xi_2 = u - \Gamma_0 + \frac{1}{2}\Gamma_1 H - \frac{1}{2}\sqrt{(\Gamma_1 H)^2 + 4H},$$

and the Riemann invariants are

$$\omega_1 = u - \Gamma_0 + \frac{1}{2}\Gamma_1 H + \frac{1}{2}\sqrt{(\Gamma_1 H)^2 + 4H} + \frac{2}{\Gamma_1} \sinh^{-1} \left(\frac{\Gamma_1 \sqrt{H}}{2} \right), \quad (2.22)$$

$$\omega_2 = u - \Gamma_0 + \frac{1}{2}\Gamma_1 H - \frac{1}{2}\sqrt{(\Gamma_1 H)^2 + 4H} - \frac{2}{\Gamma_1} \sinh^{-1} \left(\frac{\Gamma_1 \sqrt{H}}{2} \right). \quad (2.23)$$

2.4.2 Shear flows on a sloping beach

Let us consider long waves propagating towards a uniform beach profile just as described in Section 2.2 and illustrated in Figure 2.1. In addition, a linear background

shear current is present and is presented as $U(x, z) = \Gamma_1 \left(\frac{h}{2} + z \right)$ with Γ_1 as a constant. The horizontal velocity component is $V(x, z, t) = U(x, z) + u(x, t)$, where $u(x, t)$ is the average depth flow velocity. We will derive the shallow-water equation using the control volume approach and the volume width, height and length are the same as in Section 2.2. The equation of conservation of mass is then

$$\frac{d}{dt} \int_{x_1}^{x_2} H(x, t) dx + \left[\int_{-h(x)}^{\eta(x, t)} V(x, z, t) dz \right]_{x_1}^{x_2} = 0,$$

where $H(x, t) = \eta(x, t) + h(x)$ is the total depth and $h(x) = -\alpha x$ is the undisturbed depth. As before, the interval boundaries x_1 and x_2 can be chosen arbitrary and therefore the integrand must vanish at every point and the equation becomes

$$\eta_t + \left(\frac{\Gamma_1}{2} \eta (h + \eta) + uH \right)_x = 0. \quad (2.24)$$

The only force that is action on the volume is the hydrostatic pressure force and the bottom force, so, the momentum balance equation in integral form is

$$\begin{aligned} \frac{d}{dt} \int_{x_1}^{x_2} \int_{-h}^{\eta} V dz dx + \left[\int_{-h}^{\eta} V^2 dz \right]_{x_1}^{x_2} + \left[\int_{-h}^{\eta} g(\eta - z) dz \right]_{x_1}^{x_2} \\ = - \int_{x_1}^{x_2} \alpha g(\eta + h) dx. \end{aligned}$$

Since the integrand that must vanish pointwise and with some calculations, the equation reads

$$\begin{aligned} \left(\frac{\Gamma_1}{2} (h\eta + \eta^2) + uH \right)_t \\ + \Gamma_1^2 \left(\frac{h^2}{4} H + \frac{h}{2} (\eta^2 - h^2) + \frac{1}{3} (\eta^3 + h^3) \right)_x \\ + \Gamma_1 \left((hH + \eta^2 - h^2) u + u^2 H + \frac{g}{2} H^2 \right)_x \\ = -\alpha g H. \end{aligned}$$

Before continuing, this equation can be simplified using equation (2.24) to removing terms. That is, removing the terms given by $\frac{\Gamma_1}{2} h$ times equation (2.24) and following it up doing the same with the factors u and $\Gamma_1 \eta$. This leads to

$$u_t + \left(\frac{\Gamma_1}{2} h \left(\frac{\Gamma_1}{4} h - u \right) + \frac{u^2}{2} + g\eta \right)_x = 0$$

Nondimensionalizing the two equations using the non-dimensional variables $u^* = \frac{u}{u_0}$, $\eta^* = \frac{\eta}{\alpha l_0}$, $x^* = \frac{x}{l_0}$, $t^* = \frac{t}{T}$, $\Gamma_1^* = \frac{\Gamma_1}{1/T}$, where $T = \sqrt{l_0/\alpha g}$, $u_0 = \sqrt{g l_0 \alpha}$ and l_0 is a characteristic length, gives

$$\eta_{t^*}^* + \left(\frac{\alpha \Gamma_1^*}{2} \eta^* (\eta^* - x^*) + u^* (\eta^* - x^*) \right)_{x^*} = 0, \quad (2.25)$$

$$u_{t^*}^* + \left(\frac{\alpha \Gamma_1^*}{2} x^* \left(u^* + \frac{\alpha \Gamma_1^*}{4} x^* \right) + \frac{u^{*2}}{2} + \eta^* \right)_{x^*} = 0. \quad (2.26)$$

To simplify the reading, the stars will be omitted in the following. Inserting the dimensionless phase speed $c = \sqrt{(\eta - x)}$ into the equations prior to adding and subtracting the two equations, we obtain

$$\left\{ \frac{\partial}{\partial t} + \left(u + \frac{\alpha\Gamma_1}{2}x + c \right) \frac{\partial}{\partial x} \right\} \left(u + \frac{\alpha\Gamma_1}{2}x + 2c + t \right) = -2\alpha\Gamma_1 c^2 c_x, \quad (2.27)$$

$$\left\{ \frac{\partial}{\partial t} + \left(u + \frac{\alpha\Gamma_1}{2}x - c \right) \frac{\partial}{\partial x} \right\} \left(u + \frac{\alpha\Gamma_1}{2}x - 2c + t \right) = 2\alpha\Gamma_1 c^2 c_x. \quad (2.28)$$

Here, we have the same situation as in the flat bed case. The term $2\alpha\Gamma_1 c^2 c_x$ on the left-hand side are not included in the structure on the right-hand side, and it is not easy to see how that could be done. This means that the equations are not in characteristic form and the Riemann invariants are not found. In the attempt to do so, we go back to equation (2.25) and (2.26) and rewrite them as the vector equation $\mathbf{u}_t + \mathbf{f}(\mathbf{u}, x)_x = \mathbf{0}$ where $\mathbf{u} = [\eta, u]^T$. As have been considered before, the Jacobian matrix $\mathbf{f}'(\mathbf{u}, x)$ is depending on both \mathbf{u} and x , which means that the system of equations is non-reducible. Recall that a hodograph transformation would not transform the system into a linear system if it was non-reducible. In addition, it is not clear that the Riemann invariants will exist in this case. On the other hand, the eigenvalues to Jacobian matrix $\mathbf{f}'(\mathbf{u}, x)$ is found to be

$$\begin{aligned} \xi_1 &= u + \frac{\alpha\Gamma_1}{2} (x + c^2) + \frac{c}{2} \sqrt{(\alpha\Gamma_1 c)^2 + 4}, \\ \xi_2 &= u + \frac{\alpha\Gamma_1}{2} (x + c^2) - \frac{c}{2} \sqrt{(\alpha\Gamma_1 c)^2 + 4}. \end{aligned}$$

Therefore at this point, let us start by studying and comparing the pre-characteristic form of equations (2.14) and (2.15) in the flat bed case with the equations (2.27) and (2.28) in the present case. In addition, with the similarities of the known eigenvalues in both cases, the Riemann invariants found in the flat bed case are setting the stage to do a qualified guess on how the Riemann invariants could be defined in the present case. We choose them to be

$$\begin{aligned} \omega_1 &= u + \frac{\alpha\Gamma_1}{2} (x + c^2) + \frac{1}{2} c \sqrt{(\alpha\Gamma_1 c)^2 + 4} + \frac{2}{\alpha\Gamma_1} \sinh^{-1} \left(\frac{\alpha\Gamma_1 c}{2} \right) + t, \\ \omega_2 &= u + \frac{\alpha\Gamma_1}{2} (x + c^2) - \frac{1}{2} c \sqrt{(\alpha\Gamma_1 c)^2 + 4} - \frac{2}{\alpha\Gamma_1} \sinh^{-1} \left(\frac{\alpha\Gamma_1 c}{2} \right) + t. \end{aligned}$$

In order to check if this choice will fit the characteristic form, we start by writing the left-hand side of

$$\begin{aligned} \left\{ \frac{\partial}{\partial t} + \xi_1 \frac{\partial}{\partial x} \right\} \omega_1 &= 0, \\ \left\{ \frac{\partial}{\partial t} + \xi_2 \frac{\partial}{\partial x} \right\} \omega_2 &= 0. \end{aligned}$$

To see that both equations are equal to zero, we rearrange the equations such that we can use the equations (2.25) and (2.26) to cancel out every term in the equations. In this way we know that ω_1 and ω_2 are Riemann invariants to our system of equations.

An exact solution to these non-linear equations is obtained in Paper A, and the shoaling process and the combined effect of α and Γ_1 are discussed. To be able to separate this combined effect obtained in Paper A, we tackled the same scenario with a different angle. Deriving the Benney equations in the context of constant vorticity, the equations could be written in the standard form of barotropic gas dynamics. With this analogy, the difficulty of finding the Riemann invariants could be overcome in a more general way. With an exact solution obtained, a separate study of the slope angle and the constant vorticity is presented. Going back to assuming irrotational flow, in Paper C an exact solution is compared with observations done in the field.

2.5 Boussinesq system and the Korteweg-deVries equation

In order to derive the KdV equation, we go back to the case of irrotational flow so that a velocity potential exists which satisfies the Laplace equation

$$\phi_{xx} + \phi_{zz} = 0. \quad (2.29)$$

where z now measures the vertical distance from the flat bottom and $\phi_z = 0$ at $z = 0$. The following derivation is based on [38]. The velocity potential is expanded in an asymptotic series as

$$\phi = \sum_{n=0}^{\infty} z^n f_n(x, t). \quad (2.30)$$

We then substitute equation (2.30) into equation (2.29):

$$\sum_{n=0}^{\infty} z^n \frac{\partial^2 f_n(x, t)}{\partial x^2} + \sum_{n=2}^{\infty} n(n-1)z^{n-2} f_n(x, t) = 0. \quad (2.31)$$

Equation (2.31) is rewritten by factoring out z^n and rearranging the summation, gives us

$$\sum_{n=0}^{\infty} z^n \left[\frac{\partial^2 f_n(x, t)}{\partial x^2} + (n+2)(n+1)f_{n+2}(x, t) \right] = 0.$$

Then we obtain the relation

$$f_{n+2} = \frac{-1}{(n+2)(n+1)} \frac{\partial^2 f_n}{\partial x^2}.$$

The solution to this relation function is

$$\begin{aligned} f_{2n} &= \frac{-1}{2n(2n-1)} \frac{\partial^2 f_{2n-2}}{\partial x^2} \\ &= \frac{-1}{2n(2n-1)} \frac{\partial^2}{\partial x^2} \left(\frac{-1}{(2n-2)(2n-3)} \frac{\partial^2 f_{2n-4}}{\partial x^2} \right) \\ &= \frac{1}{2n(2n-1)(2n-2)(2n-3)} \frac{\partial^4 f_{2n-4}}{\partial x^4} = \dots = \frac{(-1)^n}{(2n)!} \frac{\partial^{2n} f_0}{\partial x^{2n}}, \end{aligned}$$

where only the even terms are kept due to the boundary conditions at the flat bed. Then, equation (2.30) appears in the form

$$\phi = \sum_{n=0}^{\infty} (-1)^n \frac{z^{2n}}{(2n)!} \frac{\partial^{2n} f}{\partial x^{2n}}, \quad (2.32)$$

where $f = f_0$. We then substitute into the free surface boundary conditions. First, the variables are normalized in the following way

$$x' = lx, \quad z' = h_0 z, \quad t' = \frac{lt}{c_0}, \quad \eta' = a\eta, \quad \phi' = \frac{gla\phi}{c_0}.$$

Note that the original variables are primed. By introducing the dimensionless parameters $\alpha = a/h_0$ and $\beta = h_0^2/l^2$, the Laplace equation then becomes

$$\beta \frac{\partial^2 \phi}{\partial x^2} + \frac{\partial^2 \phi}{\partial z^2} = 0,$$

and the boundary conditions are transformed into

$$\begin{aligned} \phi_z &= 0, \quad z = 0, \\ \eta_t + \alpha \phi_x \eta_x - \frac{1}{\beta} \phi_z &= 0, \quad Y = 1 + \alpha\eta, \\ \eta + \phi_t + \frac{1}{2} \alpha \phi_x^2 + \frac{1}{2} \frac{\alpha}{\beta} \phi_z^2 &= 0, \quad Y = 1 + \alpha\eta. \end{aligned}$$

Rewriting the expansion for ϕ in non-dimensional variables gives

$$\phi = \sum_{n=0}^{\infty} (-1)^n \frac{z^{2n}}{(2n)!} \frac{\partial^{2n} f}{\partial x^{2n}} \beta^n.$$

This expression is substituted into the first boundary condition and we see that

$$\begin{aligned} \eta_t + \alpha \frac{\partial}{\partial x} \left(\sum_{n=0}^{\infty} (-1)^n \frac{z^{2n}}{(2n)!} \frac{\partial^{2n} f}{\partial x^{2n}} \beta^n \right) \eta_x - \frac{1}{\beta} \frac{\partial}{\partial z} \left(\sum_{n=0}^{\infty} (-1)^n \frac{z^{2n}}{(2n)!} \frac{\partial^{2n} f}{\partial x^{2n}} \beta^n \right) \\ = \eta_t + \alpha \left(\sum_{n=0}^{\infty} (-1)^n \frac{z^{2n}}{(2n)!} \frac{\partial^{2n+1} f}{\partial x^{2n+1}} \beta^n \right) \eta_x - \frac{1}{\beta} \left(\sum_{n=1}^{\infty} (-1)^n \frac{z^{2n-1}}{(2n-1)!} \frac{\partial^{2n} f}{\partial x^{2n}} \beta^n \right) = 0. \end{aligned}$$

That leads to

$$\eta_t + \left((1 + \alpha\eta) f_x \right)_x - \left[\frac{1}{6} (1 + \alpha\eta)^3 f_{xxx} + \frac{1}{2} \alpha (1 + \alpha\eta)^2 f_{xx} \eta_x \right] \beta + \mathcal{O}(\beta^2) = 0, \quad (2.33)$$

and the dynamic boundary condition becomes

$$\eta + f_t + \frac{1}{2} \alpha f_x^2 - \frac{1}{2} (1 + \alpha\eta)^2 \left[f_{xxt} + \alpha f_x f_{xxx} - \alpha f_{xx}^2 \right] \beta + \mathcal{O}(\beta^2) = 0. \quad (2.34)$$

All terms of $\mathcal{O}(\beta)$ for equation (2.33) and equation (2.34) are kept, but terms of $\mathcal{O}(\alpha\beta)$ are omitted. The dynamic boundary condition is differentiated with respect

to x . We obtain the Boussinesq equations in the form

$$\begin{aligned}\eta_t + [(1 + \alpha\eta)w]_x + \mathcal{O}(\alpha\beta, \beta^2) &= 0, \\ w_t + \alpha w w_x + \eta_x - \frac{1}{2}\beta w_{xxt} + \mathcal{O}(\alpha\beta, \beta^2) &= 0,\end{aligned}\tag{2.35}$$

where $w = f_x$ is the first term in the expansion of the horizontal velocity. By just keeping the lowest order terms of equation (2.35), we obtain

$$\begin{aligned}\eta_t + w_x + \mathcal{O}(\alpha, \beta) &= 0, \\ w_t + \eta_x + \mathcal{O}(\alpha, \beta) &= 0.\end{aligned}$$

The KdV-equation is uni-directional equal, and we are only interested in the right-going solutions which satisfies

$$w = \eta, \quad \eta_t + \eta_x = 0.$$

A solution of (2.35) to first order in α and β has the form

$$w = \eta + \alpha A + \beta B + \mathcal{O}(\alpha^2 + \beta^2),$$

where A and B are functions of η and various derivatives. Inserting into equation (2.35) yields

$$\begin{aligned}\eta_t + \eta_x + \alpha[A_x + 2\eta\eta_x] + \beta[B_x - \frac{1}{6}\eta_{xxx}] + \mathcal{O}(\alpha^2 + \beta^2) &= 0, \\ \eta_t + \eta_x + \alpha[A_t + \eta\eta_x] + \beta[B_t - \frac{1}{2}\eta_{xxt}] + \mathcal{O}(\alpha^2 + \beta^2) &= 0.\end{aligned}$$

The two equations are consistent only if $A = -\frac{1}{4}\eta^2$ and $B = \frac{1}{3}\eta_{xx}$. Inserting into the upper equation gives the Korteweg-deVries equation

$$\eta_t + \eta_x + \frac{3}{2}\alpha\eta\eta_x + \frac{1}{6}\beta\eta_{xxx} + \mathcal{O}(\alpha^2 + \beta^2) = 0.$$

In dimensional form the equation is

$$\eta_t + c_0\eta_x + \frac{3}{2}\frac{c_0}{h_0}\eta\eta_x + \frac{1}{6}h_0^2\eta_{xxx} = 0.$$

Nondimensionalizing in a different way, where h_0 is the unit of distance and $\sqrt{\frac{h_0}{g}}$ is the unit of time, gives the normalized KdV equation

$$\eta_t + \eta_x + \frac{3}{2}\eta\eta_x + \frac{1}{6}\eta_{xxx} = 0.$$

In Paper E, we consider the incipient of breaking of a travelling undular bore such as initiated in [9, 17]. A comparison between the laboratory study conducted by Favre [24] and the KdV equation in the context of shear flows is presented. In particular, the inclusion of vorticity leads to an improvement in the comparison. The

derivation of the KdV equation with the inclusion of a linear shear and the exact solitary wave solution are given in [30]. Assuming irrotational flows, with exact numerical solutions of the KdV equation, the velocity field can be found as in [3], and particle path can be computed as shown in [16]. This is used in Paper F to make comparisons between Lagrangian particle path measured in the field and numerical particle paths estimated by the KdV equation, as well as the velocity in the fluid column. Numerical Boussinesq theory [28] was also used in Paper D in order to do a comparison with the features of a collapsing breaker.

Chapter 3

Velocities in the surf zone

A field campaign was conducted in September 2019 at a beach on the island of Sylt located north-west in Germany. In this section a more detailed description of the design and experimental procedure as well as the post processes and data analysis will be given. The purpose of initiating a field campaign at a beach was to study orbital velocities of buoyant tracers at the free surface and the flow velocities down in the water column. The goal was to figure out how the cross-shore mass transport in the surf zone is related to wave-by-wave variations in mean-water level, set-down and wave groups [8, 18, 20] We also looked at the influence of the wave height and incipient wave breaking on mass transport.

3.1 Field campaign

Together with a team from Institute of Coastal Ocean Dynamics at Geesthacht in Germany (see [12] or Paper F for more details), a field campaign was organized and completed in September 2019. Several measurements and footage were obtained, therefore in order to get an overview of what was done, a brief explanation is as follows.

When it was low tide at the beach, we mounted an array of 6 vertical poles down into the sand where the direction of the array was pointing towards the wave direction of incoming waves. Pole 1 was placed about 80 m away from the shoreline while pole 6 was placed about 20 m away from shore, see left image in Figure 3.1. At those poles, pressure gauges were attached close to the seabed. The reason to measure the pressure in the fluid was to gain data in order to extract the free surface elevation at a later stage in the process. At pole 2, in addition to the pressure gage, an Acoustic Doppler Velocimeter (ADV) was mounted to measure the Eulerian flow velocities in the water column.

The main focus of the field campaign was to be able to track buoyant surface tracers in order to construct 3D orbital paths. In our opinion, oranges were a good choice of tracers because of their physical properties and they are naturally biodegradable.



Figure 3.1: Left image: Shows six poles which are planted in the sand and lined up in the direction of the incoming waves. There is also a person holding a checkerboard as a calibration target to the stereo calibration. Right image: This image is to illustrate the ridge behind the beach and the distance from the shoreline. There is a person at the beach to illustrate the distance to the cameras. In the lower right corner, a part of the camera lens is displayed pointing in the direction of the field of view which is approximately 150 m from the camera. The sea conditions shown in the image were not ideal.

To locate the oranges and track their motion, two cameras were placed at the about 20 m high ridge behind the beach, see right image in Figure 3.1, and with 35 m in between one another to establish a two-camera stereo imaging system. Such as describe in [6, 7] where stereo observations of the wave motions were the described, we primarily used the stereo system to locating the oranges. The pair of cameras were pointing in the direction of the three most seaward poles and the field of views (FOVs) were approximately 150 m from the location of the cameras. The two cameras were triggered simultaneously and were acquired at 30 frames/second. In this way, when the wave field conditions in the surf zone were suitable for our approach, a swimmer employed oranges within the FOVs, and the stereo system could resolve their surface motion. In addition to tracing the oranges, the stereo camera system could also be used as an optical pole wave gauge at each pole in the FOVs.

To get more information on the field conditions and locations of different measurements, GPS measurements were done of the sloping beach and of almost all positions of the experimental set-up. A drone was also employed and gave us a valued overview of the beach and surf zone area. Supplementary, before we arrived Sylt, a buoy had been placed about 1km offshore to provide measurements of significant wave height, peak period and peak direction. For more details about the names, type and properties of different apparatuses, see [12] (Paper F).



Figure 3.2: This is a single photo captured by the north camera (Camera 2) placed to the right on top of the ridge behind the beach. The five outermost poles can be seen together with three floating oranges. Two of the oranges are located to the left of pole 2, while one orange is located on top of the wave between pole 1 and pole 2.

3.2 Orbital orange paths

With footage of oranges floating around at the wavy water surface 150 m from the cameras, see Figure 3.2 and Figure 3.3, the process to obtain cross-shore orbital paths will be described in this section. It is a detailed and time-consuming process,

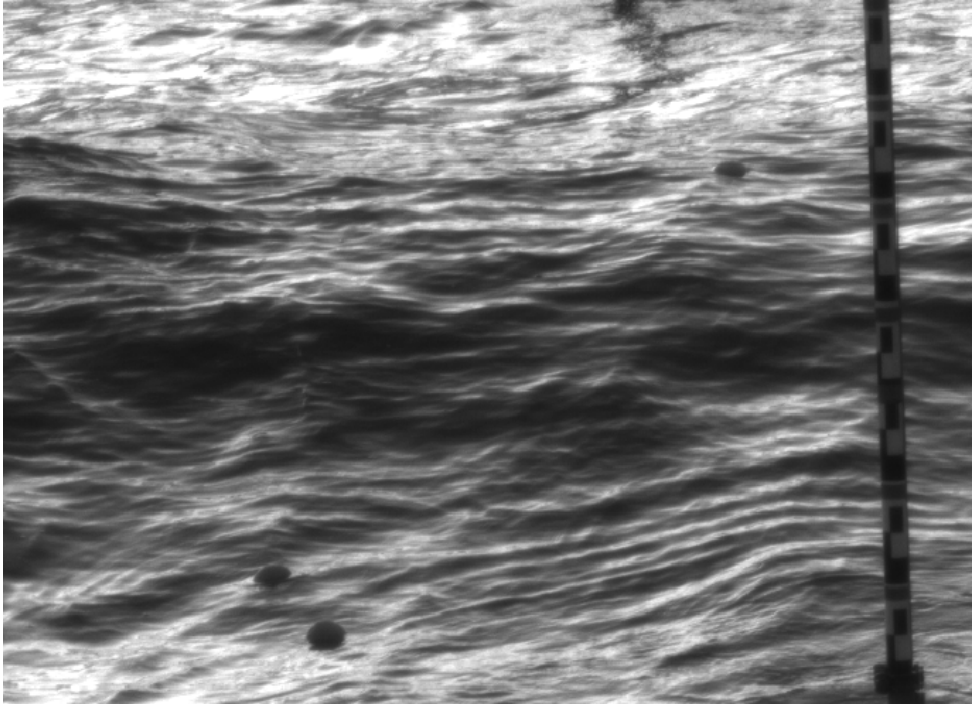


Figure 3.3: To get a better view of the three oranges in Figure 3.2 a zoomed in version is shown here. Also pole 2 is displayed and the attached pattern is visible.

therefore the focus here is to give a short explanation to every step in the process.

The first step is to calibrate the stereo imaging system. While the cameras were positioned and mounted as during the recording of tracers, images of a checkerboard pattern as a calibration target were captured. At low tide, a checkerboard was carried around in different angles covering both FOVs simultaneously, see Figure 3.4. A selected sub-sample from this footage were then used as an input to the MATLAB toolbox named Stereo Camera Calibrator [31]. With an appropriate collection of frames, the toolbox provides a calculation of the intrinsic and extrinsic parameters to both cameras. Along with the extrinsic parameters, a 3D world-coordinate system is defined to have the origin at Camera 1 (the camera to the south) with the x-axis pointing towards Camera 2 (the camera to the north).

On the left side in Figure 3.4, there is a column with some of the pair of frames used in the calibration. Adding or removing different frames with a variation of angles, focus and positions of the checkerboard could either improve or weaken the calibration results. Therefore, to obtain the best result possible, after new images were added or removed, the calibration result was examined. As an initial consideration of the calibration results, as seen to the left in Figure 3.5, due to the extrinsic parameters one could inspect the relative positions of the checkerboard locations

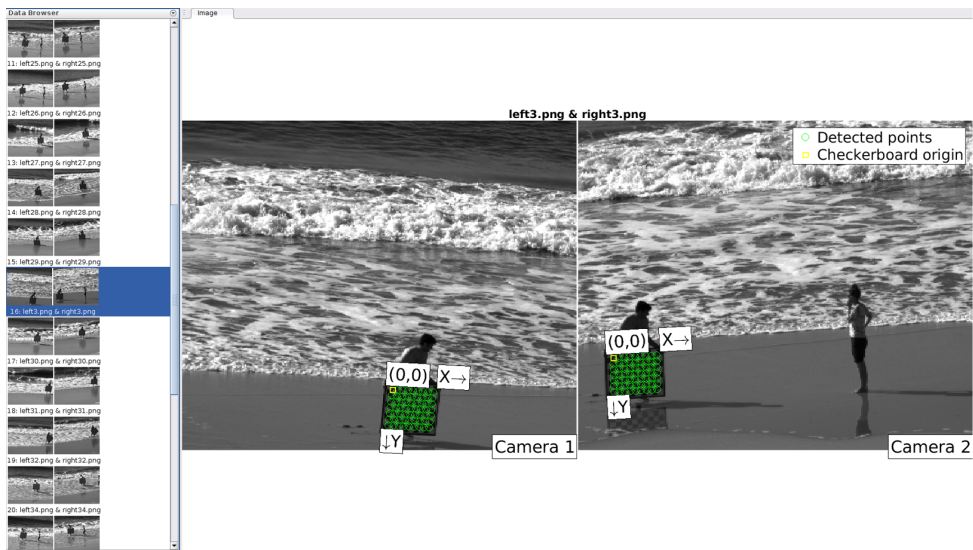


Figure 3.4: A pair of frames taken at the same time stamp by the south camera (Camera 1) and the north camera (Camera 2). The checkerboard had to be carried around covering the frames while it at the same time stayed in both FOVs. To the left, a column of image pair used in the calibration is shown. The green color shows detected points as a part of the calibration procedure.

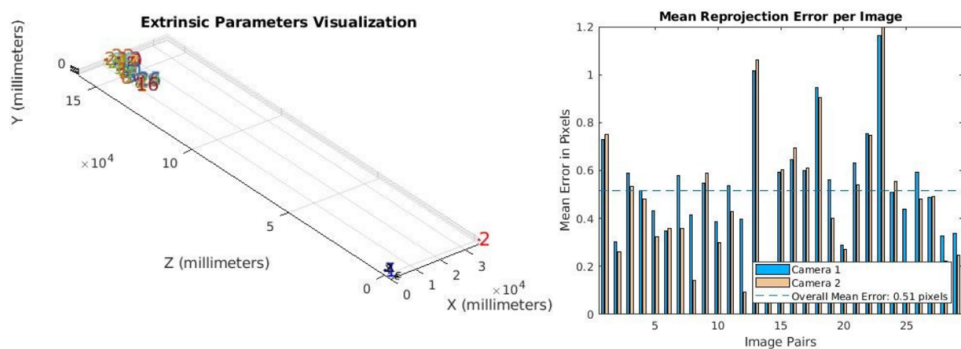


Figure 3.5: Left panel: A visualization of the positions of the two cameras and all the checkerboard locations. Right panel: A bar graph shows the mean reprojection error per image pair, and the dashed horizontal line is the overall mean error. Note, only a sub-sample of 30 image pair are displayed.

and the two cameras to see if it matches the expectations. The right panel in Figure 3.5 shows the reprojection errors in pixels for each image pair and an overall mean error. The reprojection error is the distance between a detected point of a corner at the checkerboard (see the green pattern in Figure 3.4) and a recalculation of the

same corner by the stereo calibration application. In this way, high-error image pairs can be identified and removed, and then the calibration process should be restarted. If the first indications seem sufficient, measured GPS-positions were used to compare matching distances such as between two poles or between the two mounted cameras. Also, in the vertical direction, a known pattern at each pole was a valued tool to check the calibration. After it turned out that also these indications were good, a more thorough validation was necessary. At pole 1, two time series were estimated in the same time window by using one of the cameras as an optical wave gauge (pole graduations) and by using the stereo imaging system. The root mean squared (RMS) difference of the obtained time series was calculated to validate the calibration results and was found to be less than 0.015 m.

The next step is to locate and track several surface tracers. We chose smooth non-breaking waves where the orange was visible most of the time. That is, we tried to avoid waves where the orange got non-visible because of shadows, foam or it went behind the wave crest. To get the 3D world coordinate of the position to an orange tracer, it is important that the orange is visible in both camera views at the same time stamp. In Figure 3.6, an orange is dropped between pole 1 and pole 2 and is visible in both field of views. With a frame rate of 30 frames per second, the pixel positions of the oranges were found and registered manually for each camera. After the tracer had been followed, the pixel positions together with the calibration parameters were used as an input to a triangulation function in MATLAB to calculate the corresponding 3D world coordinates. The specific MATLAB script to display images and how to register pixel position from the image were provided by Dr. Marc Buckley, and the triangulation function is provided by MATLAB, while the rest of the methods and calculations had to be created during the process.



Figure 3.6: In a pair of frames from the same time stamp, one can see a swimmer who has dropped an orange in the wave field in between pole 1 and pole 2.

At this point, a typical tracer particle path would be presented as in Figure 3.7. In order to find the cross-shore mass transport, this coordinate system is impractical

due to the independence of the reality at the beach. As an initial step to create a new and more appropriate coordinate system, consulting images provided by the drone together with the peak direction data recorded by the offshore buoy, gave us a good basis for assuming that the direction of the incoming travelling waves is parallel to the line of poles. Which means that, we assume that the wave crests are perpendicular to the poles and that this will not have a large impact considering the long-shore drift. Of course, the wave direction as well as the long-shore drift varies from wave to wave, but the variations were small. In fact, the poles were installed with an angle of 281° , while the peak direction measured by the buoy was approximately 284° .

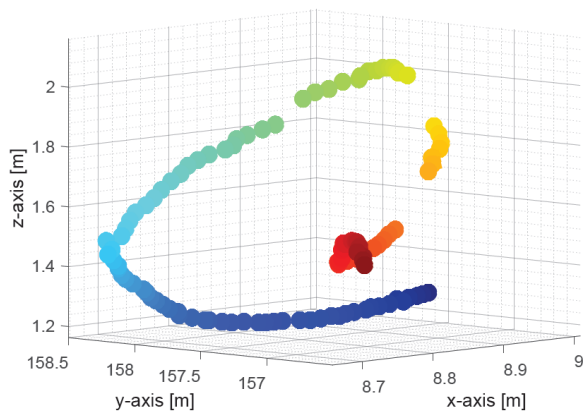


Figure 3.7: An orange path is plotted in the 3D world coordinate system defined by the calibration toolbox. The path is in different colors in order to see the oranges displacement. The initial position represents dark blue and the final position represents dark red.

Moreover, how to create a horizontal axis out in the field, or similar, how to create a vertical axis? Conveniently, at pole 2 and pole 3 there were brackets attached with measured GPS-positions. To find a 3D point in world coordinates, one needs to find the same location in both FOVs. For example, the 3D point a which is located at the bracket at pole 3, see the illustrative drawing in Figure 3.8, can be obtained by finding the pixel positions in both camera FOVs and then being triangulated into one 3D point in the world coordinate system defined by the calibration. Reviewing the GPS-measurements at the brackets located at a and d , the bracket at pole 2 is vertically 15 cm higher up than the bracket at pole 3. Therefore, in terms of finding a horizontal vector between a and b , the pattern at pole 2 were used to approximately find the pixel positions below the bracket at point d . The location of point b was checked and approved by confirming the distances between a , b and d . In this way the horizontal vector \vec{ab} was created and the basis for the new coordinate system was set. With the estimated 3D world points at a , b , c and d , the corresponding vectors leads us to the necessary vertical vector \vec{cs} . This vertical vector can be found by the

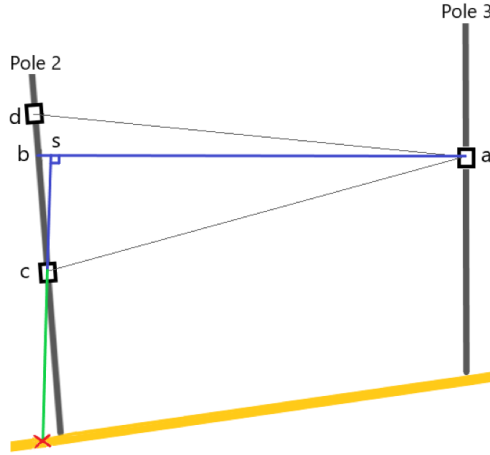


Figure 3.8: Illustrative drawing of pole 2 and pole 3 standing at the sloping beach. The square boxes indicate the brackets, and the solid blue lines shows the horizontal and vertical directions. Pole 2 is excessively skewed to visualize the difference between the pole and the vertical direction found between point c and s . Following the green line, a red cross is located where the new origin will take place approximately at the bottom at pole 2.

relation

$$\vec{cs} = k\vec{ab} - \vec{ac}, \quad (3.1)$$

where k denotes a constant. As the two vectors \vec{cs} and \vec{ab} must be orthogonal and satisfy the criteria

$$\vec{cs} \cdot \vec{ab} = 0,$$

an expression of k can be calculated and substituted into equation (3.1). The last axis is obtained by taking the cross product between the horizontal and vertical vector. The three orthogonal vectors are then normalized and rearranged so that the origin is placed at the bottom of pole 2, the x-axis is pointing along the poles towards the beach, the y-axis is pointing in the long-shore direction and the z-axis is pointing vertically upwards. In order to see the cross-shore mass transport, the surface tracer path is projected onto the xz -plane. For illustrative purposes of the new coordinate system, see Figure 3.9, which shows an original orange path and the projected orange path.

Finally, each projected position of the tracer describe by the coordinate system given by the calibration toolbox are transformed into the new coordinates described above. Let $P_{S \leftarrow B}$ be the change-of-coordinates matrix consisting of the normalized and orthogonal vectors defined at the bottom of pole 2. Let $[\mathbf{x}]_S$ denote a position vector \mathbf{x} described by the coordinate system given by the calibration and let $[\mathbf{x}]_B$ be the corresponding position described in the new coordinates, then, according to

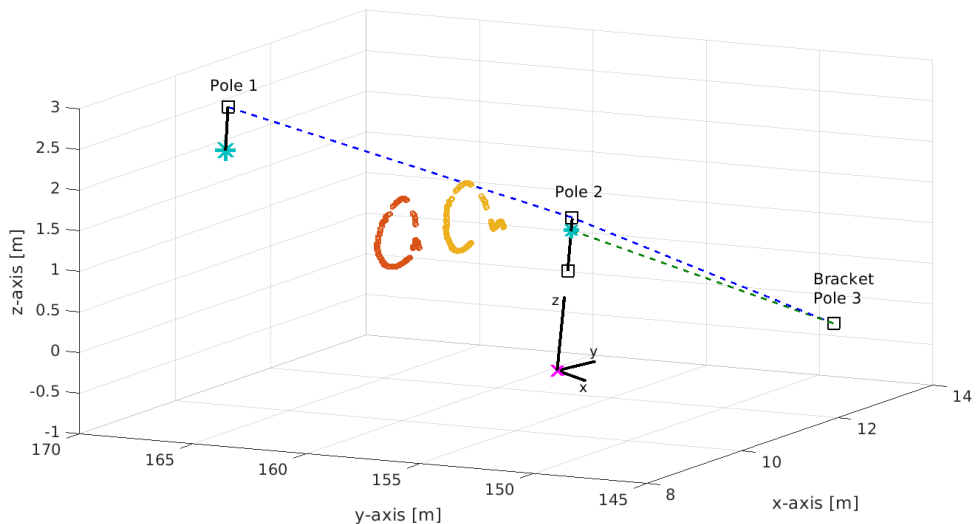


Figure 3.9: This is a plot in the 3D world coordinate system defined by the calibration toolbox. The black squares indicate brackets, and the turquoise stars indicate other points located by the stereo imaging system. The original orange path is shown in red and the projected path is shown in yellow. The blue dashed curve shows the direction of the line of poles through one point at each pole. The direction of the horizontal vector found between pole 2 and 3 is plotted with a green dashed curve. The pink cross indicates where the new origin is placed at the seabed at pole 2, and the black solid lines demonstrate the three orthogonal basis corresponding to the new coordinate system.

[27],

$$[\mathbf{x}]_S = P_{S \leftarrow B} [\mathbf{x}]_B$$

or, equally

$$P_{B \leftarrow S} [\mathbf{x}]_S = [\mathbf{x}]_B$$

gives us each tracer positions described by the new coordinate system. In Figure 3.10, an orange path is projected onto the xz -plane in the new coordinate system.

3.3 Data analysis

Measurements from the pressure gauges and the ADV were obtained during the field campaign, and several tracer paths were found and estimated in the post-process. The recorded pressure signal was transformed into the free-surface elevation (see more details in [S]), and since it had been recorded over a period of 10 minutes, an average free-surface could be calculated. The ADV measurement provided the Eulerian velocity in the water column in approximately the same directions as the

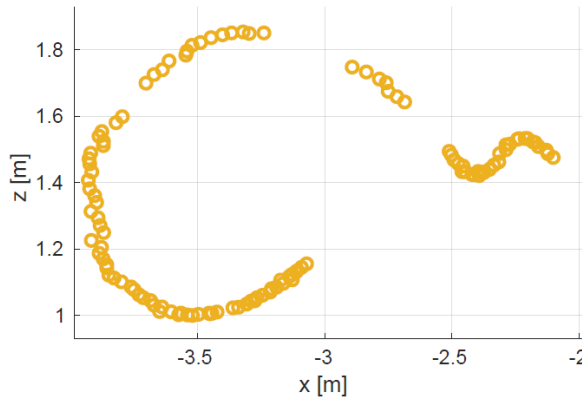


Figure 3.10: Projected orange path plotted in the coordinate system given by the origin placed at the bottom of pole 2, x-axis pointing shoreward along the poles, y-axis pointing in the long-shore direction and the z-axis pointing vertically upwards. Note that the same orbital orange path is plotted in Figure 3.7 and in Figure 3.9

axis in our new coordinate system. With this data available, a time series of the flow velocity in the x-direction could therefore be analyzed. However, in this section, a more detailed description of the analysis of tracer paths, also called Lagrangian trajectories will be given, and we will see that the time series of the free-surface elevation and the Eulerian velocity can be evaluated in a similar way.

Before initiating orange tracking by hand, the wave field should satisfy some criteria. By studying the footage, we looked for a period of time where the waves were non-steep and long-crested, with long wavelengths and with almost no spilling or breaking waves present. In addition, at least one orange had to be in both FOVs at the same time stamps. A wave was classified as non-breaking if there was no sign of spilling nor plunging before the propagating wave reached pole 3. To demonstrate, let us concentrate on a one minute and 14 seconds long orange tracking period where an orange was located near the array of poles in between pole 1 and pole 3. The orange is pinpointed by hand in both FOVs followed up by a triangulation, cleaning of outliers, projected and transformed into the new coordinate system. Figure 3.11 shows Lagrangian trajectories found by tracking one single orange over this period. Here every wave is examined and registered if breaking or spilling is occurring or not. As can be seen in the figure, there are several gaps because sometimes the tracer is not visible in both cameras. This is mainly because the orange is hidden behind the waves if the wave height is too high. Overall, the orbital paths give a quite messy impression when several are plotted in one figure. Therefore, an idea to look at it differently could be to plot the tracer elevation as a time series. This is done in Figure 3.12 where the green circles denotes every orange position plotted in Figure 3.11. Note that normally a time series is constructed by data where the recording

position is fixed over time, while here the orange moves around spatially. With

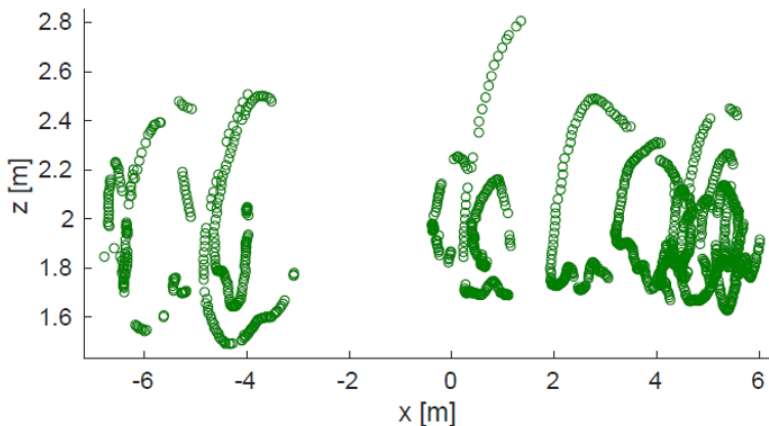


Figure 3.11: Lagrangian trajectories found by tracking one orange over a one minute and 14 second period. The green circles represent projected locations of the orange and shows the cross-shore orbital paths.

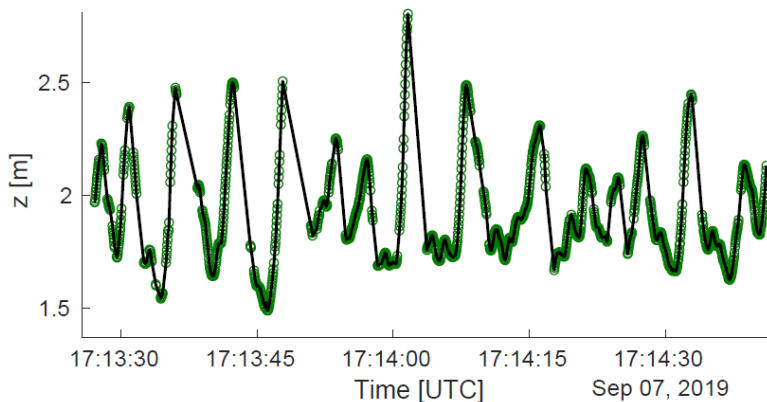


Figure 3.12: The tracer elevation is plotted over the time period in order to get a better view of the orange paths and the wave field. The green circles represents the same tracer positions as in Figure 3.11, respectively. The black solid curve is an interpolation of the obtained positions.

the interpolated black solid curve, it is easier to see the tracer elevation, and since the orange is floating at the surface, the black curve is also indicating the surface elevation where the orange is located.

Nevertheless, it is not clear how to identify each orbital path corresponding to each wave in order to calculate the cross-shore mass transport and the Lagrangian velocity. For the purpose of doing that, a zero-crossing analysis is a good option in

this case. With the average tracer elevation removed, the orbital paths, or equivalent the wave field, can be segmented into wave-by-wave by using the time stamps where the elevation crossing zero. A wave could be defined either by up-crossing or down-crossing, see Figure 3.13 for a down-crossing segmentation of the interpolated curve plotted in Figure 3.12. The black stars indicates where the curve is zero, and the orbital trajectories corresponding to the surface waves are described in different colors.

By this segmentation, the wave period and wave height (distance from trough to crest) can be found for each wave. As an illustration to make sense of the term wave-by-wave mean-water level, a black horizontal line is plotted at each wave in Figure 3.13 as an indication of the value of the mean-water level. For example, the blue wave to the left has an increased mean-water level (local set-up), while the blue wave to the right has a decreased mean-water level (local set-down). However, the wave-by-wave set-up and set-down calculated from a one minute and 14 seconds tracking period is not sufficient and should be estimated by using the pressure gauge measurements instead.

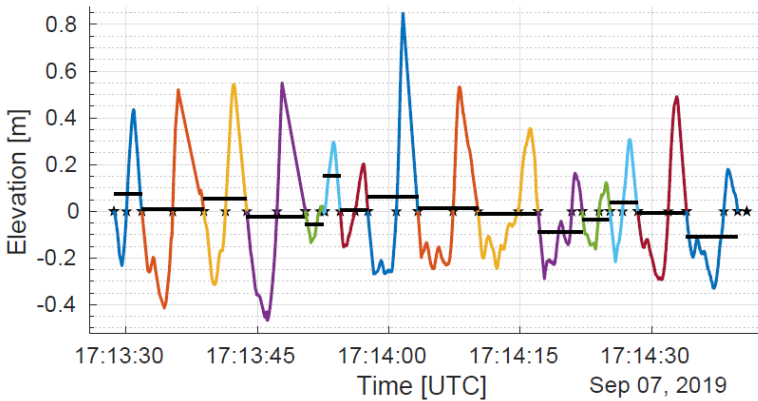


Figure 3.13: A down-crossing segmentation of the interpolated curve shown in Figure 3.12. The black stars represents where the curve intercept the axis and the value is zero. The orbital trajectories corresponding to the water waves are given in different colors. The horizontal black lines indicate the mean-water level corresponding to a single wave.

With the interception time stamps given by the black stars in Figure 3.13, a similar plot showing the cross-shore mass transport can be created, see Figure 3.14. Note that in Figure 3.13, every interception point is given by a black star, while conveniently in Figure 3.14 only the initial and final time respective to an orbital path is denoted by a black star. Here, the particle drift during one wave cycle in the x -direction can be seen. This also gives us the net cross-shore displacement which together with the wave period gives us the Lagrangian velocity.

In this way of analysing orbital trajectories, for then to add more paths and

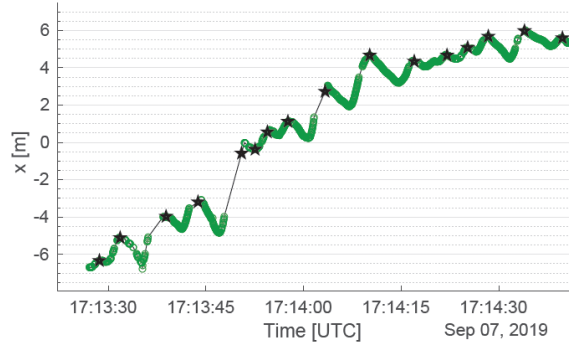


Figure 3.14: For each segmented orbital path, the particle drifts in the x -direction are plotted over the same time period. As before the green circles represents the orange positions, while the black solid curve is an interpolated curve between the positions. Here the black stars only represent the initial and final time to each wave cycle.

excluding the breaking waves, the correlation between the (Lagrangian) wave height and the Lagrangian velocity could be examined. Correlation between the Lagrangian velocity and the wave-by-wave mean-water level were also calculated. Although here, the local mean-water level is calculated by doing a zero-crossing segmentation on the free surface elevation obtained from the pressure data instead. As mentioned before, the pressure signal was recorded over a longer time period and therefore the estimation of the free-surface equilibrium state (when the free surface is at rest) is more precise. Conducting zero-crossing analyses on both time series obtained by the pressure gauge measurements and ADV measurements recorded at pole 2, gave us the mean-water level, the wave height and the cross-shore Eulerian flow velocity in the water column. With this done, a study of the relation between the Eulerian velocity with both the variation of mean-water level and the wave height could be done, as well as the impact of incipient wave breaking.

Bibliography

- [1] I. Aavatsmark, *Bevarelsesmetoder for hyperbolske differensialligninger*, Lecture notes, 2004.
- [2] A. Ali and H. Kalisch, *Reconstruction of the pressure in long-wave models with constant vorticity*, Eur. J. Mech. B Fluids **37** (2013), 187–194.
- [3] A. Ali and H. Kalisch, *On the formulation of mass, momentum and energy conservation in the KdV equation*, Acta Applicandae Mathematicae **133** (2014), 113–131.
- [4] M. Antuono and M. Brocchini, *The boundary value problem for the nonlinear shallow water equations*, Stud. Appl. Math. **119** (2007), 73–93.
- [5] M. Antuono and M. Brocchini, *Analysis of the nonlinear shallow water equations over nonplanar topography*, Stud. Appl. Math. **124** (2010), 85–103.
- [6] A. Benetazzo, *Measurements of short water waves using stereo matched image sequences*, Coastal engineering **53** (2006), 1013–1032.
- [7] A. Benetazzo, F. Fedele, G. Gallego, P.C Shih and A. Yezzi, *Offshore stereo measurements of gravity waves*, Coastal Engineering **64** (2012), 127–138.
- [8] X. Bertin, A. De Bakker, A. Van Dongeren, G. Coco, G. Andre, F. Ardhuin and others, *Infragravity waves: From driving mechanisms to impacts*, Earth-Science Reviews **177** (2018), 774–799.
- [9] M. Bjørkavåg and H. Kalisch, *Wave breaking in Boussinesq models for undular bores*, Physics Letters A **375** (2011), 1570–1578.
- [10] M. Bjørnestad, *Exact solutions for shoaling waves in shallow water*. MS thesis. The University of Bergen (2017).
- [11] M. Bjørnestad, *Run-up of long waves on background shear currents*, Wave Motion **96** (2020), 102551.
- [12] M. Bjørnestad, M. Buckley, H. Kalisch, M. Streßer, J. Horstmann, H.G. Frøysa, O.E. Ige, M. Cysewski and R. Carrasco-Alvarez, *Lagrangian Measurements of*

- Orbital Velocities in the Surf Zone*, Geophysical Research Letters, revision submitted, 2021.
- [13] M. Bjørnestad and H. Kalisch, *Shallow Water Dynamics on Linear Shear Flows and Plane Beaches*, Physics of Fluids **29** (2017), 073602.
- [14] M. Bjørnestad and H. Kalisch, *Extreme wave runup on a steep coastal profile*, AIP Advances **10** (2020), 105205.
- [15] M. Bjørnestad, H. Kalisch, M. Abid, C. Kharif and M. Brun, *Wave Breaking in Undular Bores with Shear Flows*. Water Waves (2021), 1–18.
- [16] H. Borluk and H. Kalisch, *Particle dynamics in the KdV approximation*, Wave Motion **49** (2012), 691–709.
- [17] M.K Brun, and H. Kalisch, *Convective wave breaking in the KdV equation*, Anal. Math. Phys. **8** (2018), 57–75.
- [18] R. Calvert, C. Whittaker, A. Raby, P.H Taylor, A. Borthwick and T. Van Den Bremer, *Laboratory study of the wave-induced mean flow and set-down in unidirectional surface gravity wave packets on finite water depth*, Physical Review Fluids **4**, 114801.
- [19] G.F. Carrier and H.P. Greenspan, *Water waves of finite amplitude on a sloping beach*, J Fluid Mech **4** (1958), 97–109.
- [20] B. Castelle, T. Scott, R. Brander and R. McCarroll, *Rip current types, circulation and hazard*, Earth-Science Reviews **163** (2016), 1–21.
- [21] I.M. Cohen, P.K. Kundu and D.R. Dowling, *Fluid mechanics fifth edition*, Elsevier Inc., 2012.
- [22] R. Courant and K.O. Friedrichs, *Supersonic flow and shock waves* Springer-Verlag, 1999.
- [23] I. Didenkulova, E. Pelinovsky and T. Soomere *Long surface wave dynamics along a convex bottom*, J. Geophys. Res.: Oceans **114** (2009), C7.
- [24] H. Favre: *Ondes de Translation*, Dunod, Paris 1935.
- [25] S. L. Gavriluk, N. I. Makarenko, and S. V. Sukhinin, *Waves in Continuous Media*, Springer International Publishing, 2017.
- [26] R.S. Johnson, *A modern introduction to the mathematical theory of water waves*, Cambridge University Press, 1997.
- [27] D.C. Lay, *Linear Algebra and Its Applications*, Third Edition, Pearson education, Inc., 2006.

- [28] V. Roeber, K.F Cheung and M.H Kobayashi, *Shock-capturing boussinesq type model for nearshore wave processes*, Coastal Engineering **57** (2010), 407–423.
- [29] A. Rybkin, D. Nicolsky, E. Pelinovsky and M. Buckel, *The Generalized Carrier–Greenspan Transform for the Shallow Water System with Arbitrary Initial and Boundary Conditions*, Water Waves **3** (2021), 267–296.
- [30] A. Senthilkumar and H. Kalisch, *Wave breaking in the KdV equation on a flow with constant vorticity*, European Journal of Mechanics-B/Fluids **73** (2019), 48–54.
- [31] Stereo Camera Calibrator App, <https://se.mathworks.com/help/vision/ug/stereo-camera-calibrator-app.html>, MathWorks.
- [32] J.J. Stoker, *The formation of breakers and bores the theory of nonlinear wave propagation in shallow water and open channels*, Communications on Pure and Applied Mathematics **1.1** (1948), 1–87.
- [33] J.J. Stoker, *Water Waves: The Mathematical Theory with Application*, Interscience Publishers, Inc., New York, 1957.
- [34] I.B. Svendsen, *Mass flux and undertow in a surf zone*, Coastal Eng. **8** (1984), 347–365.
- [35] A.F. Teles da Silva and D.H. Peregrine, *Steep, steady surface waves on water of finite depth with constant vorticity*, J. Fluid Mech. **195** (1988), 281–302.
- [36] J. Touboul, J. Charland, V. Rey and K. Belibassakis, *Extended mild-slope equation for surface waves interacting with a vertically sheared current*, Coastal Engineering **116** (2016), 77–88.
- [37] T. L. Walton and R. G. Dean, *Landward limit of wind setup on beaches*, Ocean Eng. **36** (2009), 763–766.
- [38] G.B. Whitham, *Linear and nonlinear waves*, John Wiley and Sons, 1999.
- [39] W.Y. Wong, M. Bjørnestad, C. Lin, M.J. Kao, H. Kalisch, P. Guyenne, V. Roeber, and J.M. Yuan, *Internal flow properties in a capillary bore*, Physics of Fluids **31** (2019), 113602.

Part II
Included papers

Paper A

Shallow water dynamics on linear shear flows and plane beaches

M. BJØRNESTAD AND H. KALISCH
Physics of Fluids **29** (2017), 073602.

Shallow water dynamics on linear shear flows and plane beaches

Cite as: Phys. Fluids **29**, 073602 (2017); <https://doi.org/10.1063/1.4994593>

Submitted: 24 March 2017 . Accepted: 30 June 2017 . Published Online: 24 July 2017

Maria Bjørnstad, and Henrik Kalisch



View Online



Export Citation



CrossMark

ARTICLES YOU MAY BE INTERESTED IN

[Vortex dynamics in nonlinear free surface flows](#)

Phys. Fluids **29**, 032101 (2017); <https://doi.org/10.1063/1.4977801>

[Higher-order modulation theory for resonant flow over topography](#)

Phys. Fluids **29**, 077101 (2017); <https://doi.org/10.1063/1.4991914>

[Why do we live for much less than 100 years? A fluid mechanics view and approach](#)

Phys. Fluids **29**, 081903 (2017); <https://doi.org/10.1063/1.4998717>



CAPTURE WHAT'S POSSIBLE
WITH OUR NEW PUBLISHING ACADEMY RESOURCES

Learn more

Shallow water dynamics on linear shear flows and plane beaches

Maria Bjørnestad and Henrik Kalisch

Department of Mathematics, University of Bergen, P.O. Box 7800, 5020 Bergen, Norway

(Received 24 March 2017; accepted 30 June 2017; published online 24 July 2017)

Long waves in shallow water propagating over a background shear flow towards a sloping beach are being investigated. The classical shallow-water equations are extended to incorporate both a background shear flow and a linear beach profile, resulting in a non-reducible hyperbolic system. Nevertheless, it is shown how several changes of variables based on the hodograph transform may be used to transform the system into a linear equation which may be solved exactly using the method of separation of variables. This method can be used to investigate the run-up of a long wave on a planar beach including the development of the waterline. *Published by AIP Publishing.* [<http://dx.doi.org/10.1063/1.4994593>]

I. INTRODUCTION

While many classical results in the theory of surface water waves have been obtained in the context of irrotational flow, the assumption of zero vorticity is not always justified. Indeed, it is well known that vorticity may have a strong effect on the properties of surface waves, and there is now a growing literature on the effect of vorticity on the properties of surface waves. In mathematical studies focused on the influence of vorticity on the dynamics of a free surface, some simplifying assumptions are usually made. Examples of cases which have proved to be mathematically tractable include compactly supported vorticity, such as point vortices or vortex patches,^{11,17} the interaction of horizontal and vertical vorticity,⁷ and the creation of vorticity through singular flow such as a hydraulic jump.¹⁵

One important case which is particularly amenable to both analytic and numerical methods is the propagation of waves over a linear shear current. As noted in the classical paper,¹⁸ there is a scale separation between long surface waves and typical shear profiles, which justifies the assumption that the shear is unaffected by the wave motion to the order of accuracy afforded by the model, and moreover, the precise profile of the shear flow may be approximated with a linear shear. Previous works on this topic include the construction of periodic traveling waves over shear flows in the Euler equations,⁹ numerical investigations,²⁰ and the investigation of the pressure profile in asymptotic models.^{1,21}

In the present work, we consider the case where a background shear current interacts with a sloping beach. In particular, suppose the seabed is given by $h(x) = -\alpha x$, and a background shear flow $U(x, z)$ is imposed (see Fig. 1). Such a situation may arise in the case of an onshore wind (blowing from the ocean and onto the land) which induces a surface current at and near the surface which is directed towards the beach.²² Depending on the strength of the wind forcing and the beach geometry, the resulting return flow may be in the form of an undertow, and mass conservation requires that the average $\int_{-h}^0 U(x, z) dz$ be equal to zero. To a first approximation, the situation may be described by the imposed linear

shear flow $U(x, z) = \Gamma_1 \left(\frac{h}{2} + z \right)$ which has the property that $\int_{-h}^0 U(x, z) dz = 0$.

As shown in the Appendix, for long surface waves, small angles α , and relatively small amplitudes, a set of shallow-water equations may be derived from first principles. The system has the form

$$\eta_t + \left(\frac{\Gamma_1}{2} \eta (\eta - \alpha x) + u (\eta - \alpha x) \right)_x = 0, \quad (1)$$

$$u_t + \left(\frac{\alpha \Gamma_1}{2} x \left(u + \frac{\alpha \Gamma_1}{4} x \right) + \frac{u^2}{2} + g\eta \right)_x = 0, \quad (2)$$

where $\eta(x, t)$ describes the deflection of the free surface at a point x and a time t , and $u(x, t)$ represents the horizontal fluid velocity. The coefficient $\alpha \Gamma_1$ represents the strength of the interaction between the sloping seabed and the shear flow. Note that this system is hyperbolic, but the inclusion of non-trivial bathymetry makes the system irreducible. Nevertheless, it will be shown in the body of this paper that it is possible to employ a hodograph transform which aids in the construction of exact solutions of the system and in particular allows us to make predictions of the development of the waterline.

The idea of exchanging the roles of dependent and independent variables originated in the theory of gas dynamics¹⁰ and has been used in various special cases in hyperbolic equations, including the shallow-water equations. However, it was not until the work of Carrier and Greenspan⁵ that it became possible to find exact solutions for the shallow-water equations in the case of non-constant bathymetry. Indeed, the real novelty of the work of Carrier and Greenspan lay in the fact that they succeeded in applying the hodograph transform in the case of a non-uniform environment. In particular, they obtained explicit solutions to the non-linear shallow-water equations on a linear beach profile, but without vorticity.

There are a few important variations on the method of Carrier and Greenspan. In particular, more general initial data were considered in Ref. 6, and physical properties such as mass and momentum fluxes related to the possible run-up of a tsunami were mapped out. Some generalizations of the method

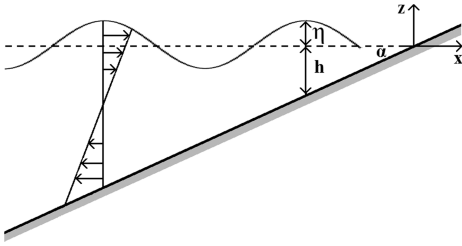


FIG. 1. Sloping beach given by $h(x) = -\alpha x$ and imposed shear flow $U(x, z)$.

with regards to the shape of the beach profile were made in Ref. 12, where a convex bottom topography of the type $h(x) = x^{4/3}$ was considered. Also, three-dimensional effects were included in recent work,¹⁶ where a general approach was put forward to study the problem in a bay of arbitrary cross section. The work laid down in Ref. 3 makes use of analysis techniques to estimate the Jacobian function associated with an arbitrary bottom profile and thus shows that at least in theory, the restriction to planar or convex beaches is not necessary. One problematic issue with the approach of Carrier and Greenspan is that it is difficult to treat the boundary-value problem. For example, if wave and velocity data are known at a fixed location, it is not straightforward to prescribe these as boundary data and study the shoaling and run-up of the resulting shorewards propagating waves. This problem was investigated in-depth in Ref. 2, where it was shown how the boundary-value can be solved in the context of planar beaches.

As we stated above, the main purpose of the current work is to extend the Carrier-Greenspan approach to the case where background vorticity can be included in the flow. The need for such an extension arises from the fact that the propagation of water waves in coastal areas is often affected by the influence of currents. A typical situation in which long waves enter a region of shear flow near a beach is the case of the leading part of a swell approaching a beach where a background shear flow has been set up independently by a sea breeze. The wind causes a shear flow directed towards the beach, and the return flow leads to an undertow, resulting in a shear profile such as that shown in Fig. 1. In particular, as explained in Ref. 18, if the leading waves of the swell are long compared to the fluid depth, a shear profile with a certain mean vorticity may be used in place of the exact distribution of vorticity.

Some recent studies have indicated the importance of a near-shore shear current from different perspectives. In particular, in Ref. 22, it was argued that such a current, which can be induced by an onshore wind, will have a significant effect on the mean-water level at the beach and may therefore enhance wave run-up under various conditions.

The plan of the current paper is as follows. In Sec. II, we consider the case of a shear flow over a flat bed. While the inclusion of background vorticity into shallow-water models is known (see Ref. 13, for instance), it is not obvious how to find closed-form expressions for the Riemann invariants in this case. In Sec. III, we treat the case of a shear flow over a linear beach and use intuition gained from the Riemann invariants in

the flat bed case to aid in the construction of the hodograph transform in the more difficult case of non-constant bathymetry. Finally, in Sec. IV, we explain how the equations may be solved exactly. We include a few plots where we compare cases with different strengths of background vorticity, and we close with a brief discussion on the effect of background vorticity on the run-up and mean-water level. Finally, the equations with both shear flow and an uneven bottom are derived in the Appendix.

II. SHEAR FLOW OVER A FLAT BED

We first look at the case of a shear flow over a flat bed as this case will give us important clues on how to proceed in the more difficult case of a shear flow over a sloping bed. A sketch of the geometry is shown in Fig. 2. In particular, the total depth is $H(x, t) = \eta(x, t) + h_0$, where h_0 is the constant undisturbed depth. The vertical shear current is assumed to be of the form $U(z) = -\Gamma_0 + \Gamma_1 z$, which yields a background vorticity $-\Gamma_1$. Without loss of generality, we may assume that the density is constant and consider a domain of unit width in the transverse direction. The shallow-water equations for a flat bed are as follows:

$$H_t + (-\Gamma_0 H + \frac{\Gamma_1}{2} H^2 + uH)_x = 0, \tag{3}$$

$$u_t + (-\Gamma_0 u + \frac{1}{2} u^2 + gH)_x = 0. \tag{4}$$

In order to express the equations in non-dimensional variables, we introduce the following scaling: $u^* = \frac{u}{u_0}$, $\eta^* = \frac{\eta}{h_0}$, $x^* = \frac{x}{h_0}$, $t^* = \frac{t}{T}$, $\Gamma_0^* = \frac{\Gamma_0}{u_0}$, $\Gamma_1^* = \frac{\Gamma_1}{1/T}$, where $T = \sqrt{h_0/g}$, $u_0 = \sqrt{g h_0}$. The equations are then written in non-dimensional form as

$$H_r^* + (-\Gamma_0^* H^* + \frac{\Gamma_1^*}{2} H^{*2} + u^* H^*)_x^* = 0,$$

$$u_r^* + (-\Gamma_0^* u^* + \frac{1}{2} u^{*2} + H^*)_x^* = 0.$$

As is customary in shallow-water theory, the propagating speed of a wave is taken as $c = \sqrt{gH}$ (in non-dimensional variables $c^* = \sqrt{H^*}$, where $c^* = \frac{c}{u_0}$). Note that for easier reading, the stars on the non-dimensional variables will be omitted from now on. Adding and subtracting the two equations above, and using the speed c as an unknown, the equations can be written in so-called pre-characteristic form as

$$\left\{ \frac{\partial}{\partial t} + (u - \Gamma_0 + c) \frac{\partial}{\partial x} \right\} (u + 2c) = -2\Gamma_1 c^2 c_x,$$

$$\left\{ \frac{\partial}{\partial t} + (u - \Gamma_0 - c) \frac{\partial}{\partial x} \right\} (u - 2c) = 2\Gamma_1 c^2 c_x.$$

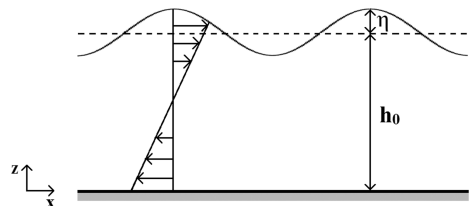


FIG. 2. Background shear flow for constant depth.

This form may be useful in some situations connected to numerical integration of the equations but is included here mainly as a stepping stone toward a similar set of equations in the case of the sloping bottom. In the current context, it is actually more advantageous to put the equations into proper characteristic form. However, since it is not easy to see how to eschew the $2\Gamma_1 c^2 c_x$ -terms on the right hand side, we will use a different approach to put the equations in characteristic form.

In vector notation, we can write Eqs. (3) and (4) as

$$\mathbf{u}_t + \mathbf{f}(\mathbf{u})_x = \mathbf{0}, \quad (5)$$

where $\mathbf{u} = [H, u]^T$. Further, $\mathbf{f}(\mathbf{u})_x = \mathbf{f}'(\mathbf{u})\mathbf{u}_x$, where $\mathbf{f}'(\mathbf{u})$ is the Jacobian matrix

$$\mathbf{f}'(\mathbf{u}) = \begin{bmatrix} -\Gamma_0 + \Gamma_1 H + u & H \\ 1 & -\Gamma_0 + u \end{bmatrix}.$$

The eigenvalues are

$$\xi_1 = u - \Gamma_0 + \frac{1}{2}\Gamma_1 H + \frac{1}{2}\sqrt{(\Gamma_1 H)^2 + 4H},$$

$$\xi_2 = u - \Gamma_0 + \frac{1}{2}\Gamma_1 H - \frac{1}{2}\sqrt{(\Gamma_1 H)^2 + 4H}.$$

These eigenvalues are real and distinct, which means that the system is strictly hyperbolic. Since the Jacobian matrix only depends on \mathbf{u} , and not x or t , the system is reducible, and Riemann invariants exist according to the standard theory.¹⁰ However, finding exact expressions for the Riemann invariants is in general highly non-trivial.

In order to find the Riemann invariants ω_1 and ω_2 , it will be convenient to define an eigenproblem $\mathbf{L}\mathbf{f}'(\mathbf{u}) = \mathbf{L}$ with the left eigenvectors

$$\mathbf{l}_1 = \begin{bmatrix} 2 \\ -\Gamma_1 H + \sqrt{(\Gamma_1 H)^2 + 4H} \end{bmatrix},$$

$$\mathbf{l}_2 = \begin{bmatrix} 2 \\ -\Gamma_1 H - \sqrt{(\Gamma_1 H)^2 + 4H} \end{bmatrix}.$$

Inserting the left eigenproblem in Eq. (5), we can express Eq. (5) as

$$\mathbf{l}_i^T \mathbf{u}_t + \xi_i \mathbf{l}_i^T \mathbf{u}_x = 0, \quad (6)$$

where $i = 1, 2$. If we now introduce the auxiliary function $\mu(\mathbf{u})$ satisfying

$$\nabla \omega_i(\mathbf{u}) = \left[\frac{\partial \omega_i}{\partial H}, \frac{\partial \omega_i}{\partial u} \right] = \mu_i(\mathbf{u}) \mathbf{l}_i^T, \quad (7)$$

Eq. (6) can be written as

$$\nabla \omega_i(\mathbf{u}) \mathbf{u}_t + \xi_i \nabla \omega_i(\mathbf{u}) \mathbf{u}_x = 0,$$

which is the same as

$$\left\{ \frac{\partial}{\partial t} + \xi_i \frac{\partial}{\partial x} \right\} \omega_i(\mathbf{u}) = 0.$$

The characteristic form in the latter equation shows that $\omega_i(\mathbf{u})$ is constant along the characteristics $\frac{dx}{dt} = \xi_i(\mathbf{u})$. The challenging part of this procedure is to find an expression for $\mu_i(\mathbf{u})$. To be able to proceed further, we start by assuming that $\mu_i(\mathbf{u})$ is

chosen such that the relation $\frac{\partial^2 \omega_i}{\partial H \partial u} = \frac{\partial^2 \omega_i}{\partial u \partial H}$ is satisfied. First, to calculate $\mu_1(\mathbf{u})$, Eq. (7) gives us

$$\begin{aligned} \frac{\partial \omega_1}{\partial H} &= 2\mu_1(\mathbf{u}), \\ \frac{\partial \omega_1}{\partial u} &= \mu_1(\mathbf{u}) \left(-\Gamma_1 H + \sqrt{(\Gamma_1 H)^2 + 4H} \right), \end{aligned}$$

and if we let

$$\mu_1(\mathbf{u}) = \Gamma_1 + \frac{1}{H} \sqrt{(\Gamma_1 H)^2 + 4H},$$

the assumption will be satisfied. Integration gives us

$$\omega_1 = 2\Gamma_1 H + 2\sqrt{(\Gamma_1 H)^2 + 4H} + \frac{8}{\Gamma_1} \sinh^{-1} \left(\frac{\Gamma_1 \sqrt{H}}{2} \right) + K_1(u),$$

$$\omega_1 = 4u + K_2(H),$$

where $K_1(H)$ and $K_2(u)$ are the constants of integration. By combining these, we obtain the first Riemann invariant

$$\omega_1 = u - \Gamma_0 + \frac{1}{2}\Gamma_1 H + \frac{1}{2}\sqrt{(\Gamma_1 H)^2 + 4H} + \frac{2}{\Gamma_1} \sinh^{-1} \left(\frac{\Gamma_1 \sqrt{H}}{2} \right),$$

where we also have divided by 4 and subtracted by Γ_0 to simplify further work.

We can obtain the second Riemann invariant in a similar way. With the expression for the parameter μ_2 given by

$$\mu_2(\mathbf{u}) = \Gamma_1 - \frac{1}{H} \sqrt{(\Gamma_1 H)^2 + 4H},$$

we get

$$\omega_2 = u - \Gamma_0 + \frac{1}{2}\Gamma_1 H - \frac{1}{2}\sqrt{(\Gamma_1 H)^2 + 4H} - \frac{2}{\Gamma_1} \sinh^{-1} \left(\frac{\Gamma_1 \sqrt{H}}{2} \right).$$

With these expressions in hand, Eqs. (3) and (4) can then be rewritten in characteristic form as

$$\begin{aligned} \left\{ \frac{\partial}{\partial t} + \xi_1 \frac{\partial}{\partial x} \right\} \omega_1 &= 0, \\ \left\{ \frac{\partial}{\partial t} + \xi_2 \frac{\partial}{\partial x} \right\} \omega_2 &= 0. \end{aligned}$$

However, the equations are still nonlinear. Since one purpose of the present study is to obtain exact representations of solutions of Eqs. (3) and (4), it will be convenient to perform yet another transformation to put the equations in linear form.

Switching dependent and independent variables via a hodograph transform from $\omega_1 = \omega_1(x, t)$ and $\omega_2 = \omega_2(x, t)$ to $x = x(\omega_1, \omega_2)$ and $t = t(\omega_1, \omega_2)$ results in

$$x_{\omega_2} - \xi_1 t_{\omega_2} = 0, \quad (8)$$

$$x_{\omega_1} - \xi_2 t_{\omega_1} = 0. \quad (9)$$

As long as the Jacobian matrix remains non-singular, linearity has been achieved and the equations can now be solved. We will come back to the solution in Sec. IV A.

III. SHEAR FLOW ON A SLOPING BED

We will now consider the geometry in Fig. 1 with the total depth $H(x, t) = \eta(x, t) + h(x)$. The vertical shear current is assumed to be of the form $U(x, z) = \Gamma_1 \left(\frac{h}{2} + z \right)$ with the vorticity $-\Gamma_1$. Note that the x -axis is now assumed to be aligned

with the undisturbed free surface as this normalization is more convenient in the current setting.

To put Eqs. (1) and (2) into non-dimensional form, we introduce new variables $u^* = \frac{u}{u_0}$, $\eta^* = \frac{\eta}{\alpha l_0}$, $x^* = \frac{x}{l_0}$, $t^* = \frac{t}{T}$, $\Gamma_1^* = \frac{\Gamma_1}{1/T}$, where $T = \sqrt{l_0/\alpha g}$, $u_0 = \sqrt{gl_0\alpha}$, and l_0 is a characteristic length. The equations then appear as

$$\eta_{t^*}^* + \left(\frac{\alpha\Gamma_1^*}{2}\eta^*(\eta^* - x^*) + u^*(\eta^* - x^*)\right)_{x^*} = 0, \tag{10}$$

$$u_{t^*}^* + \left(\frac{\alpha\Gamma_1^*}{2}x^* \left(u^* + \frac{\alpha\Gamma_1^*}{4}x^*\right) + \frac{u^{*2}}{2} + \eta^*\right)_{x^*} = 0. \tag{11}$$

As in Sec. II for the sake of readability, the stars will be disregarded in what follows. In an attempt to write the equations in characteristic form, one may insert the propagation speed in non-dimensional form $c = \sqrt{(\eta - x)}$ and then add and subtract them to obtain the pre-characteristic form

$$\left\{ \frac{\partial}{\partial t} + (u + \frac{\alpha\Gamma_1}{2}x + c) \frac{\partial}{\partial x} \right\} \left(u + \frac{\alpha\Gamma_1}{2}x + 2c + t \right) = -2\alpha\Gamma_1 c^2 c_x,$$

$$\left\{ \frac{\partial}{\partial t} + (u + \frac{\alpha\Gamma_1}{2}x - c) \frac{\partial}{\partial x} \right\} \left(u + \frac{\alpha\Gamma_1}{2}x - 2c + t \right) = 2\alpha\Gamma_1 c^2 c_x.$$

To be able to solve these equations, the difficulty lies in finding the Riemann invariants. We can write Eqs. (10) and (11) as $\mathbf{u}_t + \mathbf{f}(\mathbf{u}, x)_x = \mathbf{0}$, where $\mathbf{u} = [\eta, u]^T$. The Jacobian matrix $\mathbf{f}'(\mathbf{u}, x)$ has the following eigenvalues:

$$\xi_1 = u + \frac{\alpha\Gamma_1}{2}(x + c^2) + \frac{c}{2}\sqrt{(\alpha\Gamma_1 c)^2 + 4},$$

$$\xi_2 = u + \frac{\alpha\Gamma_1}{2}(x + c^2) - \frac{c}{2}\sqrt{(\alpha\Gamma_1 c)^2 + 4}.$$

Since the Jacobian matrix now depends on x , the system is not reducible, and it is not clear whether Riemann invariants can be found. In particular, we cannot proceed in the same way as in Sec. II. However, when carefully combining the pre-characteristic form and the eigenvalues with the corresponding equations for the flat bed case, a bit of informed guessing points to defining the Riemann invariants as

$$\omega_1 = u + \frac{\alpha\Gamma_1}{2}(x + c^2) + \frac{1}{2}c\sqrt{(\alpha\Gamma_1 c)^2 + 4} + \frac{2}{\alpha\Gamma_1} \sinh^{-1} \left(\frac{\alpha\Gamma_1 c}{2} \right) + t,$$

$$\omega_2 = u + \frac{\alpha\Gamma_1}{2}(x + c^2) - \frac{1}{2}c\sqrt{(\alpha\Gamma_1 c)^2 + 4} - \frac{2}{\alpha\Gamma_1} \sinh^{-1} \left(\frac{\alpha\Gamma_1 c}{2} \right) + t.$$

As it turns out, if these expressions are substituted into Eqs. (10) and (11), the characteristic form

$$\left\{ \frac{\partial}{\partial t} + \xi_1 \frac{\partial}{\partial x} \right\} \omega_1 = 0,$$

$$\left\{ \frac{\partial}{\partial t} + \xi_2 \frac{\partial}{\partial x} \right\} \omega_2 = 0$$

appears. These two equations are still nonlinear in t , so we continue by performing a hodograph transformation, changing $\omega_1 = \omega_1(x, t)$ and $\omega_2 = \omega_2(x, t)$ to $x = x(\omega_1, \omega_2)$ and $t = t(\omega_1, \omega_2)$, which results in the equations

$$x_{\omega_2} - \xi_1 t_{\omega_2} = 0,$$

$$x_{\omega_1} - \xi_2 t_{\omega_1} = 0.$$

In contrast to the flat bed case, the equations are still nonlinear at this stage. Therefore, another step is required, and we introduce new variables $\omega_1 + \omega_2 = \lambda$ and $\omega_1 - \omega_2 = \sigma$. This change of variables gives us

$$x_\lambda - A t_\lambda + B t_\sigma = 0,$$

$$x_\sigma - A t_\sigma + B t_\lambda = 0, \tag{12}$$

where to simplify we have defined $A = u + \frac{\alpha\Gamma_1}{2}(x + c^2)$ and $B = \frac{c}{2}\sqrt{(\alpha\Gamma_1 c)^2 + 4}$. Further, differentiating these equations and using the identities $x_{\sigma\lambda} = x_{\lambda\sigma}$ and $t_{\sigma\lambda} = t_{\lambda\sigma}$ leads to

$$A_\lambda t_\sigma - A_{\sigma} t_\lambda - B_\lambda t_\lambda + B_{\sigma} t_\sigma = B(t_{\lambda\lambda} - t_{\sigma\sigma}). \tag{13}$$

In order to find expressions for the derivatives of A and B with respect to σ and λ , we start by writing the variables λ and σ as

$$\frac{\lambda}{2} = u + \frac{\alpha\Gamma_1}{2}(x + c^2) + t, \tag{14}$$

$$\frac{\sigma}{2} = \frac{c}{2}\sqrt{(\alpha\Gamma_1 c)^2 + 4} + \frac{2}{\alpha\Gamma_1} \sinh^{-1} \left(\frac{\alpha\Gamma_1 c}{2} \right). \tag{15}$$

It is easy to see from Eq. (14) that $A_\sigma = -t_\sigma$ and $A_\lambda = \frac{1}{2} - t_\lambda$. To calculate B_λ and B_σ , we start by differentiating B to find

$$B_\sigma = \frac{(\alpha\Gamma_1 c)^2 + 2}{\sqrt{(\alpha\Gamma_1 c)^2 + 4}} c_\sigma, \quad B_\lambda = \frac{(\alpha\Gamma_1 c)^2 + 2}{\sqrt{(\alpha\Gamma_1 c)^2 + 4}} c_\lambda,$$

where c_σ and c_λ are unknown. We can find an expression for these by differentiating Eq. (15) implicitly with respect to σ and λ , yielding

$$\frac{1}{2} = c_\sigma \sqrt{(\alpha\Gamma_1 c)^2 + 4}, \quad 0 = c_\lambda \sqrt{(\alpha\Gamma_1 c)^2 + 4}. \tag{16}$$

Since the root cannot be zero, c_λ has to be zero. Thus, with these calculations, Eq. (13) becomes

$$\left(\frac{(\alpha\Gamma_1 c)^2 + 3}{(\alpha\Gamma_1 c)^2 + 4} \right) t_\sigma = \frac{c}{2} \sqrt{(\alpha\Gamma_1 c)^2 + 4} (t_{\lambda\lambda} - t_{\sigma\sigma}). \tag{17}$$

Unfortunately, the c is only given implicitly as a function of σ in Eq. (15). However, notice that in Eq. (15) both terms are increasing and monotone, so the relation can be inverted. Since we seek an expression for $c_{\sigma\sigma}$, we start by differentiating Eq. (15) twice and get

$$0 = c_{\sigma\sigma} \sqrt{(\alpha\Gamma_1 c)^2 + 4} + \frac{(\alpha\Gamma_1 c_\sigma)^2 c}{\sqrt{(\alpha\Gamma_1 c)^2 + 4}}.$$

By inserting c_σ from Eq. (16), we obtain the expression

$$c_{\sigma\sigma} = -\frac{(\alpha\Gamma_1)^2 c}{4((\alpha\Gamma_1 c)^2 + 4)^2}.$$

With some calculations, Eq. (17) then becomes

$$c t_{cc} + 3 t_c = 4c((\alpha\Gamma_1 c)^2 + 4) t_{\lambda\lambda}, \tag{18}$$

which is a linear equation and can now be solved exactly.

IV. EXACT SOLUTIONS OF THE EQUATIONS

A. Flat bed

One way to solve Eqs. (8) and (9) is to introduce new variables in the same way as shown above for the case of the sloping bed. Thus, introducing the variables $\lambda = \omega_1 + \omega_2$ and $\sigma = \omega_1 - \omega_2$, the equations can be written as

$$\begin{aligned} x_\lambda - (u - \Gamma_0 + \frac{1}{2}\Gamma_1 H)t_\lambda + \frac{1}{2}\sqrt{(\Gamma_1 H)^2 + 4H}t_\sigma &= 0, \\ x_\sigma - (u - \Gamma_0 + \frac{1}{2}\Gamma_1 H)t_\sigma + \frac{1}{2}\sqrt{(\Gamma_1 H)^2 + 4H}t_\lambda &= 0. \end{aligned} \tag{19}$$

Moreover remembering the expressions for ω_1 and ω_2 from Sec. II, λ and σ appear as

$$\begin{aligned} \frac{\lambda}{2} &= u - \Gamma_0 + \frac{\Gamma_1}{2}H, \\ \frac{\sigma}{2} &= \frac{1}{2}\sqrt{(\Gamma_1 H)^2 + 4H} + \frac{2}{\Gamma_1} \sinh^{-1}\left(\frac{\Gamma_1\sqrt{H}}{2}\right). \end{aligned} \tag{20}$$

Inverting the relation¹⁹ results in the following linear equation for $t(H, \lambda)$:

$$Ht_{HH} + 2t_H = (\Gamma_1^2 H + 4)t_{\lambda\lambda}. \tag{21}$$

Before we solve this equation, notice that it is problematic to calculate $x(H, \lambda)$ without introducing a “potential” function for $t(H, \lambda)$, i.e.,

$$t = \frac{1}{\Gamma_1^2 H + 4} \phi_H. \tag{22}$$

However, if this potential is used, Eq. (19) gives us an expression for $x(H, \lambda)$, viz.,

$$x = \frac{\lambda}{2}t - \frac{1}{2}\phi_\lambda.$$

Equation (21) can now be written due to Eq. (22) as

$$H(\Gamma_1^2 H + 4)\phi_{HH} + 4\phi_H = (\Gamma_1^2 H + 4)\phi_{\lambda\lambda}.$$

This equation can be solved using separation of variables, and the solution has the general form

$$\begin{aligned} \phi(H, \lambda) &= \cos(\omega\lambda)e^{-i\Gamma_1\omega H} [-\omega H(i\Gamma_1 - 2\omega)\mathcal{F}_1 \\ &\quad + (i\Gamma_1\omega H - 1)\mathcal{F}_2], \end{aligned}$$

where

$$\begin{aligned} \mathcal{F}_1 &= {}_1F_1\left(\frac{2i\omega + 2\Gamma_1}{\Gamma_1}, 3, 2i\Gamma_1\omega H\right), \\ \mathcal{F}_2 &= {}_1F_1\left(\frac{2i\omega + \Gamma_1}{\Gamma_1}, 2, 2i\Gamma_1\omega H\right) \end{aligned}$$

are given in terms of the generalized hypergeometric function ${}_1F_1$.¹⁴ Finally, the principal unknowns can be expressed in terms of λ and H as $u = \frac{\lambda}{2} + \Gamma_0 - \frac{\Gamma_1}{2}H$ and $\eta = H - h_0$.

B. Sloping bed

We now look at the more interesting case of exact solutions in the presence of the inclined bottom profile. To be able to solve for $x(c, \lambda)$, we will also here make use of a “potential” function. Instead of introducing the potential function for $t(c, \lambda)$ directly, we rather start by defining

$$W(c, \lambda) = u(c, \lambda) + \frac{\alpha\Gamma_1}{2}(x + c^2). \tag{23}$$

Combining the new function $W(c, \lambda)$ with Eq. (14), we can rewrite Eq. (18) and obtain

$$cW_{cc} + 3W_c = 4c((\alpha\Gamma_1 c)^2 + 4)W_{\lambda\lambda}. \tag{24}$$

If we now define the function $\phi(c, \lambda)$ by

$$W(c, \lambda) = \frac{1}{c((\alpha\Gamma_1 c)^2 + 4)}\phi_c(c, \lambda),$$

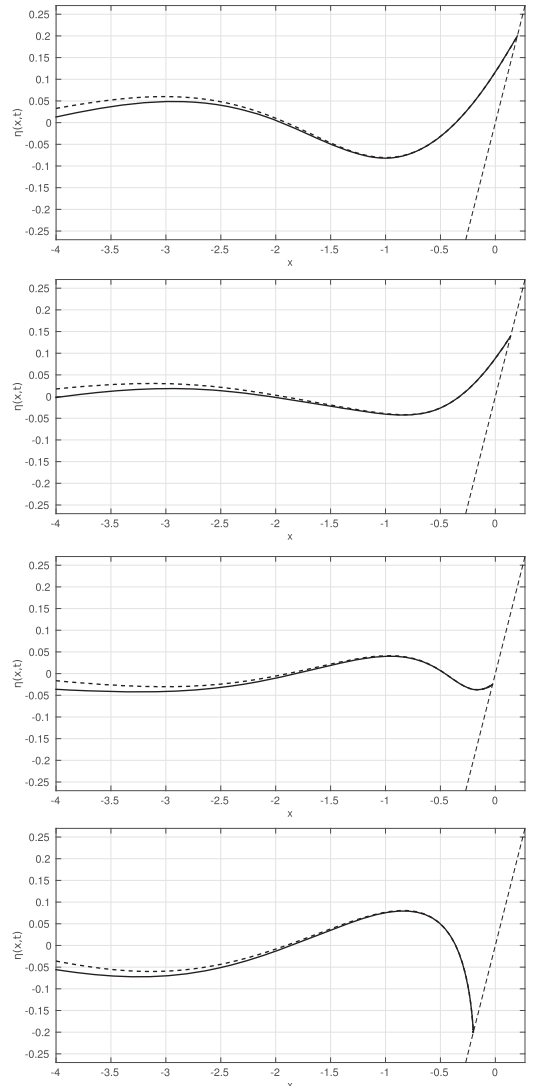


FIG. 3. Free surface evolution with and without vorticity. The parameters are $R_{max} = 0.2$, $\alpha\Gamma_1 = 0.1$, and $\omega = 1$. The four plots are shown at time $t_1 = \frac{\pi}{4}$, $t_2 = \frac{5\pi}{12}$, $t_3 = \frac{7\pi}{12}$, and $t_4 = \frac{3\pi}{4}$. The nonzero vorticity has the effect of introducing a slight setdown on the left-hand side.

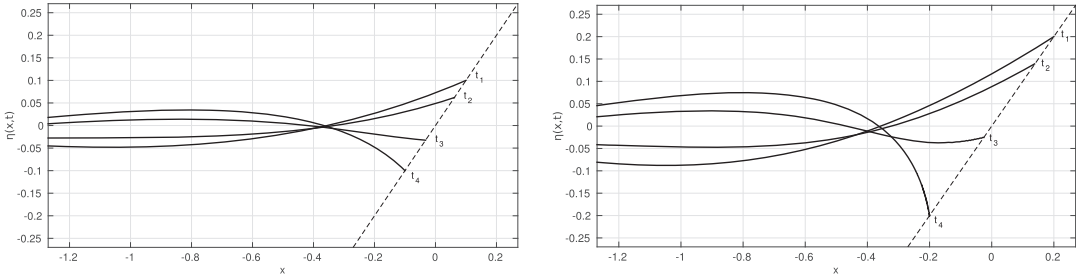


FIG. 4. Solution of a wave running up on a sloping beach. The left panel shows a solution with $R_{max} = 0.1$ and $\alpha\Gamma_1 = 0.25$. The right panel shows a solution with $R_{max} = 0.2$ and $\alpha\Gamma_1 = 0.25$. The solutions are plotted at $t_1 = \frac{\pi}{4}$, $t_2 = \frac{5\pi}{12}$, $t_3 = \frac{7\pi}{12}$, and $t_4 = \frac{3\pi}{4}$.

then Eq. (24) becomes

$$c\phi_{cc} + \frac{4 - (\alpha\Gamma_1 c)^2}{4 + (\alpha\Gamma_1 c)^2} \phi_c = 4c \left((\alpha\Gamma_1 c)^2 + 4 \right) \phi_{\lambda}. \quad (25)$$

We seek a solution in the form $\phi(c, \lambda) = f(c)g(\lambda)$, and thus separating the variables gives two equations of the form

$$c \left((\alpha\Gamma_1 c)^2 + 4 \right) f''(c) + \left(4 - (\alpha\Gamma_1 c)^2 \right) f'(c) + 4\omega^2 c \left((\alpha\Gamma_1 c)^2 + 4 \right)^2 f(c) = 0,$$

$$g''(\lambda) + \omega^2 g(\lambda) = 0,$$

where ω is a constant. The solution $\phi(c, \lambda)$ should be bounded as $c \rightarrow 0$, and the corresponding solution of Eq. (25) is

$$\phi(c, \lambda) = R_{max} \cos(\omega\lambda) e^{-i\alpha\Gamma_1 \omega c^2} \left[-\omega c^2 (i\alpha\Gamma_1 - 2\omega) \mathcal{F}_1 + (i\alpha\Gamma_1 \omega c^2 - 1) \mathcal{F}_2 \right],$$

where \mathcal{F}_1 and \mathcal{F}_2 are defined in terms of the generalized hypergeometric functions ${}_1F_1$, evaluated with the following arguments:

$$\mathcal{F}_1 = {}_1F_1 \left(\frac{2i\omega + 2\alpha\Gamma_1}{\alpha\Gamma_1}, 3, 2i\alpha\Gamma_1 \omega c^2 \right),$$

$$\mathcal{F}_2 = {}_1F_1 \left(\frac{2i\omega + \alpha\Gamma_1}{\alpha\Gamma_1}, 2, 2i\alpha\Gamma_1 \omega c^2 \right).$$

The constant R_{max} can be chosen arbitrarily and denotes the maximum run-up height on the beach. Using the function $W(c, \lambda)$, an expression for $t(c, \lambda)$ can be obtained from Eq. (14),

$$t = \frac{\lambda}{2} - W.$$

Further, an expression for $x(c, \lambda)$ can be obtained from Eq. (12). Inserting $t(c, \lambda)$ from Eqs. (14) and (23) results in

$$x_c = -WW_c - c \left((\alpha\Gamma_1 c)^2 + 4 \right) \left(\frac{1}{2} - W_\lambda \right),$$

and in terms of the function ϕ , it becomes

$$x = -\frac{W^2}{2} - \frac{c^2}{8} \left((\alpha\Gamma_1 c)^2 + 8 \right) + \phi_\lambda.$$

The equation for the propagation speed gives us the free surface elevation as $\eta(c, \lambda) = c^2 + x(c, \lambda)$, and an expression for the velocity component $u(c, \lambda)$ is found from Eq. (23) to be

$$u = W - \frac{\alpha\Gamma_1}{2} (x + c^2).$$

While these formulae give representations of solutions of (1) and (2), it is not completely straightforward to understand these solutions in (x, t) -coordinates. Indeed, in order to plot these exact solutions in terms of (x, t) -coordinates, a numerical approach is needed. A direct approach has been outlined for the problem without a shear flow,⁴ but it is unclear whether this method will work in the current situation with non-zero vorticity. Therefore, let us briefly outline the numerical implementation. First, expressions for ϕ, W, t, x, η , and u , which are all functions of (c, λ) , are used to fill arrays of numbers as c and λ run through certain prescribed sets of values. In order to plot the free surface elevation as $\eta = \eta(x, t)$, we use the two matrices for $t(c, \lambda)$ and $x(c, \lambda)$ as independent variables and

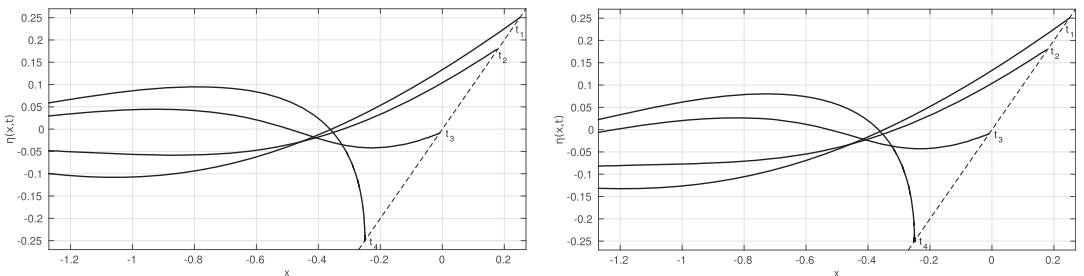


FIG. 5. Solution of a wave running up on a sloping beach. The left panel shows a solution with $R_{max} = 0.25$ and $\alpha\Gamma_1 = 0.25$. The right panel shows a solution with $R_{max} = 0.25$ and $\alpha\Gamma_1 = 0.50$. The solution is plotted at $t_1 = \frac{\pi}{4}$, $t_2 = \frac{5\pi}{12}$, $t_3 = \frac{7\pi}{12}$, and $t_4 = \frac{3\pi}{4}$.

tag the indices corresponding to certain values of x and t (to a prescribed tolerance). Then, we use these same indices in the matrix for η in order to find η as a function of x and t . With this simple scheme, plots of $\eta(x, t)$ are possible. The visualization of the horizontal fluid velocity $u = u(x, t)$ can be done in a similar way. The solution is single-valued so long as the Jacobian $\frac{\partial(x,t)}{\partial(c,\lambda)}$ is nonzero. Therefore, the constants R_{max} , α , Γ_1 , ω , and the arrays of (c, λ) are all chosen so that a single-value solution is obtained.

C. Discussion

The plots shown in Figs. 3–5 indicate how a background shear flow may affect the solutions of the shallow-water equations. Some of these effects are analyzed presently. Figure 3 focuses on the comparison between the solutions found here with small $\alpha\Gamma_1$ (solid curves) and solutions found using the method of Carrier and Greenspan (dashed curves). It can be seen that the main effect of the background vorticity is to induce a small setdown on the left-hand side (a minor downward deflection of the mean-water level). Note also that the construction laid down here depends on non-zero Γ_1 , so that the good agreement with the Carrier-Greenspan solutions validates our method.

Figure 4 shows two solutions with the same value of $\alpha\Gamma_1$, but with different amplitudes. We observe significant amplification of the wave as it moves up the slope. For example, comparing the amplitude at location $x = -0.8$ to the run-up amplitude reveals a magnification factor of about 2.75 for these waves in both cases.

Figure 5 focuses on the comparison of different strengths of vorticity. Here, it can be seen that while the run-up and run-down on the beach are identical, the amplitude of the wave on the left-hand side is smaller in the case of larger vorticity. Note that in these cases (as discussed in Sec. III), the parameter $\alpha\Gamma_1$ serves to measure the combined effect of the strength of the slope and the vorticity since this parameter appears prominently in the non-dimensional version of the equations.

In order to get more precise information on the influence of the vorticity on the amplification, we have run several more cases with varying values of $\alpha\Gamma_1$ and R_{max} . Notice that in the current analysis, it is the run-up height R_{max} which is chosen, and the offshore wave amplitude A_w is measured. From a practical point of view, it would be more sensible to measure the wave amplitude A_w so as to predict the run-up height R_{max} , and Tables I and II serve this purpose.

We note that the amplification factor depends on the background shear, in the sense that it grows with increasing vorticity. However, it appears that the main influence of the shear is the introduction of the offshore setdown mentioned above.

TABLE I. Run-up height R_{max} as a function of $\alpha\Gamma_1$ and wave amplitude A_w . Values for $R_{max} = 0.1$ and $R_{max} = 0.15$.

$\alpha\Gamma_1$	A_w	R_{max}	$\alpha\Gamma_1$	A_w	R_{max}
0.00	0.0403	0.10	0.00	0.0604	0.15
0.25	0.0396	0.10	0.25	0.0597	0.15
0.50	0.0355	0.10	0.50	0.0560	0.15

TABLE II. Run-up height R_{max} as a function of $\alpha\Gamma_1$ and wave amplitude A_w . Values for $R_{max} = 0.2$ and $R_{max} = 0.25$.

$\alpha\Gamma_1$	A_w	R_{max}	$\alpha\Gamma_1$	A_w	R_{max}
0.00	0.0806	0.20	0.00	0.1008	0.25
0.25	0.0796	0.20	0.25	0.1000	0.25
0.50	0.0765	0.20	0.50	0.0967	0.25

Again in the current mathematical description, the average water level at the shore is fixed to be zero so that the current situation corresponds to a shear-induced increase of the water level on the beach and in particular near the waterline. This finding is in line with the prediction of wind setup found, for example, in Ref. 22.

ACKNOWLEDGMENTS

This research was supported in part by the Research Council of Norway under Grant Nos. 213474/F20 and 239033/F20.

APPENDIX: DERIVATION OF THE SHALLOW-WATER EQUATIONS

For the sake of completeness, the shallow-water equations with a background shear flow over a sloping beach will be derived. This derivation complements other already existing asymptotic models with background shear, such as those presented in Refs. 1, 8, and 19. For a one dimensional flow, we consider the velocity component to be $V(x, z, t) = U(z) + u(x, t)$, where the linear shear current is given by $U(x, z) = \Gamma_1 \left(\frac{h}{2} + z \right)$ with Γ_1 being constant. For an incompressible and inviscid fluid, the equation for conservation of mass for the control interval delimited by x_1 and x_2 on the x -axis is written as

$$\frac{d}{dt} \int_{x_1}^{x_2} H(x, t) dx + \left[\int_{-h(x)}^{\eta(x,t)} V(x, z, t) dz \right]_{x_1}^{x_2} = 0,$$

where $H(x, t) = \eta(x, t) + h(x)$ is the total depth. Integrating in z yields

$$\int_{x_1}^{x_2} \eta_t + \left(\frac{\Gamma_1}{2} (h\eta + \eta^2) + uH \right)_x dx = 0.$$

Since x_1 and x_2 are arbitrary, the integrand must vanish identically so that we get the local mass balance equation

$$\eta_t + \left(\frac{\Gamma_1}{2} \eta (h + \eta) + uH \right)_x = 0. \quad (A1)$$

Next, we will consider the momentum balance in the x -direction. Recall that the only forces acting on the control volume are the pressure force and that the shallow-water approximation entails the assumption that the pressure is hydrostatic. The conservation of momentum is written as

$$\begin{aligned} \frac{d}{dt} \int_{x_1}^{x_2} \int_{-h}^{\eta} V dz dx + \left[\int_{-h}^{\eta} V^2 dz \right]_{x_1}^{x_2} + \left[\int_{-h}^{\eta} g(\eta - z) dz \right]_{x_1}^{x_2} \\ = - \int_{x_1}^{x_2} \alpha g(\eta + h) dx, \end{aligned} \quad (A2)$$

where the second term on the left is the momentum flux through the lateral boundaries of the control volume at x_1 and x_2 , and

the third term on the left is the pressure force on these lateral boundaries. The term on the right represents the pressure force in the negative x -direction due to the inclined bottom profile. The integral in the second term can be calculated to be

$$\int_{-h}^{\eta} V^2 dz = \Gamma_1^2 \left(\frac{h^2}{4} H + \frac{h}{2} (\eta^2 - h^2) + \frac{1}{3} (\eta^3 + h^3) \right) + \Gamma_1 (hH + \eta^2 - h^2) u + u^2 H.$$

Again, the integrand must vanish pointwise, so Eq. (A2) requires that

$$\begin{aligned} & \left(\frac{\Gamma_1}{2} (h\eta + \eta^2) + uH \right)_t \\ & + \left(\Gamma_1^2 \left(\frac{h^2}{4} H + \frac{h}{2} (\eta^2 - h^2) + \frac{1}{3} (\eta^3 + h^3) \right) \right. \\ & \left. + \Gamma_1 (hH + \eta^2 - h^2) u + u^2 H + \frac{g}{2} H^2 \right)_x = -\alpha g H. \end{aligned}$$

This equation can be simplified significantly by combining it with Eq. (A1). Removing terms of the form $[\frac{\Gamma_1}{2} h \cdot \text{Eq. (A1)}]$, $[u \cdot \text{Eq. (A1)}]$, and $[\Gamma_1 \eta \cdot \text{Eq. (A1)}]$, the equation becomes

$$u_t H + \frac{\Gamma_1^2}{4} h h_x H - \frac{\Gamma_1}{2} (h_x u + h u_x) H + u u_x H = -g \eta_x H.$$

Dividing through by $H(x, t)$ reveals that this equation is equivalent to

$$u_t + \left(\frac{\Gamma_1}{2} h \left(\frac{\Gamma_1}{4} h - u \right) + \frac{u^2}{2} + g \eta \right)_x = 0.$$

In particular, in the case of a linear bottom profile, the momentum equation (2) appears.

¹Ali, A. and Kalisch, H., "Reconstruction of the pressure in long-wave models with constant vorticity," *Eur. J. Mech. B Fluids* **37**, 187–194 (2013).

²Antuono, M. and Brocchini, M., "The boundary value problem for the nonlinear shallow water equations," *Stud. Appl. Math.* **119**, 73–93 (2007).

³Antuono, M. and Brocchini, M., "Analysis of the nonlinear shallow water equations over nonplanar topography," *Stud. Appl. Math.* **124**, 85–103 (2010).

⁴Antuono, M. and Brocchini, M., "Solving the nonlinear shallow-water equations in physical space," *J. Fluid Mech.* **643**, 207–232 (2010).

⁵Carrier, G. F. and Greenspan, H. P., "Water waves of finite amplitude on a sloping beach," *J. Fluid Mech.* **4**, 97–109 (1958).

⁶Carrier, G. F., Wu, T. T., and Yeh, H., "Tsunami run-up and draw-down on a plane beach," *J. Fluid Mech.* **475**, 79–99 (2003).

⁷Castro, A. and Lannes, D., "Fully nonlinear long-wave models in the presence of vorticity," *J. Fluid Mech.* **759**, 642–675 (2014).

⁸Choi, W., "Strongly nonlinear long gravity waves in uniform shear flows," *Phys. Rev. E* **68**, 026305 (2003).

⁹Constantin, A. and Varvaruca, E., "Steady periodic water waves with constant vorticity: Regularity and local bifurcation," *Arch. Ration. Mech. Anal.* **199**, 33–67 (2011).

¹⁰Courant, R. and Friedrichs, K. O., *Supersonic Flow and Shock Waves* (Springer-Verlag, 1999).

¹¹Curtis, C. W. and Kalisch, H., "Vortex dynamics in nonlinear free surface flows," *Phys. Fluids* **29**, 032101 (2017).

¹²Didenkulova, I., Pelinovsky, E., and Soomere, T., "Long surface wave dynamics along a convex bottom," *J. Geophys. Res.: Oceans* **114**(C7), 394–399, doi:10.1029/2008jc005027 (2009).

¹³Kharif, C. and Abid, M., "Whitham approach for the study of nonlinear waves on a vertically sheared current in shallow water," *J. Fluid Mech.* (to be published).

¹⁴*NIST Handbook of Mathematical Functions*, edited by Olver, F. W. J., Lozier, D. W., Boisvert, D. F., and Clark, C. W. (Cambridge University Press, New York, 2010).

¹⁵Richard, G. and Gavriluk, S., "The classical hydraulic jump in a model of shear shallow-water flows," *J. Fluid Mech.* **725**, 492–521 (2013).

¹⁶Rybkina, A., Pelinovsky, E., and Didenkulova, I., "Nonlinear wave run-up in bays of arbitrary cross-section: Generalization of the Carrier–Greenspan approach," *J. Fluid Mech.* **748**, 416–432 (2014).

¹⁷Shatah, J., Walsh, S., and Zeng, C., "Travelling water waves with compactly supported vorticity," *Nonlinearity* **26**, 1529 (2013).

¹⁸Teles da Silva, A. F. and Peregrine, D. H., "Steep, steady surface waves on water of finite depth with constant vorticity," *J. Fluid Mech.* **195**, 281–302 (1988).

¹⁹Thomas, R., Kharif, C., and Manna, M., "A nonlinear Schrödinger equation for water waves on finite depth with constant vorticity," *Phys. Fluids* **24**, 127102 (2012).

²⁰Vanden-Broeck, J.-M., "Periodic waves with constant vorticity in water of infinite depth," *IMA J. Appl. Math.* **56**, 207–217 (1996).

²¹Vasan, V. and Oliveras, K., "Pressure beneath a traveling wave with constant vorticity," *Discrete Contin. Dyn. Syst. B* **34**, 3219–3239 (2014).

²²Walton, T. L. and Dean, R. G., "Landward limit of wind setup on beaches," *Ocean Eng.* **36**, 763–766 (2009).

Paper B

Run-up of long waves on background shear currents

M. BJØRNESTAD

Wave Motion **96** (2020), 102551.



Run-up of long waves on background shear currents

Maria Bjørnestad

Department of Mathematics, University of Bergen, 5020 Bergen, Norway



ARTICLE INFO

Article history:

Received 19 November 2019

Received in revised form 23 March 2020

Accepted 24 March 2020

Available online 28 March 2020

ABSTRACT

Long waves in shallow water propagating over a background shear current towards a sloping beach are investigated, and exact solutions are found using a hodograph transform and separation of variables. Inspired by the work of Carrier and Greenspan on steady waves over a uniform beach profile in the irrotational setting, we study waves which propagate over a background shear current.

The shallow-water equations are obtained from the nonlinear Benney equations, and exact solutions are found with help of the hodograph transformation in conjunction with several further changes of variables. The hodograph transformation is effected by finding the Riemann invariants after the equations are written in the standard form of barotropic gas dynamics.

In the current work, the background flow features zero mass flux, as would be required by a real flow at a beach. Moreover, in contrast with previous work, the present approach allows separate study of the influence of the strength of the shear current and the slope of the bottom profile. This enables us to provide an estimate of the run-up as a function of the shear flow while keeping the bottom slope constant.

© 2020 Elsevier B.V. All rights reserved.

1. Introduction

In coastal seas, strong currents are often observed. Such currents will vary by depth and can for instance be established by tides, oceanic circulation, bottom friction, wind or wave breaking. The influence of background shear on water wave dynamics is known to be significant [1,2]. Several studies describing this kind of wave–current interaction have been done, see for example [3–8].

In the long-wave approximation it is reasonable to assume a background shear profile with linear variation in the vertical. As describe in [9], this assumption is justified when the surface waves are long compared with the water depth. Furthermore, it is convenient to consider the interaction between waves and a pre-existing current and to assume that the background current will be unaffected by the motion of the waves.

In particular, such a background current can be induced by the influence of a landward wind and the required return flow creates an undertow [10] which is flowing in the direction opposing the wave propagation. In the case of storm surge models, the variations of the mean-water level is a result of a combination of different processes where the most significant component is the wind set-up [11]. Therefore, it will be important to gain a better understanding about the role the wind stress-created current has on the shoaling process and the development of the waterline (run-up).

In the present work we enforce a background shear flow to have a zero net mass flux while long waves are propagating towards a linear beach profile. We derive the Benney equations from the classical Euler equations, followed by a reduction to the shallow water equations. These equations will then be solved exactly by a modification of Carrier and Greenspan's

E-mail addresses: maria.bjoernestad@gmail.com, maria.bjoernestad@uib.no.

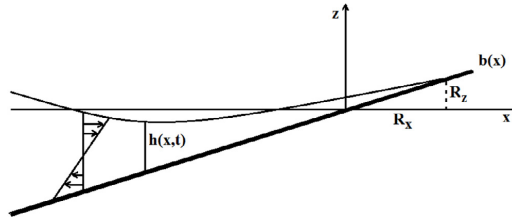


Fig. 1. Definition sketch of a plane sloping beach. The seabed is defined by $b(x) = \theta x$, and the water height is $h(x, t)$. The horizontal run-up is denoted by R_x and the vertical run-up is denoted by R_z . A shear flow with zero net mass flux is indicated on the left.

method [12]. The purpose of this work is twofold. First, this new approach will provide a more general way to solve the non-reducible shallow water equations by the use of the gas-dynamic analogy. Secondly, in contrast with [13], a more precise description in which role and impact the slope profile and the strength of vorticity have on the water wave dynamic and the water level near shore. In fact, studying different slopes indicates a natural scaling under which the equation is invariant.

In 1958, Carrier and Greenspan [12] solved the run-up problem of an irrotational flow on a linear beach where the exact solution gave a prediction of long waves at the beach. Our work is a modification of this model by including a background shear flow with zero net mass flux. An important step in the Carrier and Greenspan's methodology is to find the Riemann invariants for the system of equations. To overcome this difficulty, we will take the advantage of using the similarity between the shallow-water equations and the gas-dynamics equations as described in [14,15]. This analogy able us to use known methods from the gas-dynamics theory to find the Riemann invariants. Compared to the work in [13], this approach provides a more general way to solve the non-linear and non-reducible Benney equations.

There have been important generalizations of the method of Carrier and Greenspan. In particular, an approximate analytical solution of the boundary-value problem for the nonlinear shallow-water equations in the context of plane beaches were obtained in [16]. Based on the same method, initial conditions were used to study tsunami run-up and run-down in [17,18]. The final solution to the important problem of boundary and initial conditions was recently given in [19,20]. Moreover, the Carrier and Greenspan technique can also be generalized to apply to more complicated bathymetries than planar beaches. Applications of the method to base of arbitrary form and different beach profiles can be found in [21,22].

A recent paper [13] provided exact solutions to the shallow-water equations where a shear current and a beach profile were included. Here, a parameter $\alpha\Gamma$, where α is the slope steepness and Γ is the strength of the constant vorticity, is used to predict the wind set-up and indeed confirms that an increase of $\alpha\Gamma$, increases the wind set-up near shore. To obtain more precise description of the different roles of the constants α and Γ , we let them be separated during our current work.

The plan of the paper is as follows. In Section 2, the derivation of the Benney equations is presented and then followed by how to find the Riemann invariants through the gas-dynamic theory. It is shown how they can be used in a proper hodograph transformation together with changes of variables to obtain a single linear differential equation. The purpose of Section 3 is to provide an exact solution of the problem and to graphically present different approaches. In Section 4, our method and the results will be discussed.

2. Background shear flow on a sloping beach

The flow of an inviscid and incompressible fluid with a free surface can be described by the Euler equations with the kinematic and dynamic boundary conditions at the surface. In addition, the equation of mass conservation needs to be satisfied. If the fluid velocity is denoted by $\mathbf{u} = [u, w]$, where the horizontal component is denoted $u = u(x, z, t)$ and the vertical component is denoted $w = w(x, z, t)$, the mass conservation for an incompressible fluid is $\nabla \cdot \mathbf{u} = 0$. We consider long waves propagating only in the x -direction over a bottom described by $z = b(x)$. We assume that the undisturbed free surface is aligned with the x -axis and that $b(0) = 0$. In this way the waterline meets the bottom in the origin if no perturbation is present. The surface perturbation is denoted by $\eta(x, t)$, and the total water height is $h(x, t) = \eta(x, t) - b(x)$ as indicated in Fig. 1.

In order to derive the Benney equations, let us start with the kinematic condition at the free surface defined as $(\mathbf{n} \cdot \mathbf{u})_{z=h+b} = \mathbf{n} \cdot \mathbf{U}_{\text{interface}}$, where $\mathbf{U}_{\text{interface}}$ is the velocity of the surface and \mathbf{n} is the surface normal. The condition can be rewritten as

$$w = h_t + (h + b)_x u \quad \text{at} \quad z = h + b.$$

Integrating the equation of conservation of mass over the depth from $b(x)$ to $h(x, t) + b(x)$, and applying the equation above, gives us

$$h_t + \frac{\partial}{\partial x} \int_b^{h+b} u \, dx = 0. \tag{1}$$

With the assumption of long waves, the vertical momentum equation implies the hydrostatic law $P_z = -\rho g$ where P is the pressure, ρ is the fluid density and g is the constant of gravity. By this assumption, the x-component momentum balance is described by

$$u_t + uu_x + wu_z = -g(h + b)_x. \tag{2}$$

The third equation can be found by the integration $\int_b^z u_x + w_z \, dz = 0$ written as

$$w = - \int_b^z u_x \, dz + w|_{z=b}. \tag{3}$$

The three derived equations (1), (2) and (3) are called the Benney equations.

The horizontal velocity profile is defined with a shear current with zero net mass flux such that $\frac{1}{h} \int_b^{h+b} u \, dz = U$. By this definition we choose an appropriate expression for the background shear flow so that

$$u(x, z, t) = U(x, t) + \Omega \left(z - \left(b(x) + \frac{h(x, t)}{2} \right) \right)$$

has the depth-averaged velocity $U(x, t)$. Here the strength of the vorticity is denoted Ω and we are only interested in the case where $\Omega > 0$. Note that the approximation of $u(x, z, t)$ is justified if we consider long waves in shallow water. Together with this velocity profile and the second kinematic condition $\mathbf{n} \cdot \mathbf{u} = 0$ at $z = b(x)$, also written as $w|_{z=b} = ub_x$, Eq. (3) can be rewritten as

$$w = - \left(U_x - \Omega \left(b + \frac{h}{2} \right)_x \right) (z - b) + b_x \left(U - \Omega \frac{h}{2} \right).$$

Substituting the expression for $u(x, z, t)$ and the above expression for $w(x, z, t)$ into Eqs. (1) and (2), gives us the shallow water equations

$$h_t + (Uh)_x = 0, \tag{4}$$

$$U_t + UU_x + \frac{\Omega^2}{4} h h_x + g(h + b)_x = 0. \tag{5}$$

Before we continue, it is convenient to define the slope as $b(x) = \theta x$ and thereby the surface elevation is described by $\eta(x, t) = h(x, t) + \theta x$. If we now use Eq. (4) to rewrite Eq. (5) as the equation

$$(hU)_t + (hU^2 + p(h))_x = -gh\theta, \tag{6}$$

where $p(h) = \frac{1}{2}gh^2 + \frac{1}{12}\Omega^2h^3$, can we see the similarity to the gas-dynamic equations for a barotropic gas if we consider $P(h)$ as the 'pressure' and h as the 'density'. With this analogy, the characteristic speed and the Riemann invariants for our system of equations can be found in a more general way. In the common gas theory, see such as [14] and [15], if we let $c^2 = \frac{dp}{dh}$, the eigenvalues are given as $\lambda_{1,2} = U \pm c$ and the two Riemann invariants will have the form

$$\omega_{1,2} = U \pm \int \frac{c(h)}{h} \, dh + g\theta t.$$

The last term on the right hand side is added due to the bathymetry. We are now able to write the system of equations in characteristic form as

$$\left\{ \frac{\partial}{\partial t} + \lambda_{1,2} \frac{\partial}{\partial x} \right\} \omega_{1,2} = 0,$$

where

$$\lambda_{1,2} = U \pm \frac{1}{2} \sqrt{\Omega^2 h^2 + 4gh}$$

and

$$\omega_{1,2} = U \pm \left[\frac{1}{2} \sqrt{\Omega^2 h^2 + 4gh} + \frac{g}{\Omega} \ln \left(\sqrt{\Omega^2 h^2 + 4gh} + \Omega h + \frac{2g}{\Omega} \right) \right] + g\theta t.$$

We will now implement an appropriate hodograph transformation, which is to interchange the dependent variables with the independent variables. Let us first name α and β as characteristics variables and define them as $\alpha = \omega_1$ and

$\beta = \omega_2$. Instead of using U and h as our dependent variables in the transformation, we transform $\alpha = \alpha(x, t)$ and $\beta = \beta(x, t)$ to $x = x(\alpha, \beta)$ and $t = t(\alpha, \beta)$. Assuming a non-zero Jacobian $\frac{\partial(x,t)}{\partial(\alpha,\beta)}$, our equations become

$$\begin{aligned}x_\beta - \lambda_1 t_\beta &= 0, \\x_\alpha - \lambda_2 t_\alpha &= 0,\end{aligned}$$

which are still nonlinear in t . In order to obtain linearity, we define new independent variables as $\lambda = \alpha + \beta$ and $\sigma = \alpha - \beta$, and the above equations become

$$x_\lambda - Ut_\lambda + \frac{1}{2}\sqrt{\Omega^2 h^2 + 4gh} t_\sigma = 0, \quad (7)$$

$$x_\sigma - Ut_\sigma + \frac{1}{2}\sqrt{\Omega^2 h^2 + 4gh} t_\lambda = 0. \quad (8)$$

Assuming that $x_{\sigma\lambda} = x_{\lambda\sigma}$ and $t_{\sigma\lambda} = t_{\lambda\sigma}$, the two equations reduce to the following equation

$$2U_\sigma t_\lambda - 2U_\lambda t_\sigma - t_\sigma \left(\sqrt{\Omega^2 h^2 + 4gh} \right)_\sigma + t_\lambda \left(\sqrt{\Omega^2 h^2 + 4gh} \right)_\lambda = (t_{\sigma\sigma} - t_{\lambda\lambda}) \sqrt{\Omega^2 h^2 + 4gh}$$

and with the expressions for the new independent variables,

$$\frac{\lambda}{2} = U + g\theta t, \quad (9)$$

$$\frac{\sigma}{2} = \frac{1}{2}\sqrt{\Omega^2 h^2 + 4gh} + \frac{g}{\Omega} \ln \left(\sqrt{\Omega^2 h^2 + 4gh} + \Omega h + \frac{2g}{\Omega} \right), \quad (10)$$

we can write it as follows

$$\frac{\Omega^2 h + 3g}{\Omega^2 h + 4g} t_\sigma = \frac{1}{2} (t_{\lambda\lambda} - t_{\sigma\sigma}) \sqrt{\Omega^2 h^2 + 4gh}. \quad (11)$$

Here, h is only given implicitly as a function of σ in Eq. (10), but since the terms in Eq. (10) are both monotone and increasing, the relation can be inverted. The expression for $h_{\sigma\sigma}$ can be found using Eq. (10) to obtain

$$h_{\sigma\sigma} = \frac{2g}{(\Omega^2 h + 4g)^2},$$

and in this way, Eq. (11) turns into the linear equation

$$2t_h + ht_{hh} = (\Omega^2 h + 4g) t_{\lambda\lambda}.$$

3. Exact solution

To find a proper exact solution, it is more convenient to rewrite the equation using Eq. (9), such that

$$2U_h + hU_{hh} = (\Omega^2 h + 4g) U_{\lambda\lambda},$$

for then to introduce a 'potential function' as

$$U = \frac{1}{\Omega^2 h + 4g} \phi_h,$$

and end up with the following equation

$$4g\phi_h + h(\Omega^2 h + 4g)\phi_{hh} = (\Omega^2 h + 4g)^2 \phi_{\lambda\lambda}.$$

This second order differential equation can be solved by the method of separation of variables. We seek a solution which is bounded as $h \rightarrow 0$ and therefore by this method we choose the following solution

$$\phi(h, \lambda) = A \cos(k\lambda) \exp^{-ik\Omega h} [-(i\Omega - 2gk)\Omega h H_1 + (ik\Omega h - 1)H_2],$$

where H_1 and H_2 are defined in terms of the generalized hypergeometric function F_1^1 with the following arguments

$$H_1 = F_1^1 \left(\frac{2ikg + 2\Omega}{\Omega}, 3, 2ik\Omega h \right), \quad H_2 = F_1^1 \left(\frac{2ikg + \Omega}{\Omega}, 2, 2ik\Omega h \right).$$

Here, both A and k are constants which cannot be chosen completely arbitrary. Regarding several changes of variables, the solution is single-valued as long as the Jacobian $\frac{\partial(x,t)}{\partial(h,\lambda)}$ is nonzero. Therefore both A and k , as well as the constants θ and Ω , should be chosen such that the Jacobian is nonzero. In terms of the expression for ϕ , we proceed by finding the final expressions for x , t , and η depending on the variables h and λ . It now becomes clear why it is necessary to introduce

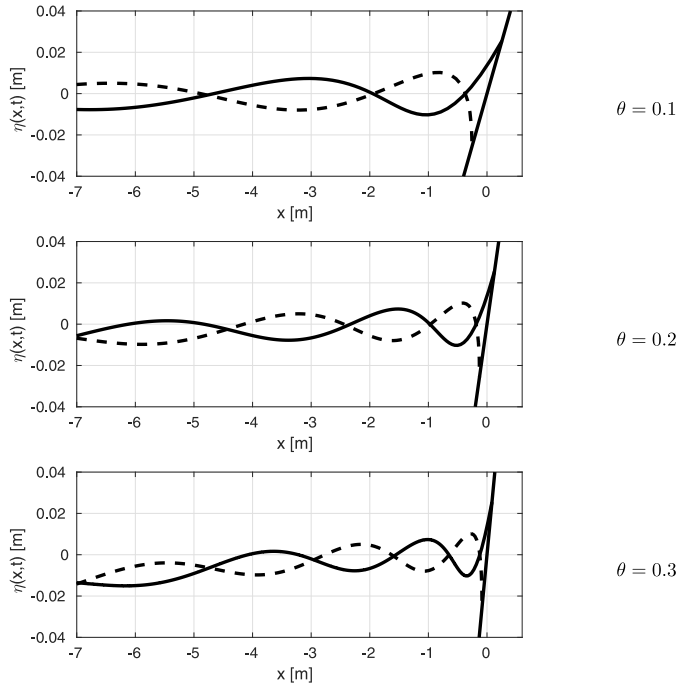


Fig. 2. The surface evolution with an increasing slope steepness. The parameters are $A = 0.5$, $k = 1$ and $\Omega = 0.5 \text{ s}^{-1}$. The solid curves represent the maximum run-up at time $t_1 = \frac{\pi}{4g\theta}$ and the dashed curves represent the minimum run-up at $t_2 = \frac{3\pi}{4g\theta}$.

the 'potential function', because with this approach we can simply choose to integrate Eq. (8) to find an expression for x as

$$x = \frac{1}{2g\theta} \left[-U^2 - \frac{1}{4} (\Omega^2 h + 8g) h + \phi_\lambda \right]. \tag{12}$$

By Eq. (9), $t(h, \lambda)$ can be expressed as

$$t = \frac{1}{2g\theta} (\lambda - 2U)$$

and as mentioned before the surface elevation is expressed as $\eta = h + \theta x$. The exact solution is plotted in Fig. 2 and in Fig. 3.

4. Discussion

To get more precise information about the run-up length R_x and the run-up height R_z , see Fig. 1, we let $h \rightarrow 0$ in Eq. (12). The U^2 -term goes to $A^2 \cos^2(k\lambda)$ and the ϕ_λ -term goes to $-Ak \sin(k\lambda)$, which means that the maximum run-up length has the expression $R_x = \frac{Ak}{2g\theta}$. With this expression found, the run-up height follows as $R_z = \frac{Ak}{2g}$. This simple approach shows that neither the run-up height nor the run-up length explicitly depends on the strength of the vorticity. This makes sense due to our mathematical description where the still water level is fixed to be zero at the shore. However, if we make a comparison between the run-up and the wave height further offshore, it becomes clear that the run-up is implicitly depending on the strength of the vorticity since the offshore wave height is decreasing with an increasing vorticity Ω , see Table 1. In this way, we can state that the background shear flow has an impact on the run-up.

In Fig. 2 the free surface elevation with the parameters $A = 0.5$, $k = 1$ and $\Omega = 0.5 \text{ s}^{-1}$ is plotted at the times for maximum and minimum run-up. With the steepness of the beach profile changing between the three different plots, we can consider the impact of the slope on the wave dynamics. Let us denote the first wave as the crest closest to the beach regardless of the run-up wave and then denote the second wave to be to the left of the first wave and so on. Note that

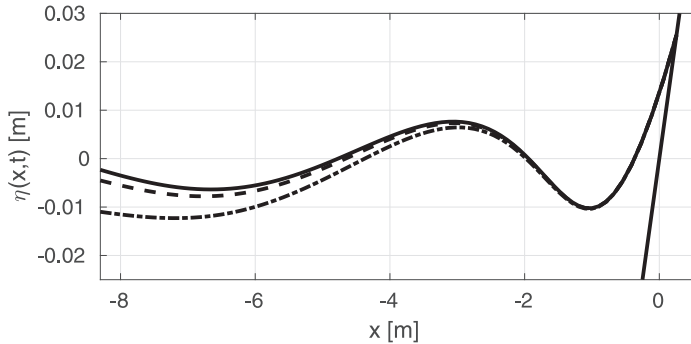


Fig. 3. The curves are plotted with the parameters $A = 0.5$, $\theta = 0.1$ and $k = 1$ at the maximum run-up time $t = \frac{\pi}{4g\theta}$. Solid curve with $\Omega = 0$, dashed curve with $\Omega = 0.5 \text{ s}^{-1}$ and dashed-dotted curve with $\Omega = 1 \text{ s}^{-1}$.

Table 1

The table shows the wave height at four fixed positions x with three different strength of vorticity. For all the calculated wave heights the required constants are set as $A = 0.5$, $k = 1$ and $\theta = 0.1$.

x [m]	Ω [s^{-1}]		
	0	0.5	1
-1.151	0.01867	0.01866	0.01864
-3.356	0.01482	0.01480	0.01475
-6.815	0.01253	0.01251	0.01242
-11.531	0.01103	0.01099	0.01086

the first wave in all three plots has the same wave height. The same occurs for the second and the third wave. At the same time, note that the length between the intersection points of the first wave in the first plot is twice the length of the first wave in the second plot and three times the length of the first wave in the third plot. The same structure occurs also for the second and third wave. This tells us that there is a symmetry in the scaling. In fact, by looking closer at Eq. (6), it is clear that the equation is invariant under the scaling $x \rightarrow \delta x$, $t \rightarrow \delta t$ and $\theta \rightarrow \delta \theta$.

The three solutions shown in Fig. 3 are all plotted with the same parameters $A = 0.5$, $\theta = 0.1$ and $k = 1$ at the maximum run-up time $t = \frac{\pi}{4g\theta}$, but with different strength of vorticity. Here, it appears that the main effect of an increase in the strength of the vorticity results in a larger set-down further offshore. As the water level near shore is fixed, note that due to the uniform shear flow there is a set-up close to shore which has been shown and explained as a wind induced set-up in [11].

Declaration of competing interest

The authors declare that they have no known competing financial interests or personal relationships that could have appeared to influence the work reported in this paper.

Acknowledgements

This research was supported in part by the Research Council of Norway under grants 213474/F20 and 239033/F20. Thanks to Sergey Gavriluyk for suggesting this approach and Henrik Kalisch for helpful discussions.

References

- [1] A. Ali, H. Kalisch, Reconstruction of the pressure in long-wave models with constant vorticity, *Eur. J. Mech. B Fluids* 37 (2013) 187–194.
- [2] A.F. Teles da Silva, D.H. Peregrine, Steep, Steady surface waves on water of finite depth with constant vorticity, *J. Fluid Mech.* 195 (1988) 281–302.
- [3] N.C. Freeman, R.S. Johnson, Shallow water waves on shear flows, *J. Fluid Mech.* 42 (2) (1970) 401–409.
- [4] I.G. Jonsson, in: B. LeMehaute, D.M. Hanes (Eds.), *Wave-Current Interactions*, in: *The Sea*, vol. 9, John Wiley, New York, 1990, pp. 65–120.
- [5] H. Kalisch, V. Teyekpiti, Hydraulic jumps on shear flows with constant vorticity, *Eur. J. Mech. B Fluids* 72 (2018) 594–600.
- [6] C. Kharif, M. Abid, Whitham approach for the study of nonlinear waves on a vertically sheared current in shallow water, *Eur. J. Mech. B: Fluids* 72 (2018) 12–22.
- [7] M.S. Longuet-Higgins, R.W. Stewart, The changes in amplitude of short gravity waves on steady non-uniform currents, *J. Fluid Mech.* 10 (4) (1961) 529–549.

- [8] D.H. Peregrine, Interaction of water waves and currents, *Adv. Appl. Mech.* 16 (1976) 9–117.
- [9] J. Touboul, J. Charland, V. Rey, K. Belibassakis, Extended mild-slope equation for surface waves interacting with a vertically sheared current, *Coast. Eng.* 116 (2016) 77–88.
- [10] I.B. Svendsen, Mass flux and undertow in a surf zone, *Coast. Eng.* 8 (1984) 347–365.
- [11] T.L. Walton, R.G. Dean, Landward limit of wind setup on beaches, *Ocean Eng.* 36 (2009) 763–766.
- [12] G.F. Carrier, H.P. Greenspan, Water waves of finite amplitude on a sloping beach, *J. Fluid Mech.* 4 (1958) 97–109.
- [13] M. Bjørnstad, H. Kalisch, Shallow water dynamics on linear shear flows and plane beaches, *Phys. Fluids* 29 (2017) 073602.
- [14] R. Courant, K.O. Friedrichs, *Supersonic Flow and Shock Waves*, Springer-Verlag, 1999.
- [15] S.L. Gavriluk, N.I. Makarenko, S.V. Sukhinin, *Waves in Continuous Media*, Springer International Publishing, 2017.
- [16] M. Antuono, M. Brocchini, The boundary value problem for the nonlinear shallow water equations, *Stud. Appl. Math.* 119 (2007) 73–93.
- [17] G.F. Carrier, T.T. Wu, H. Yeh, Tsunami run-up and draw-down on a plane beach, *J. Fluid Mech.* 475 (2003) 79–99.
- [18] U. Känäoğlu, C. Synolakis, Initial value problem solution of nonlinear shallow water-wave equations, *Phys. Rev. Lett.* 97 (14) (2006) 148501.
- [19] D. Nicolsky, E. Pelinovsky, A. Raz, A. Rybkin, General initial value problem for the nonlinear shallow water equations: Runup of long waves on sloping beaches and bays, *Phys. Lett. A* 382 (38) (2018) 2738–2743.
- [20] A. Rybkin, Method for solving hyperbolic systems with initial data on non-characteristic manifolds with applications to the shallow water wave equations, *Appl. Math. Lett.* 93 (2019) 72–78.
- [21] A. Raz, D. Nicolsky, A. Rybkin, E. Pelinovsky, Long wave runup in asymmetric bays and in fjords with two separate heads, *J. Geophys. Res.: Oceans* 123 (3) (2018) 2066–2080.
- [22] A. Rybkin, E. Pelinovsky, I. Didenkulova, Nonlinear wave run-up in bays of arbitrary cross-section: generalization of the Carrier–Greenspan approach, *J. Fluid Mech.* 748 (2014) 416–432.

Paper C


Extreme wave runup on a steep coastal profile

M. BJØRNESTAD AND H. KALISCH
AIP Advances **10** (2020), 105205.

Extreme wave runup on a steep coastal profile

Cite as: AIP Advances **10**, 105205 (2020); <https://doi.org/10.1063/5.0020128>

Submitted: 11 August 2020 . Accepted: 14 September 2020 . Published Online: 02 October 2020

M. Bjørnstad, and  H. Kalisch

COLLECTIONS

Paper published as part of the special topic on [Chemical Physics, Energy, Fluids and Plasmas, Materials Science and Mathematical Physics](#)



View Online



Export Citation



CrossMark

ARTICLES YOU MAY BE INTERESTED IN

[Impact of the confinement plate on the synthetic jet](#)


AIP Advances **10**, 105204 (2020); <https://doi.org/10.1063/5.0022813>

[Lead iodide and cesium lead halide perovskite highly oriented films deposited by spin coating](#)

AIP Advances **10**, 105305 (2020); <https://doi.org/10.1063/5.0011318>

[A Brewster incidence method for shocked dynamic metrology of transparent materials and its error evaluation](#)

AIP Advances **10**, 105203 (2020); <https://doi.org/10.1063/5.0023819>



Call For Papers!

AIP Advances

SPECIAL TOPIC: Advances in
Low Dimensional and 2D Materials

Extreme wave runup on a steep coastal profile

Cite as: AIP Advances 10, 105205 (2020); doi: 10.1063/5.0020128

Submitted: 11 August 2020 • Accepted: 14 September 2020 •

Published Online: 2 October 2020



M. Bjørnstad and H. Kalisch^{a)} 

AFFILIATIONS

Department of Mathematics, University of Bergen, P.O. Box 7800, 5020 Bergen, Norway

^{a)}Author to whom correspondence should be addressed: Henrik.Kalisch@uib.no

ABSTRACT

It is shown that very steep coastal profiles can give rise to unexpectedly large wave events at the coast. We combine insight from exact solutions of a simplified mathematical model with photographs from observations at the Norwegian coast near the city of Haugesund. The results suggest that even under moderate wave conditions, very large run-up can occur at the shore.

© 2020 Author(s). All article content, except where otherwise noted, is licensed under a Creative Commons Attribution (CC BY) license (<http://creativecommons.org/licenses/by/4.0/>). <https://doi.org/10.1063/5.0020128>

I. INTRODUCTION

In the present work, we are interested in the interaction of ocean waves with steep offshore topography such as encountered in some areas at the Norwegian coast. If surface waves propagate on such a steep bottom slope, they experience only slight amplification until very close to shore. However, just before they reach the beach face, the waves receive a large boost in amplitude, which can lead to an explosive run-up on the shore. As this large run-up may seem wholly unexpected to the casual observer, it may create a potentially hazardous situation.

It is well known that the Norwegian coast, especially in the south and the west, features a multitude of fjords.¹ These rocky cliffs often continue past the waterline, and may drop to several hundred meters depth, cutting through the continental shelf as submarine valleys. This landscape was formed by glaciers during the last ice age. Indeed, it is well known that fjords developed due to glaciers' capability of eroding below sea level,^{1,2} leaving deep submerged valleys when the ice age came to a close and melting was completed.

In some cases, these valleys are offshore of the present shoreline, and there are some places today where coastal platforms give way to very steep seaward slopes carved by these thick glaciers. In fact, it is not unusual to see 200 m or 300 m drops of the sea bed over a distance of a few hundred meters. These steeply sloping shores typically consist of bedrock, which has been smoothed by the glacial ice and is rather immune to erosion and littoral processes. In fact, wide stretches of the coast have not been filled with mud and other sediments, and the rocks remain exposed. As a result, this coast is generally classified as the primary coast,¹ similar to the coasts in other

places around the world such as New Zealand and the northernmost part of the East Coast of the United States.²

Further offshore, the Norwegian coast features very irregular bathymetry, which dissipates much of the incoming wave energy through wave focusing, shoaling, and local breaking.³⁻⁵ However, some long waves of moderate amplitude and steepness are able to pass the rugged offshore topography relatively unscathed and reach the coast. If these long waves hit an area with sharply sloping coastal profiles, even waves of relatively small amplitude can lead to large run-up. In what follows, in Sec. II, we report observations of waves made at a site with a sharp, nearly 1:1 drop from the water line. In Sec. III, we detail a mathematical model capable of predicting large run-up from a moderate-sized offshore wavefield in the case of bathymetry featuring a steep slope such as seen at the observation site. The results are discussed in Sec. IV.

II. OBSERVATIONS

Observations were made at a site near the Norwegian city of Haugesund. As shown in Fig. 1, the bathymetry near the coast features a steep drop to about 200 m right from the waterline. Indeed, it can be seen in the schematic of a cross section of the site in Fig. 2 that the slope is very steep, about 1:1. Due to the very steep slope, it is common for waves to exhibit surging breaking, such as defined in Refs. 6-8. However, as waves of slightly larger amplitude quickly shoal on the steep slope, they sometimes reach the point of plunging almost as soon as they can be made out as a large wave. One such example is shown in Fig. 3. Under the rough conditions prevailing when the photos in Fig. 3 were taken, energetic waves crash

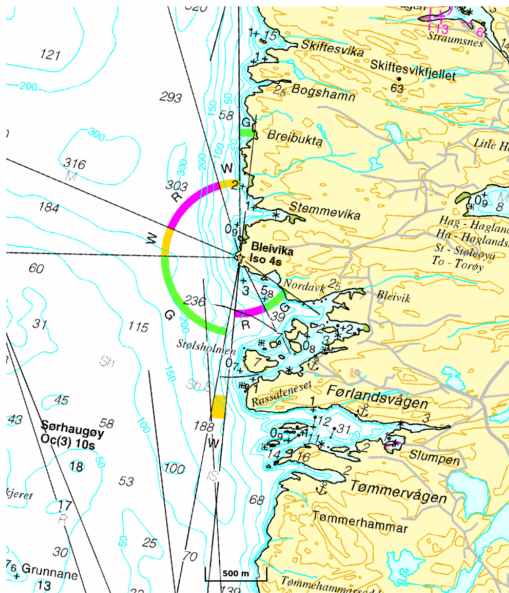


FIG. 1. Bathymetric chart of the sea bed near the Bleivika lighthouse. The depth contours run nearly parallel to the shore and feature a steep drop from the shoreline to about 200 m depth. Kartverket©. Used with permission from The Norwegian Mapping Authority.

into the rocks, creating large areas of turbulent flow. The accompanying foam and spray immediately alert the observer to the fact that wave conditions are serious, and caution must be exercised. On the other hand, the conditions in Fig. 4 were mostly calm with little visible swell, and only a small chop due to a moderate local wind. A few small patches of foam are visible, which appear to be remnants of previous waves interacting with the jagged rocks, or

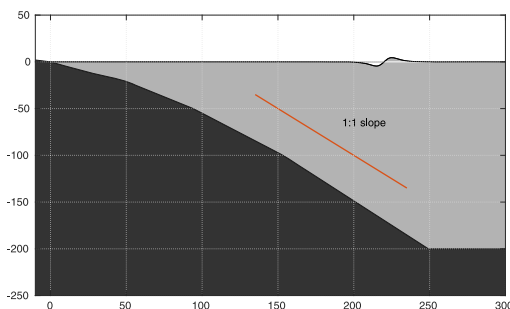


FIG. 2. Schematic of the sea bed near Stemmevika.

white-capping due to local wind gusts. The smaller swell waves were just lapping the shore, and the limited foam and absence of spray do not signal any danger. As a slightly larger swell wave approaches and shoals, the subsequent wave run-up appears to be extreme against the backdrop of otherwise benign wave and weather conditions. An example of such an explosive run-up is shown in Fig. 4, and one may argue that the flooding of the rocks may happen unexpectedly to a non-initiated observer.

A. Observations on January 16th, 2020

Observations were made from a location near the lighthouse Bleivika indicated by a star on the map in Fig. 1. We used an *Olymp Mark III E* camera to shoot 4 K video clips. Individual frames from those clips are shown in the figures below. Wave conditions were monitored using operational wave forecasts from two sources. First, the NOAA site⁹ gave an estimate of the significant waveheight and the peak period for the general area using an operational version of Wavewatch III. On this day, the significant waveheight was in the range 2 m–2.5 m, and the peak wave period was about 10 s.

Under local conditions, a forecast provided by the *BarentsWatch Center*¹⁰ was consulted. Near the coast, the waves had already encountered several shoals, and the waveheight and wave periods were somewhat smaller. The wind speed was above 9 m/s, therefore, there was a significant wind sea component in addition to swell. Most waves were surging breakers, but some waves were steep enough to break before reaching the shore. Figure 3 shows a wave developing along the steep sloping bottom. It can be seen that the waveheight develops quickly, and in this case, the wave is large enough for the wave to plunge before it hits the rocky shore. This situation would not pose a danger to the casual observer since wave conditions were not calm.

B. Observations on January 29th, 2020

In this case, the wave forecasts from NOAA and *BarentsWatch Center* estimated the local significant waveheight to be just above 1 m, with a maximum waveheight of about 2 m. Visually, conditions were rather calm, as also borne out from a study shown in Fig. 4. However, there was swell from a distant storm, and the peak wave period was about 13 s (i.e., wavelength of ~260 m based on linear wave theory). The authors were at the site for about 90 min, and the visually measured wave period was on the average about 9 s–13 s, though some waves were as short as 6 s, and some waves were longer than 13 s.

The rock, which can be seen in Fig. 4 stayed dry for the most part, though in the 90 min we were present, it was flooded 3 times. In fact, as far as we can tell, what typically seemed to happen was that a group of waves arrived, which had slightly higher than normal waveheight, and the rock was flooded not by the first, but by the second and/or third wave in the group. After such an incident, the conditions went back to normal. Indeed, it is well known that swell will organize into wave groups (see Refs. 11–13 and references therein), so the situation above would have to be expected. As mentioned above, in the 90-min observational period, there were three waves that flooded the rock, two of these in one wave group, and one in another wave group.



FIG. 3. This figure shows four snapshots of wave conditions at 59.48° N, 13.44° E on January 16th, 2020. Upper left: $t = 105$ s, upper right: $t = 115$ s, lower left: $t = 120$ s, lower right: $t = 124$ s.

Figure 4 shows a wave crest at $t = 15$ s (relative time in the video), an approximately flat surface at $t = 18$ s, and the wave trough at $t = 21$ s. This was a relatively unspectacular wave with a small waveheight hitting the rock. The next wave (not shown) already has

a larger amplitude, but stops short of the rock. Finally, 25 s later, at $t = 46$ s the third wave crest hits the rock, flooding the top of the rock almost entirely. Using tide tabulations, and a local elevation map, the run-up can be estimated to be about 3.8 m.



FIG. 4. This figure shows four snapshots of wave conditions at 59.48° N, 13.44° E on January 29th, 2020. Upper left: wave trough at $t = 15$ s, upper right: mean water level at $t = 18$ s, lower left: wave crest at $t = 21$ s, lower right: wave crest at $t = 46$ s.

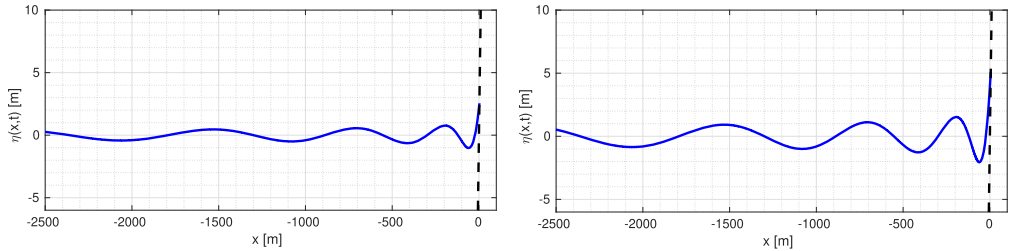


FIG. 5. Offshore wavefield and run-up on a 1:1 slope for two different offshore wave conditions. In the left panel, we have offshore amplitude 0.459 m and run-up 2.548 m. In the right panel, we have offshore amplitude 0.918 m and run-up 5.097 m.

III. MATHEMATICAL MODEL

In the following, it will be shown that a comparatively simple mathematical model can be used to understand how relatively small waves can lead to significant and unexpected run-up if encountering a steep slope. For this purpose, we will use the shallow-water system

$$h_t + (uh)_x = 0, \tag{1}$$

$$u_t + uu_x + g(h + b)_x = 0, \tag{2}$$

where $h(x, t)$ is the total depth of the fluid, $u(x, t)$ is the average horizontal velocity, g is the gravitational acceleration, and $b(x)$ is the bottom profile. In the present case, we define the bathymetry by $b(x) = \theta x$. The surface elevation is then given by $\eta(x, t) = h(x, t) + \theta x$.

This system is able to describe long waves in shallow water, and it is possible to find *exact* solutions in the presence of non-constant bathymetry, which enable us to make predictions of the development of the waterline. Exact solutions of 2×2 systems of conservation laws are classically obtained using a hodograph transformation, where dependent and independent variables are interchanged.¹⁴ In the presence of bathymetry, it is somewhat more difficult to find the requisite change of variables than in the case of constant coefficients. Nevertheless, an appropriate hodograph transformation was found by Carrier and Greenspan,¹⁵ and there have been a number of works seeking to extend and generalize that idea (see Refs. 16–21 and references therein).

In the present situation, it is important that the system be solved in *dimensional* coordinates in order to understand the influence of the steep bottom slope. For the convenience of the reader, the construction of the exact solutions is explained in the Appendix. As demonstrated in the Appendix, the independent variables λ and σ are introduced through a hodograph transformation. These variables do not have a clear physical meaning. However, using the separation of variables, an exact solution can be specified with the help of a “potential” ϕ defined in terms of the velocity u by the relation $u = \frac{1}{\sigma} \phi_\sigma$. In terms of the potential, the solution has the form

$$\phi(\sigma, \lambda) = \frac{A}{k} J_0(k\sigma) \cos(k\lambda). \tag{3}$$

Here, J_0 is the zeroth-order Bessel function of the first kind, and A and k are arbitrary constants. Using the potential ϕ , an expression

for $x(\sigma, \lambda)$ is found in the form

$$x = \frac{1}{2g\theta} \left(\frac{1}{2} \phi_\lambda - u^2 - \frac{\sigma^2}{8} \right), \tag{4}$$

and $t(\sigma, \lambda)$ can be expressed as

$$t = \frac{1}{2g\theta} (\lambda - 2u). \tag{5}$$

The surface elevation $\eta = h + \theta x$ is given by

$$\eta = \frac{1}{2g} \left(\frac{1}{2} \phi_\lambda - u^2 \right). \tag{6}$$

Note that in contrast to the solution provided in Ref. 15, the slope θ appears explicitly in the final solution.

This solution can now be used to investigate the run-up for various wave conditions. In Fig. 5, an exact solution is plotted with a steep slope of $\theta = 1$. In the left panel, we choose $A = 100 \frac{m^2}{s^2}$ and $k = 0.04 \frac{s}{m}$ (we emphasize that even though A and k feature units, there is no clear physical meaning assigned to these constants) in the solution to obtain an offshore amplitude of 0.459 m, and run-up 2.548 m. The steepness is defined as $2\pi a/L$, where L is the wavelength and a is the amplitude. In the right panel, we chose $A = 200 \frac{m^2}{s^2}$ and $k = 0.04 \frac{s}{m}$ to plot an offshore amplitude of 0.918 m with a steepness of 0.0059 and a run-up of 5.097 m. In Table I, the run-up for four different offshore amplitudes for waves with a period $T = 8$ s is recorded. The values of A used in the table are $50 \frac{m^2}{s^2}$, $100 \frac{m^2}{s^2}$, and $200 \frac{m^2}{s^2}$, $300 \frac{m^2}{s^2}$. The 8 s period is found by choosing

TABLE I. Run-up for four different offshore amplitudes for waves with period $T = 8$ s and varying steepness. The amplification factor between the offshore amplitude and the run-up is 5.5.

Amplitude (offsh.) (m)	Steepness (offsh.)	Period (s)	Run-up (m)
0.229	0.0015	8	1.274
0.459	0.0029	8	2.548
0.918	0.0059	8	5.097
1.377	0.0088	8	7.645

$k = 0.04 \frac{s}{m}$. The amplification factor between the offshore amplitude and run-up is 5.5.

IV. DISCUSSION

In this work, the run-up of waves on a steep slope has been studied through field observations at the Norwegian coast and a mathematical model. The observations presented here point to the possibility that extreme wave run-up may occur during otherwise benign conditions. The effect of the large run-up is further enhanced by the more moderate slope of the coast above the waterline (see Fig. 2), leading to a large area of flooding, such as shown in Fig. 4.

The mathematical model used here also shows that unusually large run-up can be realized on a steep slope by small offshore amplitudes. Indeed, it is evident from Table I that a moderate rise in the offshore amplitude from 0.459 m to 0.918 m may lead to a difference of more than 2.5 m in the run-up height. A still moderate wave amplitude of 1.377 m can lead to a run-up height of 7.648 m.

In summary, both observations and the shallow-water theory show that large run-up may occur under otherwise inconspicuous conditions. The two approaches do not give a perfect quantitative match because of the inherent quantitative uncertainty in the observations, and because some of the shorter waves observed are only shallow-water waves once they enter the coastal slope. Nevertheless, both observation and mathematical theory clearly show large amplification of the waves as they approach the shore, and it is clear that an observer focusing on offshore conditions may be taken by surprise as moderate waves experience such strong amplification and subsequent explosive run-up on the shore.

In the present work, we have focused on a very steep 1:1 slope where the bathymetry has a decisive effect on the wave evolution and the resulting run-up. It appears that in many previous studies on extreme wave events in shallow water, a gently sloping bottom was assumed. This is the case, in particular, in studies on the so-called sneaker waves, which are generally taken to be large run-up events on unusually large waves, or freak waves in shallow water, but not near the shore. For example, in Refs. 18 and 23, the authors describe freak wave occurrences in the nearshore zone, and in Refs. 25 and 26, the authors look at wave interaction phenomena as a possible route to freak wave development. In Ref. 27, laboratory experiments and numerical simulations are used to explain the occurrence of freak waves. In the situation considered in these works, even though the waves are in shallow water, the bathymetry does not exert a major effect on the fashion in which large wave events develop.

In contrast, a strong influence of the bathymetry on the wave conditions was found in Ref. 28, where resonant behavior due to irregular underwater topography was considered, and also in Refs. 29 and 30. However, the slopes considered in these works were still much gentler than the steep 1:1 bathymetry considered in the present work. On the other hand, the run-up on a vertical wall, such as a sea cliff were studied in Refs. 31 and 32.

There is a large literature on rogue or freak waves (see Refs. 33–39 and the references therein). It is not clear whether the present phenomenon should be classified as a freak wave event since at least in theory it can be predicted if measurements of the offshore

wavefield are available. Indeed, it would be interesting to conduct field measurements at this or a similar site, such as reported in the in-depth study.⁴⁰ However, under the conditions in this case such as the extreme slope, the slippery rocks, and small tidal range, it appears challenging to obtain reliable measurements.

ACKNOWLEDGMENTS

The authors wish to thank Professor Jarle Berntsen for helpful discussions, and two anonymous referees for providing pertinent comments for the improvement of this article. Funding from the Research Council of Norway under Grant No. 233039/F20 is acknowledged.

APPENDIX: EXACT SOLUTIONS FOR THE SHALLOW-WATER EQUATIONS

The shallow-water equations (1) and (2) are to be solved on a domain such as indicated in Fig. 6. As suggested in Ref. 41, a gas dynamics analogy may be used to find the eigenvalues and the Riemann invariants for the shallow-water system. Using (1) to rewrite (2) as

$$(hu)_t + (hu^2 + p(h))_x = -gh\theta, \quad (A1)$$

where $p(h) = \frac{1}{2}gh^2$, a similarity to the gas-dynamic equations for a barotropic gas can be seen if we consider $P(h)$ as the “pressure” and h as the “density.” For more details, the reader may refer to Ref. 14. Indeed, with this analogy, the eigenvalues are $\lambda_{1,2} = u \pm c$ and the Riemann invariants can be found to be

$$\alpha = u + \int \frac{c(h)}{h} dh + g\theta t, \quad (A2)$$

$$\beta = u - \int \frac{c(h)}{h} dh + g\theta t, \quad (A3)$$

where c is defined by $c^2 = \frac{dp}{dh}$. The last term on the right-hand side is due to the bathymetry. The system can then be written in terms of the characteristic variables $\alpha = u + 2\sqrt{gh} + g\theta t$ and $\beta = u - 2\sqrt{gh} + g\theta t$ as

$$\left\{ \frac{\partial}{\partial t} + (u + \sqrt{gh}) \frac{\partial}{\partial x} \right\} (u + 2\sqrt{gh} + g\theta t) = 0, \quad (A4)$$

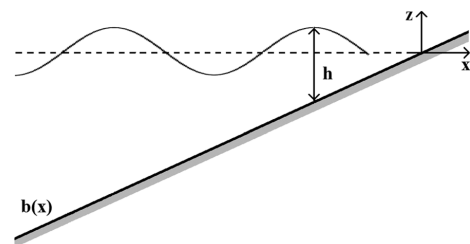


FIG. 6. Definition sketch for the mathematical model, including the slope $b(x)$ and the water depth $h(x, t) = \eta(x, t) - b(x)$.

$$\left\{ \frac{\partial}{\partial t} + (u - \sqrt{gh}) \frac{\partial}{\partial x} \right\} (u - 2\sqrt{gh} + g\theta t) = 0. \quad (\text{A5})$$

The hodograph transform can be effected by the implicit differentiation of the equations (A4) and (A5) and using the dependent variables $x = x(\alpha, \beta)$ and $t = t(\alpha, \beta)$, instead of $\alpha = \alpha(x, t)$ and $\beta = \beta(x, t)$. Assuming a non-zero Jacobian $\frac{\partial(x,t)}{\partial(\alpha,\beta)}$, the equations (A4) and (A5) become

$$x_\beta - \lambda_1 t_\beta = 0, \quad (\text{A6})$$

$$x_\alpha - \lambda_2 t_\alpha = 0. \quad (\text{A7})$$

In order to obtain a linear set of equation, we define new independent variables $\lambda = \alpha + \beta$ and $\sigma = \alpha - \beta$. The systems then appear as

$$x_\lambda - ut_\lambda + \sqrt{gh} t_\sigma = 0, \quad (\text{A8})$$

$$x_\sigma - ut_\sigma + \sqrt{gh} t_\lambda = 0. \quad (\text{A9})$$

Assuming that $x_{\sigma\lambda} = x_{\lambda\sigma}$ and $t_{\sigma\lambda} = t_{\lambda\sigma}$, the two equations reduce to

$$u_\sigma t_\lambda - u_\lambda t_\sigma - \left(\sqrt{gh} \right)_\sigma t_\sigma + \left(\sqrt{gh} \right)_\lambda t_\lambda = \sqrt{gh} (t_{\sigma\sigma} - t_{\lambda\lambda}). \quad (\text{A10})$$

Using the expressions for the new independent variables yields

$$\frac{\lambda}{2} = u + g\theta t, \quad (\text{A11})$$

$$\frac{\sigma}{4} = \sqrt{gh}. \quad (\text{A12})$$

By using (A11) and (A12), expressions for u_σ , u_λ , $\left(\sqrt{gh} \right)_\sigma$, and $\left(\sqrt{gh} \right)_\lambda$ can be found and (A10) turns into the linear wave equation

$$\sigma(t_{\lambda\lambda} - t_{\sigma\sigma}) - 3t_\sigma = 0. \quad (\text{A13})$$

Using the expression (A11) for λ together with an appropriate potential function $u = \frac{1}{\sigma} \phi_\sigma$, the Eq. (A13) can be rewritten as

$$(\sigma \phi_\sigma)_\sigma - \sigma \phi_{\lambda\lambda} = 0. \quad (\text{A14})$$

Using the separation of variables, we are able to find an exact solution, which is bounded as $\sigma \rightarrow 0$. This solution can be written as

$$\phi(\sigma, \lambda) = \frac{A}{k} J_0(k\sigma) \cos(k\lambda), \quad (\text{A15})$$

where J_0 are the Bessel function of the first kind of order zero, and A and k are constants.

With this solution in hand, an expression for $x(\sigma, \lambda)$ is found in the form

$$x = \frac{1}{2g\theta} \left(\frac{1}{2} \phi_\lambda - u^2 - \frac{\sigma^2}{8} \right), \quad (\text{A16})$$

and $t(\sigma, \lambda)$ can be expressed as $t = \frac{1}{2g\theta} (\lambda - 2u)$. The surface elevation $\eta = h + \theta x$ is then given by $\eta = \frac{1}{2g} \left(\frac{1}{2} \phi_\lambda - u^2 \right)$.

DATA AVAILABILITY

Data sharing is not applicable to this article as no new data were created or analyzed in this study.

REFERENCES

- T. Klemsdal, "Coastal classification and the coast of Norway," *Norw. J. Geogr.* **36**, 129–152 (1982).
- D. W. Johnson, *Shore Processes and Shoreline Development* (Wiley, 1919).
- J. Grue, "Nonlinear water waves at a submerged obstacle or bottom topography," *J. Fluid Mech.* **244**, 455–476 (1992).
- J. Falnes, "Research and development in ocean-wave energy in Norway," in *Proceedings of International Symposium on Ocean Energy Development*, edited by H. Kondo (Cold Region Port and Harbor Engineering Research Center, Murora, 1993), pp. 27–39.
- A. Chawla, H. T. Özkan-Haller, and J. T. Kirby, "Spectral model for wave transformation and breaking over irregular bathymetry," *J. Waterw. Port Coast. Ocean Eng.* **124**, 189–198 (1998).
- R. G. Dean and R. A. Dalrymple, *Water Wave Mechanics for Scientists and Engineers* (World Scientific, 1984).
- C. J. Galvin, "Breaker type classification on three laboratory beaches," *J. Geophys. Res.* **73**, 3651–3659, <https://doi.org/10.1029/jb073i012p03651> (1968).
- S. T. Grilli, I. A. Svendsen, and R. Subramanya, "Breaking criterion and characteristics for solitary waves on slopes," *J. Waterw. Port Coastal Ocean Eng.* **123**, 102–112 (1997).
- NOAA Wavewatch III, <https://polar.ncep.noaa.gov/waves/>, National Weather Service, USA.
- The BarentsWatch Centre, <https://www.barentswatch.no/en/services/Wave-forecasts/>, Wave forecast.
- W. Thompson, A. Nelson, and D. Sedivy, "Wave group anatomy of ocean wave spectra," in *Coastal Engineering Proceedings*, 1984.
- M. Longuet-Higgins, "Statistical properties of wave groups in a random sea state," *Philos. Trans. R. Soc. London* **312**, 219–250 (1984).
- G. Masselink, "Group bound long waves as a source of infragravity energy in the surf zone," *Cont. Shelf Res.* **15**, 1525–1547 (1995).
- R. Courant and K. O. Friedrichs, *Supersonic Flow and Shock Waves* (Springer, 1999).
- G. F. Carrier and H. P. Greenspan, "Water waves of finite amplitude on a sloping beach," *J. Fluid Mech.* **4**, 97–109 (1958).
- C. E. Synolakis, "The runup of solitary waves," *J. Fluid Mech.* **185**, 523–545 (1987).
- M. Antuono and M. Brocchini, "The boundary value problem for the nonlinear shallow water equations," *Stud. Appl. Math.* **119**, 73–93 (2007).
- I. Didenkulova and E. Pelinovsky, "Rogue waves in nonlinear hyperbolic systems," *Nonlinearity* **24**, R1–R18 (2011).
- M. Bjørnstad and H. Kalisch, "Shallow water dynamics on linear shear flows and plane beaches," *Phys. Fluids* **29**, 073602 (2017).
- M. Bjørnstad, *Shallow Water Dynamics on Linear Shear Flows and Plane Beaches* (Wave Motion, 2020).
- A. Rybkin, D. Nicolsky, E. Pelinovsky, and M. Buckel, *The Generalized Carrier-Greenspan Transform for the Shallow Water System with Arbitrary Initial and Boundary Conditions* (Water Waves, 2020).
- G. García-Medina, H. T. Özkan-Haller, P. Ruggiero, R. A. Holman, and T. Nicolini, "Analysis and catalogue of sneaker waves in the US pacific northwest between 2005 and 2017," *Nat. Hazards* **94**, 583–603 (2018).
- I. Nikolkina and I. Didenkulova, "Rogue waves in 2006–2011," *Nat. Hazards Earth Syst. Sci.* **11**, 2913–2924 (2011).
- I. I. Didenkulova, A. V. Slunyaev, E. N. Pelinovsky, and C. Kharif, "Freak waves in 2005," *Nat. Hazards Earth Syst. Sci.* **6**, 1007–1015 (2006).
- T. Soomere and J. Engelbrecht, "Weakly two-dimensional interaction of solitons in shallow water," *Eur. J. Mech. B: Fluids* **25**, 636–648 (2006).
- T. Soomere, "Rogue waves in shallow water," *Eur. Phys. J.: Spec. Top.* **185**, 81–96 (2010).
- J. Zhang, M. Benoit, O. Kimmoun, A. Chabchoub, and H.-C. Hsu, "Statistics of extreme waves in coastal waters: Large scale experiments and advanced numerical simulations," *Fluids* **4**, 99 (2019).
- T. S. Stefanakis, F. Dias, and D. Dutykh, "Local run-up amplification by resonant wave interactions," *Phys. Rev. Lett.* **107**, 124502 (2011).

- ²⁹K. Trulsen, H. Zeng, and O. Gramstad, "Laboratory evidence of freak waves provoked by non-uniform bathymetry," *Phys. Fluids* **24**, 097101 (2012).
- ³⁰O. Gramstad, H. Zeng, K. Trulsen, and G. K. Pedersen, "Freak waves in weakly nonlinear unidirectional wave trains over a sloping bottom in shallow water," *Phys. Fluids* **25**, 122103 (2013).
- ³¹N. Mirchina and E. Pelinovsky, "Increase in the amplitude of a long wave near a vertical wall," *Izv., Atmos. Oceanic Phys.* **20**, 252–253 (1984).
- ³²F. Carbone, D. Dutykh, J. M. Dudley, and F. Dias, "Extreme wave runup on a vertical cliff," *Geophys. Res. Lett.* **40**, 3138–3143, <https://doi.org/10.1002/grl.50637> (2013).
- ³³M. K. Ochi, *Ocean Waves: The Stochastic Approach* (Cambridge University Press, 1998).
- ³⁴M. Onorato, A. R. Osborne, M. Serio, and S. Bertone, "Freak waves in random oceanic sea states," *Phys. Rev. Lett.* **86**, 5831 (2001).
- ³⁵C. Kharif and E. Pelinovsky, "Physical mechanisms of the rogue wave phenomenon," *Eur. J. Mech. B: Fluids* **22**, 603–634 (2003).
- ³⁶K. Dysthe, H. E. Krogstad, and P. Müller, "Oceanic rogue waves," *Ann. Rev. Fluid Mech.* **40**, 287–310 (2008).
- ³⁷F. Fedele, J. Brennan, S. De Leon, J. Dudley, and F. Dias, "Real world ocean rogue waves explained without the modulational instability," *Sci. Rep.* **6**, 27715 (2016).
- ³⁸M. A. Donelan and A. K. Magnusson, "The making of the Andrea wave and other rogues," *Sci. Rep.* **7**, 44124 (2017).
- ³⁹E. Didenkulova, "Catalogue of rogue waves occurred in the world ocean from 2011 to 2018 reported by mass media sources," *Ocean Coast. Manage.* **188**, 105076 (2020).
- ⁴⁰G. Dodet, F. Leckler, D. Sous, F. Ardhuin, J. F. Filipot, and S. Suanes, "Wave runup over steep rocky cliffs," *J. Geophys. Res.* **123**, 7185–7205, <https://doi.org/10.1029/2018jc013967> (2018).
- ⁴¹S. L. Gavriluk, N. I. Makarenko, and S. V. Sukhinin, *Waves in Continuous Media* (Springer International Publishing, 2017).

Paper D


Internal flow properties in a capillary bore

W.Y. WONG, M. BJØRNESTAD, C. LIN, M.J. KAO, H. KALISCH, P. GUYENNE,
V. ROEBER, AND J.M. YUAN
Physics of Fluids **31** (2019), 113602.

Internal flow properties in a capillary bore

Cite as: Phys. Fluids **31**, 113602 (2019); <https://doi.org/10.1063/1.5124038>

Submitted: 27 August 2019 . Accepted: 22 October 2019 . Published Online: 13 November 2019

Wei-Ying Wong, Maria Bjørnstad, Chang Lin, Ming-Jer Kao, Henrik Kalisch , Philippe Guyenne, Volker Roeber, and Juan-Ming Yuan




View Online




Export Citation





CrossMark



CAPTURE WHAT'S POSSIBLE
WITH OUR NEW PUBLISHING ACADEMY RESOURCES

Learn more 



Internal flow properties in a capillary bore

Cite as: Phys. Fluids 31, 113602 (2019); doi: 10.1063/1.5124038

Submitted: 27 August 2019 • Accepted: 22 October 2019 •

Published Online: 13 November 2019



Wei-Ying Wong,¹ Maria Bjørnstad,² Chang Lin,¹ Ming-Jer Kao,¹ Henrik Kalisch,²  Philippe Guyenne,³ Volker Roeber,^{2,4,5} and Juan-Ming Yuan⁶

AFFILIATIONS

¹Department of Civil Engineering, National Chung Hsing University, Taichung 40227, Taiwan

²Department of Mathematics, University of Bergen, P.O. Box 7800, 5020 Bergen, Norway

³Department of Mathematical Sciences, University of Delaware, Newark, Delaware 19716, USA

⁴Université de Pau et des Pays de l'Adour, Anglet Campus, IPRA, EA4581, 64600 Anglet, France

⁵Department of Oceanography, University of Hawaii, 1000 Pope Road, Honolulu, Hawaii 96822, USA

⁶Department of Data Science and Big Data Analytics, Providence University, Taichung 43301, Taiwan

ABSTRACT

In this work, a detailed description of the internal flow field in a collapsing bore generated on a slope in a wave flume is given. It is found that in the case at hand, just prior to breaking, the shape of the free surface and the flow field below are dominated by capillary effects. While numerical approximations are able to predict the development of the free surface as it shoals on the laboratory beach, the internal flow field is poorly predicted by standard numerical models.

© 2019 Author(s). All article content, except where otherwise noted, is licensed under a Creative Commons Attribution (CC BY) license (<http://creativecommons.org/licenses/by/4.0/>). <https://doi.org/10.1063/1.5124038>

I. INTRODUCTION

Wave breaking is an important and ubiquitous phenomenon which happens virtually in all flows involving a free surface. As clearly brought out by a number of review articles and monographs,^{3,6,18,29,31,38,39,42,45} wave breaking has been a major focus of wave and ocean research for a long time. While it is well understood that wave breaking is central for the study of the energy budget of the oceans and air-sea interaction, it is also noted in the above works that the nature of wave breaking remains poorly understood. Indeed, wave breaking is a classical multiple-scale problem which exhibits a number of complicating factors in the flow such as circulation, turbulence, capillarity, and intermittency.

Wave breaking happens in many shapes and forms, and different types of breakings require a variety of methods for study. The object of the present paper is the study of a collapsing breaker on a moderate slope. Collapsing breakers appear on the margin between plunging and surging breakers, as found in the work by Galvin.²² Possibly because of their relatively rare occurrence, studies of collapsing breakers are few and far between. Indeed, collapsing breakers are not explicitly mentioned in Ref. 25, where the authors define a detailed classification of breaking waves on a planar beach in terms

of a single parameter S_0 based on the bottom slope, waveheight, and wavelength.

The focus of the present work is twofold. On the one hand, using new experiments performed in a wave flume at National Chung Hsing University in Taiwan, we aim to give a detailed description of the internal flow including velocity, Lagrangian acceleration, and pressure fields in the prebreaking stage of a capillarity-dominated collapsing breaker. In particular, we aim to describe details of the fluid flow below the free surface in order to identify a number of indicators for the onset of wave breaking.

Second, the internal flow field is compared with the results of numerical simulations using a Boussinesq model.⁴⁸ It is found that this numerical model has certain challenges when it comes to describing the internal flow field in a flow of this kind.

In order to create a collapsing breaker, a solitary wave of a certain waveheight is initiated with a wavemaker at one end of the wave flume. The wave propagates through the tank and starts deforming as it comes upon the slope located at the point $x = 0$. As the wave steepens, the wavefront starts to resemble a bore rushing onto the slope and eventually collapses without spilling or overturning. In this laboratory scale experiment, in the final stage before the bore collapses, the flow near the free surface is dominated by capillary

effects, which leads to interesting pressure anomalies. The shape of the bore just before breaking takes a *dolphin head*-like appearance, resembling similar profiles found in the context of capillary jumps such as discussed in Refs. 20 and 37. The shape of the wavefront is also similar to a spilling breaker in the presence of strong capillarity, such as discussed in Refs. 18 and 19.

The collapsing of the breaker is eventually indicated by the development of negative vertical velocity components which are necessitated by the acceleration due to the pressure anomalies resulting from strong capillarity. As the bore collapses, its internal flow structure resembles a plunging breaker (see, for example, Ref. 49) even though the free surface is still intact in the early stages of wave breaking. Eventually, as the toe of the capillary region gets ever more acute, it acts essentially as a hydrofoil, spoiling the free surface and creating a vortical motion in the breaking bore. The dynamics of the ensuing eddy motion could possibly be described numerically, but this is beyond the scope of the present article. Indeed, it is not clear whether existing point-vortex models such as, for example, those used in Ref. 15 will be able to capture the surface and eddy motion to a satisfactory degree of accuracy.

The disposition of the paper is as follows. In Sec. II, the experimental apparatus and setup are described. In Sec. III, the details of the flow field in a collapsing breaker are presented. Section IV contains a comparison with a numerical Boussinesq solver. Section V contains a brief conclusion.

II. EXPERIMENTAL TECHNIQUES

A. Experimental apparatus

The experiments were conducted in a wave flume located at the Department of Civil Engineering, National Chung Hsing University, Taiwan. The internal dimensions of the wave flume are 14.00 m long, 0.25 m wide, and 0.50 m deep. The bottom and two sidewalls of the wave flume were made of tempered glass to allow optical access. A piston-type wavemaker driven by a servo-motor is mounted at one end of the wave flume. The method proposed by Goring in Ref. 23 for generating the solitary wave is used. As shown in Refs. 33–36, highly repeatable solitary waves can be produced by this wavemaker.

A sloping beach made of tempered glass with a slope of 1:20 was installed in the wave flume. This is a moderately steep slope, much more gentle than the steep slopes used in Refs. 28 and 52. The toe of the sloping beach was fixed 6.48 m away from the wave paddle at rest. A Cartesian coordinate system with the origin $(x, y) = (0, 0)$ cm being located at the toe of the sloping beach is used. The x-axis is

oriented in the horizontal direction and measured positive onshore from the toe. The y-axis is oriented in the vertical direction and measured positive upward from the horizontal bottom. The schematic diagram of the experimental setup and coordinate system is shown in Fig. 1.

The free surface elevation was measured using two ultrasonic wave gauges. The first gauge located at $x = -150$ cm was used to measure the time series of free surface elevation η_0 and the waveheight H_0 for the incident solitary wave propagating over the horizontal bottom with a still water depth of h_0 . A voltage signal output from this wave gauge was employed to trigger the camera for capturing the images. Furthermore, the second gauge is placed at the toe at $x = 0$ cm to precisely identify the time, $t = 0$ s, at which the wave crest exactly reaches the toe. As shown in Fig. 1, $\eta(x, t)$ is the instantaneous wave profile and $h(x)$ is the still-water depth at a specified location over the sloping beach.

B. Flow visualization and velocity measurements

The structure of the prebreaking, breaking, and postbreaking waves was explored using flow visualization techniques (FVT) and high-speed particle image velocimetry (HSPIV) measurements. Titanium dioxide (TiO_2) was used for the seeding particles. These seeding particles have a refractive index of 2.6 and a mean diameter of $1.8 \mu\text{m}$, together with mean specific gravity and settling velocity (estimated by Stoke’s law) equal to 3.547 and 4.5×10^{-4} cm/s, respectively. The fall velocity is very small and thus ignored as compared with the typical velocity of interest in this study. An argon-ion laser head (Innova-300, Coherent Inc.) with a maximum power of 4 W was used as a light source. A fan-shaped laser light sheet (1.5 mm thick) was formed while the laser beam was guided by three reflection mirrors and then passed through the cylindrical lens. The light sheet, located 8 cm away from the glass sidewall, was eventually projected upward through the glass bottom of the wave flume to illuminate the seeding particles suspended uniformly in the water column. A high-speed digital camera (Phantom M310, Vision Research) with a maximum framing rate of 3260 Hz under the largest resolution of 1280×800 pixels was used to capture the images of both the free surface profile and the flow structure underneath the free surface.

The flow visualization images were captured by using a particle-trajectory photography method, with a high exposure time to allow the path-line of the particles to be captured. The framing rate and the exposure time of the high-speed camera for taking flow visualization images were 500 Hz and $1900 \mu\text{s}$. On the other hand, to

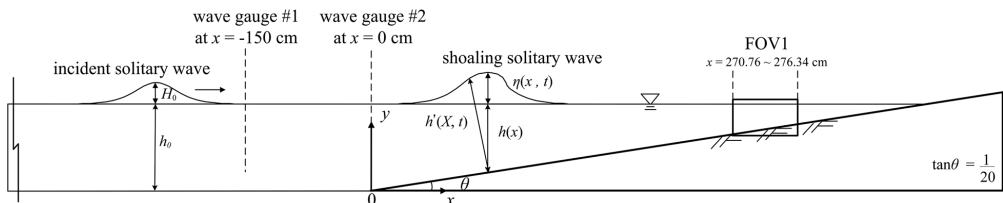


FIG. 1. Schematic diagram showing the coordinate system, the incident solitary wave, and the position of the field of view (FOV1).

ensure high time-resolved HSPIV measurements, the framing rate was 2000 Hz, much higher than FVT, and the exposure time was 490 μ s, smaller than FVT. The images of flow fields with the illuminated moving seeding particles were recorded continuously by using the high-speed camera. The free surface profile of the shoaling solitary waves, $\eta(x, t)$, was extracted from the images of the HSPIV measurements. The time interval in between each such image was very short, and a high-resolution record of $\eta(x, t)$ could be obtained. Furthermore, due to the mirror effect of the interface between the air and water, the particles on the free surface were illuminated by the laser light sheet and can be clearly identified.

One field of view (FOV1) was employed in this study. As shown in Fig. 1, the FOV1 was located between $x = 270.76$ cm and $x = 276.34$ cm, $y = 13.18$ cm and $y = 16.66$ cm. The width and height of FOV1 were 5.58 cm and 3.48 cm, respectively. The resolution was 4.356×10^{-3} cm/pixel. A cross-correlation calculation was used to determine the velocity vector from the images in which the brightness of the seeding particles had been intensified by using the Laplacian edge-enhancement technique.¹ The multipass PIV algorithm was then employed to calculate the instantaneous velocity field from three correlated images. The calculation is started from an interrogation window size of 64×64 pixels and ending with a window size of 8×8 pixels with a 50% overlap. Consequently, spurious vectors were removed by employing both global-range and median filters. Missing vectors are then interpolated to complete the whole velocity vector field.

C. Experimental conditions

An incident solitary wave with waveheight $H_0 = 1.12$ cm was created on water of an undisturbed depth of $h_0 = 14$ cm so that the ratio $H'_0 = H_0/h_0$ was equal to 0.08. The wave conditions are listed in Table I. Ten repeated runs were conducted for the HSPIV measurements. An ensemble average of all runs was used to describe the spatial or temporal variation of the velocity fields.

In order to obtain a collapsing breaker, the classification of Grilli *et al.*²⁵ was used. In that work, the authors define the parameter

$$S_0 = \frac{sL_0}{h_0},$$

where $s = \tan \theta$ is the slope, h_0 is the undisturbed depth prior to the sloping bottom, and L_0 is the wavelength. Following Ref. 25, the wavelength in Boussinesq's solitary wave theory is measured at the point of maximal slope on the wave profile, which leads to the relation

$$L_0 = \frac{2h_0}{\sqrt{3H'_0/4}} \operatorname{arctanh} \frac{\sqrt{3}}{3}.$$

With this definition of L_0 , S_0 is given in terms of the slope s and relative waveheight H'_0 by

$$S_0 = 1.521 \frac{s}{\sqrt{H'_0}}.$$

Grilli *et al.*²⁵ observed the following breaker types:

- spilling: $S_0 < 0.025$,
- plunging: $0.025 < S_0 < 0.3$, and
- surging: $0.3 < S_0 < 0.37$.

In the present case, we are using a slope of 1:20 so that $s = 0.05$. Since the relative waveheight is $H'_0 = 0.08$, the parameter value for the current experiment is $S_0 = 0.269$. Thus, the waveform used here is in the range of plunging breakers, but close to surging according to the classification above. As noted by Galvin,²³ some waves fall between plunging and surging and can be classified as collapsing breakers, and this is the case here.

III. DESCRIPTION OF THE FLOW

A. Wave generation and propagation

A solitary wave was generated in the wave flume by executing a quarter stroke with the piston wavemaker. The early stage of the evolution of the solitary wave was checked against a potential flow solver,^{24,26} where the solitary wave was generated numerically using a variant of Tanaka's method (see Refs. 14 and 51). The resulting time series can be seen in Fig. 2. Note that in both time series, there is a nearly perfect match between experimental data and numerical simulation.

B. Details of the wave breaking process

As the wave passes the toe of the sloping bottom, it starts to feel the upward slope and the wave starts to steepen. The slope provides a force in the direction opposing the wave motion, which eventually stops the motion. The reflection then leads to a rundown and backward motion. The rundown is not in focus in the present study.

As the wave collapses on the beach, there is little air entrainment. Moreover, the width of the tank is relatively small at 25 cm. With these restrictions, we notice that the flow is not being able to

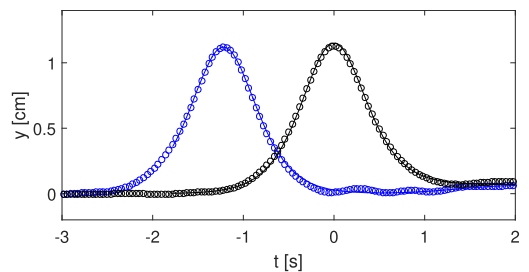


FIG. 2. Comparison of time series for solitary waves. The circles indicate the time series measured at two measuring stations in the wave flume. Blue: $x = -150$ cm. Black: $x = 0$. The solid curves indicate time series at two points in the numerical domain.

TABLE I. Experimental conditions.

H_0 (cm)	h_0 (cm)	H_0/h_0
1.12	14.0	0.080

form three-dimensional turbulent structures even in the postbreak- ing stage. In a sense, the flow is what one might call quasilaminar.

Next, we describe the details of the prebreaking development. From Fig. 3, it can be seen that fluid velocities near the top of the surging wave become larger. The wavefront gets steeper as more and more fluid concentrates behind the surging wavefront, creating a bulging “dolphin head” shape. A study of the individual terms in the Lagrangian acceleration, i.e., the terms $\frac{\partial u}{\partial t}$, $u \frac{\partial u}{\partial x}$, and $v \frac{\partial u}{\partial y}$, shows that the large velocities in Fig. 3 are not due to acceleration of fluid particles, but rather due to convective effects and concentration of fast

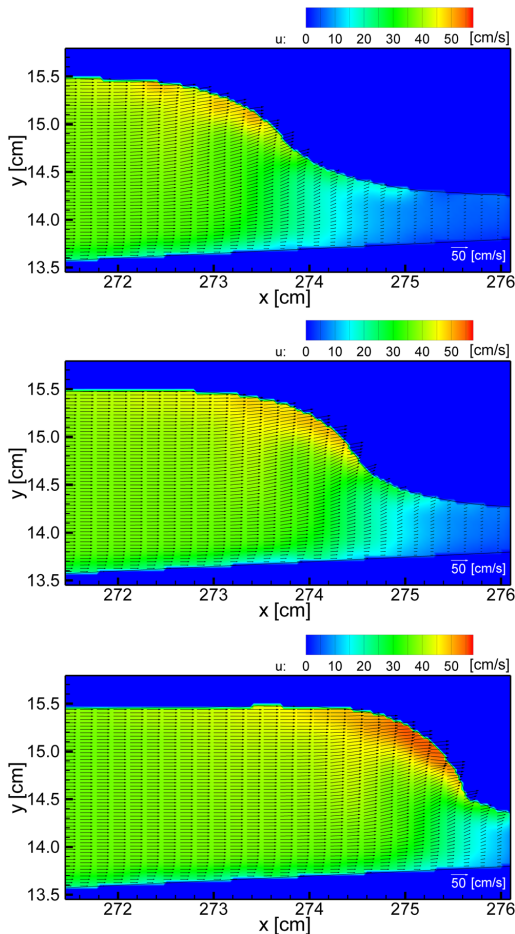


FIG. 3. Fluid particle velocities in FOV 1 at three times close to breaking: $t = 2.639$ s, $t = 2.652$ s, and $t = 2.669$ s (top to bottom). For reference, the long-wave speed is $c_0 \sim 38$ cm/s.

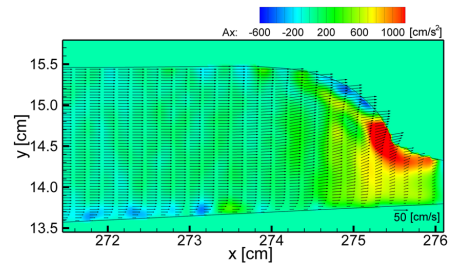


FIG. 4. Lagrangian accelerations at time $t = 2.666$ s. Fluid particles near the head of the wave experience a reduction in the horizontal velocity, while fluid particles near the toe of the wave experience horizontal acceleration in the direction of wave propagation. For comparison, the gravitational acceleration is $g = 981$ cm/s^2 .

particles behind the wavefront. In fact, consulting Fig. 4 shows that there is a fairly strong deceleration of particles behind the wavefront. As will be explained later, this deceleration is due to a large excess pressure just behind the wavefront due to capillary effects. The same capillary effects also contribute to acceleration of fluid particles in the free surface (cf. Fig. 5).

The onset of breaking may be defined as the first time the vertical velocity component of a particle behind the wavefront is negative. In Fig. 7, it can be seen that the vertical velocity component of particles in a larger and larger region starts to turn negative. This incipient downward motion constitutes the beginning of the creation of an internal circulation behind the wavefront.

In Fig. 5, particles in the free surface are being followed (manually), and it can be seen that these particles are accelerating while the free surface is decelerating. This feature seems to be common in waves approaching breaking. For example, similar behavior was found recently in deep-water waves which approach the breaking point.³⁰ It is also interesting to view these data in light of recent work⁷ where a universal breaking criterion was put forward. This criterion can be formulated in terms of the horizontal component of the fluid particle velocity at the crest u and the velocity of the crest itself c , and it states that a wavetrain is liable to feature wave breaking if the ratio $B = u/c$ exceeds the threshold 0.85–0.86, which is in contrast to the usual convective criterion (see Ref. 12 and references therein) which places the critical value at about 1. In the present case, as the wave enters the slope, it forms a steep front so that there is no well defined wave crest. Nevertheless, using the data shown in Fig. 5, we may compare the front velocity to the horizontal component of the particle velocity. A representative result is shown in Table II. Note that the value $B \sim 0.87$ is achieved about 0.003 s before the wave starts to break (cf. Fig. 7).

Finally, let us explain the role of capillarity in the prebreaking development of the wave. The horizontal momentum balance is written in terms of the horizontal component of the velocity field u and the stress vector σ_x as

$$\rho \frac{Du}{Dt} = \nabla \cdot \sigma_x,$$

where $\frac{D}{Dt}$ represents the material (Lagrangian) derivative and ρ is the fluid density. Given that the fluid velocity near the wavefront is

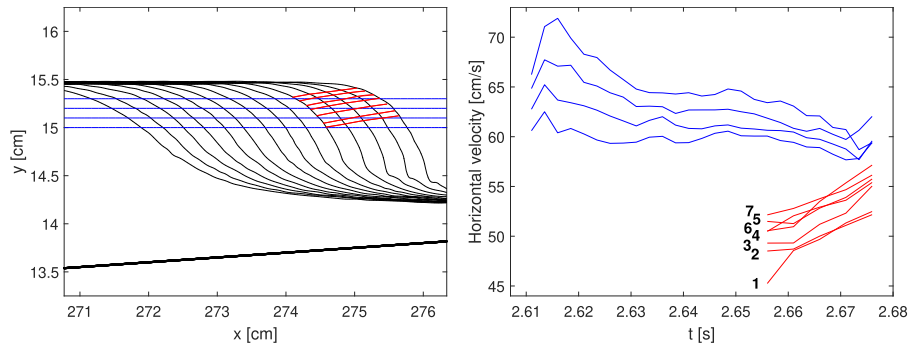


FIG. 5. Comparison between front velocity and fluid particle velocities. The blue curves in the right panel show the velocity of the free surface at a number of fixed vertical locations which are indicated as straight lines in the left panel. The ordering of the blue curves in the right panel by height corresponds to the same ordering as that in the left panel. In particular, the highest vertical location features the highest front velocity. The free surface in the left panel is indicated at a time step of 0.005 s, from $t = 2.611$ s to $t = 2.676$ s. As the front steepens, the front velocity decreases slightly over time. The red curves show the horizontal component of the velocities of fluid particles inside the free surface. The red curves in the left panel show the approximate position of fluid particles and are ordered from the top to the bottom. The ordering is indicated by arabic numerals in the right panel. The horizontal particle velocities increase over time.

similar to the velocity of the wave itself, we do not expect boundary layer effects to be dominant at the free surface so that the momentum balance reduces to

$$\frac{Du}{Dt} = -\frac{p_x}{\rho},$$

where p is the fluid pressure. Now from Fig. 4 which shows the Lagrangian acceleration in the x direction, we see that $\frac{Du}{Dt}$ is negative in the upper part of the wave. Thus, according to the above formula, the pressure p increases in the direction of wave propagation in the upper part of the wave. In contrast, in the lower part of the wave (red part), the Lagrangian acceleration $\frac{Du}{Dt}$ is positive so that the pressure decreases in the direction of wave propagation.

These findings can be explained by looking at the free surface condition with capillarity. Indeed, the balance of forces is written in terms of the fluid pressure p , the atmospheric pressure p_a , the free surface excursion η , and the capillary parameter τ as

$$p - p_a = -\tau \frac{\partial^2 \eta / \partial x^2}{[1 + (\partial \eta / \partial x)^2]^{3/2}}.$$

This formula clearly shows that near the head of the wave, where the free surface is convex, the fluid pressure is above atmospheric (i.e., the gauge pressure $p - p_a$ is positive), while near the bottom of the wave, the fluid pressure is below atmospheric since the free surface is concave.

Thus, as indicated in Fig. 6, there is an acceleration of fluid particles on the free surface, while particles behind the leading front of

the wave are decelerated. Moreover, together, these pressure conditions also lead to acceleration of fluid particles near the middle of the leading front in the negative y -direction. After carefully analyzing the data using HSPIV method, it was indeed found that the internal velocity field under the head of the wave develops negative vertical velocity components (see Fig. 7).

IV. COMPARISON WITH THE BOUSSINESQ MODEL

As there are no closed-form solutions of solitary waves propagating and breaking on a slope, the experimental data will be compared to simulations done with a Boussinesq model. There are some theoretical works providing nearly closed-form solutions for standing waves on a slope (see Refs. 10, 13, and 50), but in the present situation, numerical simulation is the only reasonable choice.

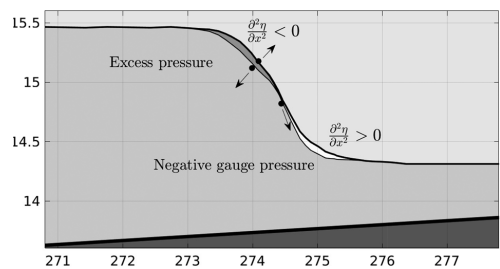


FIG. 6. This schematic explains the acceleration experienced by various fluid particles. Due to the curvature of the free surface, there is an excess pressure near the head of the wave and a pressure deficit near the toe of the wave. These pressure differentials cause fluid particles to be accelerated in different directions.

TABLE II. Breaking onset parameter $B = ulc$ as a function of time t .

t (s)	2.656	2.661	2.666	2.671	2.676
B	0.75	0.77	0.78	0.84	0.87

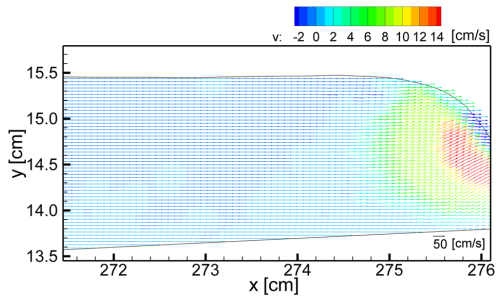


FIG. 7. Vertical velocity behind a wavefront in a solitary wave shoaling on a 1:20 slope. Incipient breaking stage at $t = 2.679$ s.

A. Model description

The Boussinesq Ocean and Surf Zone (BOSZ) model is a phase-resolving Boussinesq-type model for the computation of nearshore waves, wave-driven currents, infragravity oscillations, and ship wake waves (see, for example, Refs. 16, 32, 46, and 47). The governing equations are based on a conserved variable formulation of Ref. 41. The numerical solution handles the nonlinear shallow water part of the governing equations with a finite-volume scheme based on a total-variation diminishing (TVD) reconstruction method of up to 5th order and a Riemann solver. This combination ensures robust and accurate computation of fast flows over irregular terrain including moving boundaries (wet/dry cell interfaces). The frequency dispersion terms are based on a central-difference scheme of second order. Time integration is carried out with an adaptive Runge-Kutta time-stepping scheme, allowing up to 4th order accuracy. For most computations, such as this test case, a 2nd order time integration is sufficient; however, some problems with more dispersive waves require at least a 3rd order integration scheme. Due to the presence of space-time derivatives of the evolution variables in the momentum equations, systems of equations have to be solved to extract the flow speed at the end of each time step. The two systems are directionally independent of each other with

data-dependencies arising only in the x - or the y -directions, respectively. The bottom friction is accounted for through the widely used Manning-Strickler formula based on a roughness coefficient, which represents the surface property of the experimental layout. Here, we choose $n = 0.012s/m^{1/3}$ to match the smooth laboratory slope.

The input waves are generated at the left boundary in various forms. For the present case, the solitary wave was generated in two ways: (a) with an analytical solution at the boundary and (b) by feeding a time series from the wave gauge through the boundary. The flow velocity at the boundary is set by long wave theory in the form $u = \eta\sqrt{g/h_0}$. As shown in Fig. 8, both methods have led to near-perfect replication of the input wave conditions.

B. Reduction of dispersion based on the free-surface Froude number

As the flow depth becomes very shallow on the slope, wave breaking has to be incorporated locally into the Boussinesq model. As Boussinesq models do not have an inherent wave-breaking mechanism, a numerical criterion needs to be used in order to maintain stability. The strategy used here is based on the *free surface Froude-number* Fr , which can be determined from the free surface flow velocities. The governing equations allow for calculation of the flow velocity at any position in the water column based on the horizontal velocities and under the assumption of a prescribed quadratic velocity profile used in the derivation of the Boussinesq system.

We know that for $Fr > 1$, the flow becomes supercritical and bores can develop. Therefore, if the free surface Froude-number exceeds 1.0, the dispersion terms are locally and momentarily set to zero, i.e., the solution reduces to the hyperbolic nonlinear shallow-water equations in the cells around the wave breaking front. The local *Froude number* at the free surface is determined by

$$Fr_{loc} = \sqrt{u_{y=\eta}^2} / \sqrt{g(h_0 + \eta)},$$

where the velocity at the free surface is given by the quadratic profile, which arises from the Taylor series expansion of the horizontal velocity which is usually employed in Boussinesq type models.⁴¹ Since the model code checks for the Fr -number criterion at each time step, the solution at the wavefront can dynamically switch

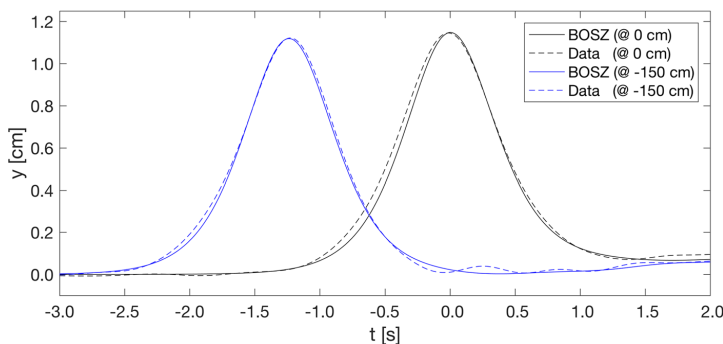


FIG. 8. Comparison between the numerical solution from BOSZ and the experimental data for the free surface elevation at the two wave gauges (−150 cm and 0 cm, respectively; see Fig. 1 for the layout).

between the full Boussinesq-type solution and the hydrostatic non-linear shallow-water equations. Similar methods for the detection and treatment of wave breaking were tested in Refs. 4, 5, 9, and 27 and compared to data from Refs. 21, 50, and 55. In particular, this is in contrast to the typical wave steepening observed in hyperbolic models.⁴⁴ One may also use the quadratic ansatz used in many Boussinesq models to reconstruct the velocity profile at any point in the fluid column (see Ref. 11, for example), though better results would be expected using higher-order reconstructions (see Ref. 54) or full Euler or Navier-Stokes equations.^{36,8}

C. Comparison

Considering the results over the small PIV window, the BOSZ model computes the shape of the collapsing bore reasonably well. Particular snapshots show very good agreement (see Fig. 9). The wave steepness depends mostly on the grid spacing. $\Delta x = 0.50$ cm shows good agreement, whereas $\Delta x = 0.75$ cm and $\Delta x = 0.25$ cm lead to a slightly gentler and steeper bore front. In more detail, note

that within FOV1 shown in Fig. 9, the BOSZ code essentially solves a shallow-water system due to the breaking criterion switching off the dispersive parts. While the numerical solver does not feature molecular viscosity, it features numerical dissipation, and it appears that with a grid size of $\Delta x = 0.75$ cm, there is just the right amount of dissipation to slow the hyperbolic steepening so that very good agreement with the experimental data is obtained (see the leftmost curve in the lower panel of Fig. 9). On the other hand, the numerical model does not incorporate capillarity, which is the reason for the poor agreement with the experimental data in the rightmost curve in the lower panel of Fig. 9. With decreasing grid size, $\Delta x = 0.50$ cm and $\Delta x = 0.25$ cm, the numerical dissipation weakens and more pronounced hyperbolic steepening is observed in the numerical solutions. This choice yields a simulation which is closer to the hyperbolic nature of the equations to be solved, but the comparison with the experimental data is not as good (see the leftmost curves in upper and middle panels of Fig. 9). However, this choice leads to a better comparison with the capillary region further up the slope as can be seen in the rightmost curves in the upper and middle panels

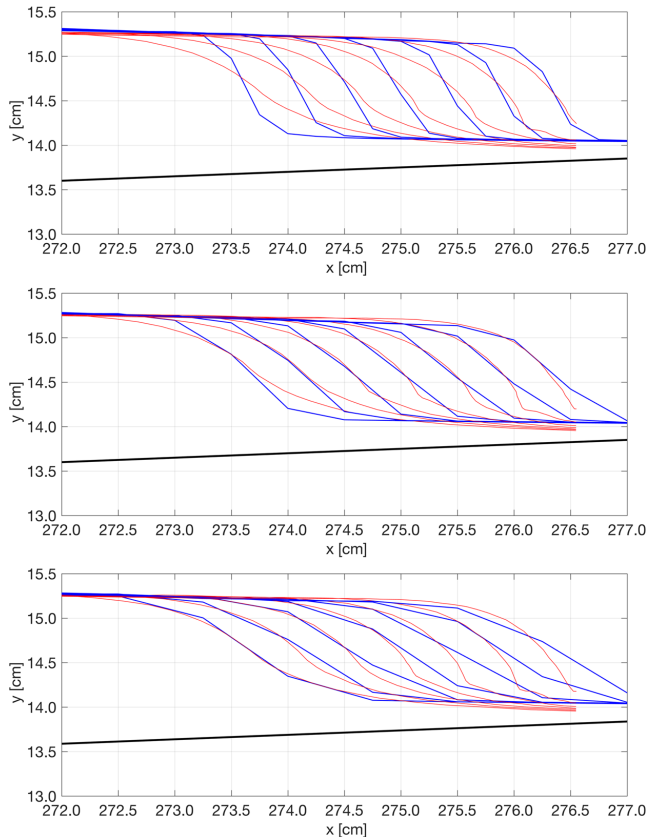


FIG. 9. Comparison of the free surface envelope from experimental data with the numerical computation from the BOSZ code. Upper panel: $\Delta x = 0.25$ cm; middle panel: $\Delta x = 0.50$ cm; lower panel: $\Delta x = 0.75$ cm. The blue curves represent solutions from BOSZ, and the red curves show the free surface derived from video images of experimental data. The code is able to give overall correct answers for the wave transformation and runoff. Details in the structure of the wavefront and wave toe differ from the data, probably due to the lack of capillarity in the governing equations of BOSZ.

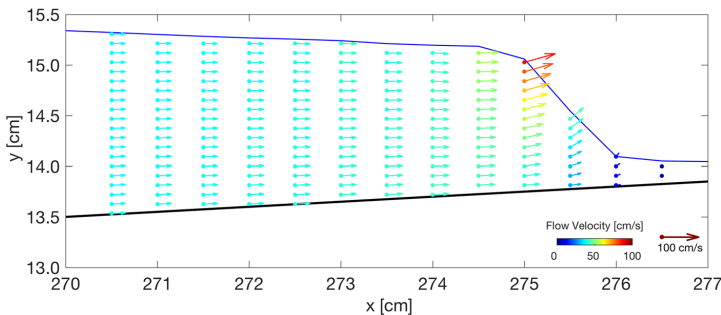


FIG. 10. Reconstruction of the velocity field from the numerical solution of the BOSZ model with grid size $\Delta x = 0.5$ cm.

of Fig. 9. The velocity field can be reconstructed using the quadratic ansatz inherent in the Boussinesq model. An example is shown in Fig. 10. As can be seen in this Fig. 10, the intricate features of the velocity field due to capillarity at the bore front are not captured by the Boussinesq model. This is to be expected as capillarity is not part of the Boussinesq model since it is generally a long-wave model.

D. Wave runup

The measured maximum run-up height for 14 cm still water depth and waveheight to water depth ratio being 0.08 is $R = 3.154$ cm. With $n = 0.012\text{s}/\text{m}^{1/3}$, the computed maximum runup agrees exactly with the measured runup of 3.154 cm. The computed maximum runup is the highest cell on the straight slope that was wet at any time during the computation. This corresponds to a minimum water depth of 0.001 cm.

V. CONCLUSION

In a certain sense, one may view collapsing breakers as a hybrid between a plunging and a surging breaker. In a surging breaker, the steep slope provides a strong force in the negative x -direction (i.e., in the direction opposed to the propagation of the wave). This force is indeed strong enough to slow the wave, eventually arresting the wave motion without breaking.

In a spilling breaker, the slope is comparatively gentler, the force in the negative x -direction comparatively smaller, and the waveheight comparatively larger. As a result, the fluid motion in the lower half of the wave is inhibited while the force distributed through the fluid from the sloping bottom is not strong enough to arrest the fluid motion in the upper half of the wave. Thus, the upper half of the wave overtakes the lower half, leading to the well known formation of a jet. As the leading part of the jet feels gravity and starts to fall, a reconnection with the lower part of the wave is formed, and wave breaking ensues.

The collapsing breaker appears to represent a balance where the pressure forces provided by the slope are strong enough to slow the fluid motion in the whole of the wave, but not strong enough to prevent it from breaking. As a result, one may observe something which resembles an “internal plunging breaker.” This observation is most apparent when looking at camera footage from the PIV system, but can also be observed in Fig. 7.

Since a delicate balance between the bottom slope and the waveheight is required, collapsing breakers are not widely observed in the field. Nevertheless, there are accounts of collapsing breakers in the literature. For example, a photograph of a collapsing breaker is given on page 56 in Ref. 45. The importance of capillarity is usually gauged by looking at the Bond number $\rho g L^2 / \tau$, for a length scale L . For large breakers such as the one shown in Ref. 45, the Bond number is large, and capillarity is not expected to play a decisive role.

On the other hand, the distinctive features of a collapsing breaker at the laboratory scale such as those discussed in the present paper are provided by capillarity. As shown in Fig. 4, the Lagrangian acceleration in the x direction is negative near the head of the wave and positive in the lower part. Using the horizontal momentum balance, this finding can be explained by capillary effects on the fluid pressure. In particular, capillarity contributes to excess pressure at the leading edge of the wave and a pressure deficit at the wave toe. Such pressure anomalies can sometimes be achieved in the presence of strong shear (cf. Ref. 2), but in the present case, capillarity appears to be the dominant effect.

The shape of the free surface of the collapsing breaker can be reasonably well approximated with a Boussinesq model. The BOSZ model used in this study was able to predict the main features of the free surface profile. On the other hand, the omission of capillary effects and the reliance of a quadratic velocity profile limit the applicability of the Boussinesq model to simulate the internal flow structure of the collapsing breaker at a laboratory scale.

From an operational point of view, capillarity has not been shown to be a major factor in coastal dynamics or the development of beach morphology, but it may be important in small-scale wave breaking, for example, in small parasitic breakers riding on the top of larger waves (see Ref. 40 and the references contained therein) or in smaller breakers occurring in the uprush on the beach.

The wave breaking in the experiment reported in here has been shown to occur at values of the breaking onset parameter B as defined in Ref. 7 which are close to the values indicated in Refs. 7 and 17. As the breaking criterion defined in these papers has been tested in deep and intermediate depths, it will be interesting to conduct further work exploring the relation between the breaking onset parameter B and the details of the wave breaking process in a larger number of cases in shallow water, and, in particular, in flows dominated by capillarity.

It should be noted that capillarity also comes to the fore in breaking waves at small scales in various other settings. For example, wave breaking in a two-phase flow in circular pipes has been studied recently in Ref. 53. Another interesting further problem will be to understand the generation of vorticity in the wave breaking process and the ensuing eddy motion.

ACKNOWLEDGMENTS

This research was supported in part by the Research Council of Norway and the European Union's Horizon 2020 research and innovation programme. P.G. was supported in part by the National Science Foundation, USA (Grant No. DMS-1615480). V.R. acknowledges financial support from the Isite program Energy and Environment Solutions (E2S), the Communauté d'Agglomération Pays Basque (CAPB), and the Communauté Région Nouvelle Aquitaine (CRNA) for the chair position HPC-Waves. J.-M.Y. was supported in part by the Ministry of Science and Technology, Taiwan (Grant Nos. MOST 106-2115-M-126-003 and MOST 107-2115-M-126-004). W.-Y.W., C.L., and M.-J.K. were supported in part by the Ministry of Science and Technology, Taiwan (Nos. 105-2221-E-005-033-MY3 and 106-2221-E-005-045-MY3).

REFERENCES

- R. J. Adrian and J. Westerweel, *Particle Image Velocimetry* (Cambridge University Press, New York, 2011).
- A. Ali and H. Kalisch, "Reconstruction of the pressure in long-wave models with constant vorticity," *Eur. J. Mech., B: Fluids* **37**, 187–194 (2013).
- A. Babanin, *Breaking and Dissipation of Ocean Surface Waves* (Cambridge University Press, 2011).
- P. Bacigaluppi, M. Ricchiuto, and P. Bonneton, "Upwind stabilized finite element modelling of non-hydrostatic wave breaking and run-up," hal-00990002, 2014.
- P. Bacigaluppi, M. Ricchiuto, and P. Bonneton, "Implementation and evaluation of breaking detection criteria for a hybrid Boussinesq model," *Water Waves* (to be published); e-print arXiv:1902.03021 (2019).
- M. L. Banner and D. H. Peregrine, "Wave breaking in deep water," *Annu. Rev. Fluid Mech.* **25**, 373–397 (1993).
- X. Barthelemy, M. L. Banner, W. L. Peirson, F. Fedele, M. Allis, and F. Dias, "On a unified breaking onset threshold for gravity waves in deep and intermediate depth water," *J. Fluid Mech.* **841**, 463–488 (2018).
- A. Berchet, B. Simon, A. Beaudoin, P. Lubin, G. Rousseaux, and S. Huberson, "Flow fields and particle trajectories beneath a tidal bore: A numerical study," *Int. J. Sediment. Res.* **33**, 351–370 (2018).
- M. Bjørkavåg and H. Kalisch, "Wave breaking in Boussinesq models for undular bores," *Phys. Lett. A* **375**, 1570–1578 (2011).
- M. Bjørnstad and H. Kalisch, "Shallow water dynamics on linear shear flows and plane beaches," *Phys. Fluids* **29**, 073602 (2017).
- H. Borluk and H. Kalisch, "Particle dynamics in the KdV approximation," *Wave Motion* **49**, 691–709 (2012).
- M. K. Brun and H. Kalisch, "Convective wave breaking in the KdV equation," *Anal. Math. Phys.* **8**, 57–75 (2018).
- G. F. Carrier and H. P. Greenspan, "Water waves of finite amplitude on a sloping beach," *J. Fluid Mech.* **4**, 97–109 (1958).
- W. Craig, P. Guyenne, J. Hammack, D. Henderson, and C. Sulem, "Solitary water wave interactions," *Phys. Fluids* **18**, 057106 (2006).
- C. W. Curtis and H. Kalisch, "Vortex dynamics in nonlinear free surface flows," *Phys. Fluids* **29**, 032101 (2017).
- C. G. David, V. Roerber, N. Goseberg, and T. Schlurmann, "Generation and propagation of ship-borne waves—Solutions from a Boussinesq-type model," *Coastal Eng.* **127**, 170–187 (2017).
- M. Derakhti, M. L. Banner, and J. T. Kirby, "Predicting the breaking strength of gravity water waves in deep and intermediate depth," *J. Fluid Mech.* **848**, R2 (2018).
- J. H. Duncan, "Spilling breakers," *Annu. Rev. Fluid Mech.* **33**, 519–547 (2001).
- J. H. Duncan, V. Philomin, M. Behres, and J. Kimmel, "The formation of spilling breaking water waves," *Phys. Fluids* **6**, 2558–2560 (1994).
- N. Ebuchi, H. Kawamura, and Y. Toba, "Fine structure of laboratory wind-wave surfaces studied using an optical method," *Boundary-Layer Meteorol.* **39**, 133–151 (1987).
- H. Favre, *Ondes de Translation* (Dunod, Paris, 1935).
- C. J. Galvin, "Breaker type classification on three laboratory beaches," *J. Geophys. Res.* **73**, 3651–3659, <https://doi.org/10.1029/jb073i012p03651> (1968).
- D. G. Goring, "Tsunami: The propagation of long waves onto a shelf," Technical Report No. KH-R-38, W. M. Keck Laboratory of Hydraulics and Water Resources, California Institute of Technology, Pasadena, California, USA, 1978.
- S. T. Grilli, P. Guyenne, and F. Dias, "A fully non-linear model for three-dimensional overturning waves over an arbitrary bottom," *Int. J. Numer. Methods Fluids* **35**, 829–867 (2001).
- S. T. Grilli, L. A. Svendsen, and R. Subramanya, "Breaking criterion and characteristics for solitary waves on slopes," *J. Waterw., Port, Coastal Ocean Eng.* **123**, 102–112 (1997).
- P. Guyenne and S. Grilli, "Numerical study of three-dimensional overturning waves in shallow water," *J. Fluid Mech.* **547**, 361–388 (2006).
- S. Hatland and H. Kalisch, "Wave breaking in undular bores generated by a moving bottom," *Phys. Fluids* **31**, 033601 (2019).
- A. Jensen, G. K. Pedersen, and D. J. Wood, "An experimental study of wave run-up at a steep beach," *J. Fluid Mech.* **486**, 161–188 (2003).
- H. Kalisch, M. Ricchiuto, P. Bonneton, M. Colin, and P. Lubin, "Introduction to the special issue on breaking waves," *Eur. J. Mech., B: Fluids* **73**, 1–5 (2019).
- A. Khaït and L. Shemer, "On the kinematic criterion for the inception of breaking in surface gravity waves: Fully nonlinear numerical simulations and experimental verification," *Phys. Fluids* **30**, 057103 (2018).
- K. T. Kiger and J. H. Duncan, "Air entrainment mechanisms in plunging jets and breaking waves," *Annu. Rev. Fluid Mech.* **44**, 563–596 (2012).
- N. Li, Y. Yamazaki, V. Roerber, K. F. Cheung, and G. Chock, "Probabilistic mapping of storm-induced coastal inundation for climate change adaptation," *Coastal Eng.* **133**, 126–141 (2018).
- C. Lin, P. H. Yeh, S. C. Hseih, Y. N. Shih, L. F. Lo, and C. P. Tsai, "Prebreaking internal velocity field induced by a solitary wave propagating over a 1:10 slope," *Oceanic Eng.* **80**, 1–12 (2014).
- C. Lin, P. H. Yeh, M.-J. Kao, M. H. Yu, S. C. Hseih, S. C. Chang, T. R. Wu, and C. P. Tsai, "Velocity fields in near-bottom and boundary layer flows in pre-breaking zone of solitary wave propagating over a 1:10 slope," *J. Waterw., Port, Coastal, Ocean Eng.* **141**, 04014038 (2015).
- C. Lin, M.-J. Kao, G. W. Tzeng, W.-Y. Wong, J. Yang, R. V. Raikar, T. R. Wu, and P. L. F. Liu, "Study on flow fields of boundary-layer separation and hydraulic jump during rundown motion of shoaling solitary wave," *J. Earthquake Tsunami* **9**, 1540002 (2015).
- C. Lin, S. M. Yu, W.-Y. Wong, G. W. Tzeng, J.-W. Kao, P. H. Yeh, R. V. Raikar, J. Yang, and C. P. Tsai, "Velocity characteristics in boundary layer flow caused by solitary wave traveling over horizontal bottom," *Exp. Therm. Fluid Sci.* **76**, 238–252 (2016).
- M. S. Longuet-Higgins, "Capillary jumps on deep water," *J. Phys. Oceanogr.* **26**, 1957–1965 (1996).
- P. Lubin and H. Chanson, "Are breaking waves, bores, surges and jumps the same flow?," *Environ. Fluid Mech.* **17**, 47–77 (2017).
- W. K. Melville, "The role of surface-wave breaking in air-sea interaction," *Annu. Rev. Fluid Mech.* **28**, 279–321 (1996).
- S. Murashige and W. Choi, "A numerical study on parasitic capillary waves using unsteady conformal mapping," *J. Comput. Phys.* **328**, 234–257 (2017).
- O. Nwogu, "Alternative form of Boussinesq equations for nearshore wave propagation," *J. Waterw., Port, Coastal Ocean Eng.* **119**, 618–638 (1993).
- D. H. Peregrine, "Breaking waves on beaches," *Annu. Rev. Fluid Mech.* **15**, 149–178 (1983).

- ⁴³M. Perlin, W. Choi, and Z. Tian, "Breaking waves in deep an intermediate waters," *Annu. Rev. Fluid Mech.* **45**, 115–145 (2013).
- ⁴⁴Y. Pomeau, M. Le Berre, P. Guyenne, and S. Grilli, "Wave-breaking and generic singularities of nonlinear hyperbolic equations," *Nonlinearity* **21**, T61–T79 (2008).
- ⁴⁵F. Raichlen, *Waves* (MIT Press, Cambridge, MA, 2012).
- ⁴⁶V. Roeber and J. D. Bricker, "Destructive tsunami-like wave generated by surf beat over a coral reef during Typhoon Haiyan," *Nat. Commun.* **6**, 7854 (2015).
- ⁴⁷V. Roeber and K. F. Cheung, "Boussinesq-type model for energetic breaking waves in fringing reef environments," *Coastal Eng.* **70**, 1–20 (2012).
- ⁴⁸V. Roeber, K. F. Cheung, and M. H. Kobayashi, "Shock-capturing Boussinesq-type model for nearshore wave processes," *Coastal Eng.* **57**, 407 (2010).
- ⁴⁹Y.-M. Scolan and P.-M. Guilcher, "Wave kinematics in a two-dimensional plunging breaker," *Water Waves* (published online).
- ⁵⁰C. E. Synolakis, "The runup of solitary waves," *J. Fluid Mech.* **185**, 523–545 (1987).
- ⁵¹M. Tanaka, "The stability of solitary waves," *Phys. Fluids* **29**, 650–655 (1986).
- ⁵²C. P. Tsai, H. B. Chen, H. H. Hwung, and M. J. Huang, "Examination of empirical formulas for wave shoaling and breaking on steep slopes," *Oceanic Eng.* **32**, 469–483 (2005).
- ⁵³P. Vollestad, A. A. Ayati, and A. Jensen, "Microscale wave breaking in stratified air-water pipe flow," *Phys. Fluids* **31**, 032101 (2019).
- ⁵⁴G. Wei, J. T. Kirby, S. T. Grilli, and R. Subramanya, "A fully nonlinear Boussinesq model for surface waves. Part 1. Highly nonlinear unsteady waves," *J. Fluid Mech.* **294**, 71–92 (1995).
- ⁵⁵D. L. Wilkinson and M. L. Banner, "Undular bores," in 6th Australian Hydraulics and Fluid Mechanics Conference, Adelaide, Australia.

Paper E

Wave Breaking in Undular Bores with Shear Flows

M. BJØRNESTAD, H. KALISCH, M. ABID, C. KHARIF AND M. BRUN
Water Waves (2021), 1–18.



Wave Breaking in Undular Bores with Shear Flows

Maria Bjørnestad¹ · Henrik Kalisch¹ · Malek Abid² · Christian Kharif² · Mats Brun³

Received: 27 April 2020 / Accepted: 16 November 2020
© The Author(s) 2021

Abstract

It is well known that weak hydraulic jumps and bores develop a growing number of surface oscillations behind the bore front. Defining the bore strength as the ratio of the head of the undular bore to the undisturbed depth, it was found in the classic work of Favre (Ondes de Translation. Dunod, Paris, 1935) that the regime of laminar flow is demarcated from the regime of partially turbulent flows by a sharply defined value 0.281. This critical bore strength is characterized by the eventual breaking of the leading wave of the bore front. Compared to the flow depth in the wave flume, the waves developing behind the bore front are long and of small amplitude, and it can be shown that the situation can be described approximately using the well known Kortweg–de Vries equation. In the present contribution, it is shown that if a shear flow is incorporated into the KdV equation, and a kinematic breaking criterion is used to test whether the waves are spilling, then the critical bore strength can be found theoretically within an error of less than ten percent.

Keywords Undular bore · Wave breaking · Shear flow · KdV equation

1 Introduction

A river bore is an upriver-propagating transition between different flow depths which is generally caused by tidal forces. Similar flows can also be realized in controlled environments such as wave flumes, and a number of studies have been conducted to understand the main features of bores. In particular, in Favre's work [21] a dedicated series of laboratory experiments and matching theory based on the shallow-water

Henrik Kalisch
henrik.kalisch@math.uib.no

¹ Department of Mathematics, University of Bergen, 5020 Bergen, Norway

² Aix Marseille Université, CNRS, Centrale Marseille, IRPHE UMR 7342, 13384 Marseille, France

³ CEES, Department of Biosciences, University of Oslo, 0316 Oslo, Norway

Saint-Venant equations is described. Favre's experimental results have been examined theoretically from a number of angles. For example, the initial formation of the free-surface oscillations was explained from a physical perspective in [37,43], the interaction of bores was considered in [9], and the breaking of the leading oscillations in the bore was considered in [10,14,22,30]. Recent laboratory experiments revealing intricate properties of undular bores are detailed in [34,35], and a numerical study of the flow structure is given in [8].

Of particular interest in the present article is the critical bore strength dividing the regime of laminar flow from the regime of partially turbulent flow. To explain the situation, assume without loss of generality that the downstream flow depth is the undisturbed depth in the wave flume, say h_0 , and the incident depth is $a_0 + h_0$. Defining the bore strength by the ratio a_0/h_0 , it was found in [21] that there are three main bore types. If the bore strength is below 0.281, the flow is laminar, and since in this case, none of the waves are breaking, this case is termed the purely undular bore. If the ratio $\alpha = a_0/h_0$ exceeds 0.281, then the leading wave behind the transition front starts to break, and while the flow still features oscillations, there is some turbulence associated with the breaking waves. If the ratio exceeds 0.75, a fully turbulent bore appears.

The main purpose of the current paper is to demonstrate that the critical ratio found by Favre [21] can also be predicted using fairly simple nonlinear model equations such as the KdV equation in connection with a kinematic (or sometimes called convective) breaking criterion which defines the onset of breaking as the point when the horizontal component of the particle velocity exceeds the crest velocity. In effect, if we let the fluid particle velocity at the leading wavecrest of the bore be $U = U(x, \eta(x, t), t)$, and the local phase velocity of the wavecrest be C , then the wave starts spilling when $U/C > 1$. The kinematic wave breaking criterion is one of the simplest diagnostics for predicting the onset of wave breaking (see [28,49] and the references therein), and has been shown to work well in a number of situations [25,27,29].

To study an undular bore in the context of the KdV equation, one needs to be able to pose a boundary-value problem where the incident-free surface level is imposed at, say, the left end of the domain, and the undisturbed level is imposed at the right end of the domain.¹ (see Fig. 1, left panel). Such a model has been developed for instance in [14,42]. One can then evaluate the free surface numerically, and reconstruct the velocity field in the fluid column using the traditional asymptotic expansion of the velocity potential as an asymptotic Taylor series in powers of the vertical coordinate [51]. If the wave crest velocity is also evaluated numerically, then the convective criterion can be tested as an indication of whether the wave starts breaking or not.

Previous studies using this wave-breaking criterion in connection with a Boussinesq system and the KdV equation gave good qualitative results, but were not quantitatively convincing. In particular, the critical ratio was found to be $a_0/h_0 \sim 0.379$ in [10] using a Boussinesq system, and $a_0/h_0 \sim 0.353$ in the context of the KdV equation [14].

A possible improvement on these results may be obtained from the inclusion of vorticity into the description. Indeed, it is by now well known that vorticity can have a

¹ While a river bore is generally propagating upstream, in the current work we use the convention that upstream describes the end of the wave flume where the inflow is imposed, and that the bore is propagating downstream.

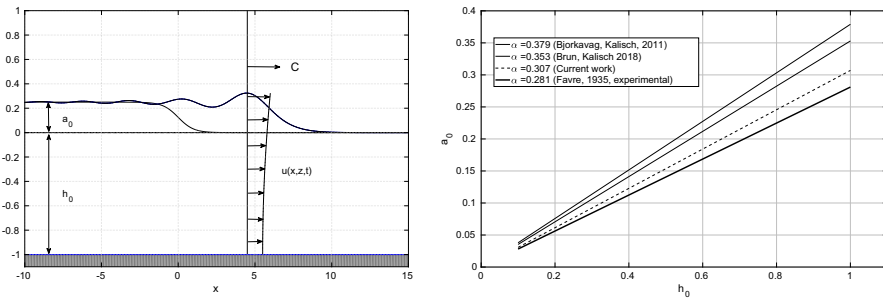


Fig. 1 Left panel: definition sketch for undular bore. The bore front propagates at velocity C . The arrows indicate the vertical distribution of the horizontal velocity $u(x, z, t)$ below the maximum surface displacement. Right panel: the critical amplitude a_0 dividing the purely undular case from the case where the leading wave features wave breaking graphed against the undisturbed depth h_0 . The slope of the curves is the non-dimensional critical bore strength. The value $\alpha = 0.281$ was found in Favre's experimental work [21]. The value $\alpha = 0.379$ was found in a previous work [10], the value $\alpha = 0.353$ was found in [14], and the value $\alpha = 0.307$ is found in the present work

significant effect on the properties of surface waves (see for example [1,30,38,41,48] and references therein). One simple configuration is the case of a linear shear flow such as used in [48]. In particular in the case of long waves, this configuration is expected to capture many features of more general flows (see [17]), and it is our aim in the present work to determine whether the agreement with the experimental results of Favre may be improved by incorporating a constant shear flow into the governing equation. Indeed, the existence of vorticity in a similar situation was found in [26], and a mathematical inquiry into Favre's results also suggested that vorticity might be present in such flows [30]. To get an idea of the strength of vorticity in Favre's experiments, we derive a KdV equation in the presence of a linear shear flow. We then run a numerical simulation of an undular bore and try to match the wavelength of the oscillations of the numerical approximation of the KdV equation with the experimental wavelengths reported by Favre. This procedure leads to an estimate for the vorticity Γ which is then used in simulations aimed at finding the critical bore ratio by testing the leading wave for incipient breaking. The approach outlined above yields a critical bore strength $a_0/h_0 \sim 0.307$ which is within 9% of the experimental ratio of 0.281.

The plan of the paper is as follows. In the next section, the experiments of Favre are explained in some detail. Then in Sect. 3, the KdV equation with a shear flow is explained. Section 4 contains some comments about the numerical approach, and Sect. 5 describes the results of our numerical simulations. Finally, Sect. 6 contains a brief discussion which puts our findings into context with respect to some recent studies on breaking waves.

2 The Experiments of Favre

Favre (1935) conducted a series of experiments on undular bores in an open wave tank at the Hydraulic Laboratory of Ecole Polytechnique Fédérale of Zurich. The wave channel of rectangular cross section was 75.58 m long, 0.42 m wide and 0.40 m deep.

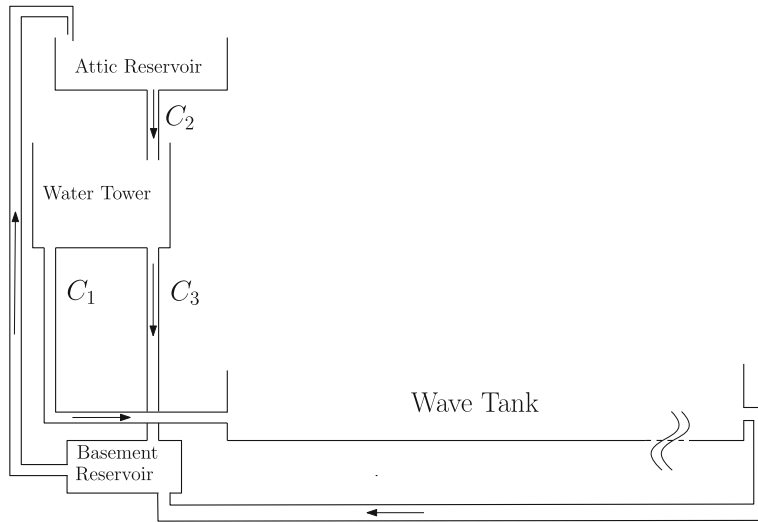


Fig. 2 Definition sketch for the experimental setup of Favre

Some experiments were performed with a horizontal tank and some were performed with a slightly inclined tank. Herein, we consider only experiments in the horizontal wave tank. The tank was supplied by a water tower of constant water level through a pipe C_1 . The water tower was supplied by fixed reservoirs located in the laboratory attic through a pipe C_2 . A third pipe C_3 was used to drain off the excess of water of the tower. The water level of the tower remained constant as long as the flow from C_2 was larger than that of C_1 . The excess water was drained off via C_3 to a reservoir located in the laboratory basement, and then returned by pumps to the reservoirs located in the attic. The water flow from C_1 was adjusted by a valve operated by a servo-motor. The pipe C_2 included a device that allowed the determination of the flow from the water tower. At the end of the tank was a sluice gate that allowed control of the water discharge and full closing of the end of the tank. Beyond the sluice gate, the water was discharged in the same reservoir in the basement as mentioned above. With this setup, it was possible to tune the system so as to guarantee a constant inflow into the wave tank and adjust the inflow to create bores of varying strength. A schematic of the setup just described is shown in Fig. 2.

Three measuring and recording devices were used: (1) six vertical scales located in the longitudinal axial plan of the tank and distributed along the tank every 12 m were used for measuring the water level at rest or in motion. The accuracy was on the order of one to two tenths of a millimeter. (2) To record the fluctuations of the free surface at the six locations Favre used pressure head (Pitot) tubes whose meniscus positions were recorded on sensitive paper exposed to light. An optical apparatus consisting of a prism, a lens, an electric lamp and a mirror was used to record the meniscus position. (3) The variations of the front of the undular bores were measured differently. The measurements were based on photos taken with exposure time of approximately 1/100 s.

Preliminary experiments were conducted to calibrate the devices. Undular bores were generated by a sudden variation of the flow at the upstream end of the tank. Favre performed a series of 30 experiments on undular bores on still water, grouped in three series corresponding to three different initial constant water depths (0.205 m, 0.155 m and 0.1075 m). A spillway plate was placed at the downstream end of the tank whose height was fixed to the desired depth, then the tank was filled through C1 until the water overflowed the spillway plate. Water filling was stopped and 20 min later the water level was stabilized at the height of the spillway plate.

The water flow was determined as a function of the valve displacement (see Figure 38 of Favre [21]). The water flowing into the tank generated an undular bore with a front consisting of a series of undulations whose number increased with the distance of propagation. To make the free surface easily visible, Favre sprinkled aluminum sawdust on the free surface and scattered confetti soaked with black ink. These measures made the free surface clearly visible on photographs. Favre photographed 21 fronts of undular bores: (1) 6 of the first series of experiments (nos. 2, 4, 6, 8, 10, 12; depth 0.205 m); (2) 6 of the third series of experiments (nos. 21, 22, 23, 24, 26, 29; depth 0.1075 m); (3) 8 of the sixth series and one of the seventh series of experiments, which correspond to inclined tank. In the present work, we consider two cases of the third series of experiments, and the results of numerical simulations of experiments no. 22 and no. 23 are presented in Sect. 5.

The fronts of the undular bores were photographed when the crest of the first undulation was located at 64.78 m and 64.60 m from the upstream end of the tank for experiments no. 22 and no. 23, respectively. Recall that Favre introduced the bore strength parameter a_0/h_0 , where a_0 was the mean height of the head of the undular bore (see Figure 41 of Favre [21]) and h_0 was the initial water depth where the first crest of the undular bore was photographed. Bore strength values corresponding to experiments no. 22 and no. 23 are given in Sect. 5. Favre found that for weak values of bore strength the bore undulations were almost sinusoidal, whereas for high values they became cnoidal (experiments nos. 22, 23, 24).

In experiments no. 22 and no. 23, no wave breaking was observed. In experiment no. 24, the leading wave exhibited spilling breaking after traveling a considerable distance. Experiments no. 26 and no. 29 featured wave breaking after the front of the bore had traveled a shorter distance. Breaking and non-breaking cases can be clearly identified by observing the maximum height of the leading wave. Experimental results based on Favre's data shown in Figure 49 of [21] are plotted in Fig. 3. It is apparent that the maximum height of the leading wave increases with increasing bore strength, up to a maximum of 2.06 times the incident depth a_0 . That maximum occurs in experiment no. 24 which corresponds to $a_0/h_0 = 0.281$. As shown in these figures, experiments with higher bore strength feature earlier breaking and much lower wave heights for the leading wave.

As already stated above, the main purpose of the present work is to explore whether the critical bore strength can be found using fairly simple wave models such as the KdV equation. In the next section, the KdV equation will be derived in the presence of a shear flow, and then numerical simulations will be presented which suggest that the critical ratio can be found to within 9% error.

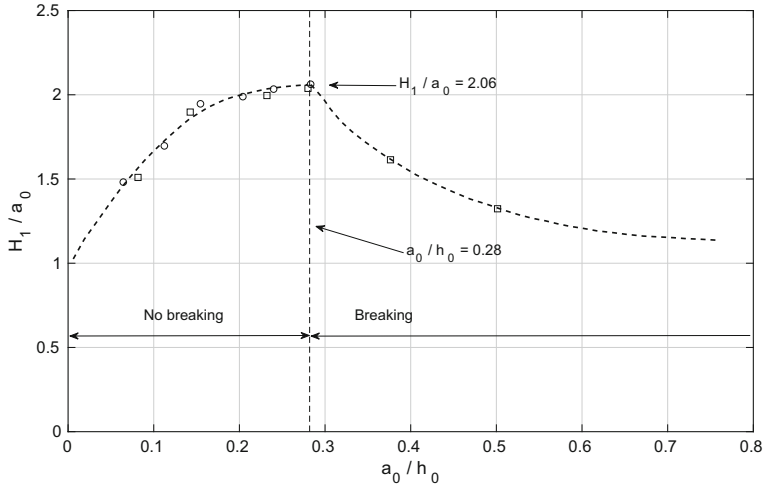


Fig. 3 Wave height H_1 of the leading wave—normalized by a_0 —as a function of the bore strength a_0/h_0 . The experimental data are taken from Figure 49 in [21]. Legend: o - undisturbed depth $h_0 = 0.205$ m, □ - undisturbed depth $h_0 = 0.1075$ m

3 The KdV Equation in the Presence of Shear Flows

Consider a fluid contained in a long channel of unit width and depth h_0 . The surface water-wave problem is generally described by the Euler equations with slip conditions at the bottom, and kinematic and dynamic boundary conditions at the free surface. We fix a coordinate system by aligning the x -axis with the undisturbed free surface, and suppose the fluid domain extends along the entire x -axis. It is assumed that the fluid is inviscid, incompressible and of unit density, the bottom of the channel is flat, and the wave motion transverse to the x -axis can be neglected.

With the assumption of irrotational flow and using the incompressibility of the fluid, the two-dimensional Euler equations can be written in terms of the Laplace equation for a velocity potential ϕ , and the boundary conditions at the free surface are given in terms of ϕ and the surface excursion $\eta(x, t)$ by

$$\begin{aligned} \eta_t + \phi_x \eta_x - \phi_z &= 0, & \text{on } z = \eta(x, t), \\ \phi_t + \frac{1}{2}(\phi_x^2 + \phi_z^2) + g\eta &= 0, & \text{on } z = \eta(x, t), \end{aligned}$$

where g is the gravitational acceleration.

As is well known, this problem is difficult to treat both mathematically and numerically, and in practical situations, an asymptotic approximation of the Euler equations is often used. In the case at hand, we have long waves of small to moderate amplitude on a shallow fluid, and it appears that these waves fall approximately into the Boussinesq scaling regime. Moreover, the waves travel only in one direction down the length of the wave flume, so that an appropriate asymptotic model to be used is the

KdV equation, given in dimensional form by

$$\eta_t + c_0 \eta_x + \frac{3}{2} \frac{c_0}{h_0} \eta \eta_x + \frac{1}{6} c_0 h_0^2 \eta_{xxx} = 0.$$

Here, $c_0 = \sqrt{gh_0}$ is the limiting long-wave speed, whereas already mentioned, where g is the gravitational acceleration and h_0 is the undisturbed depth.

The KdV equation features both nonlinearity and dispersion, and the balance of these two effects gives rise to both solitary-wave solutions and periodic traveling waves [31]. The equation is known to give a good description of the evolution of unidirectional surface water waves in the case when the waves are long compared to the undisturbed depth h_0 of the fluid, the average amplitude of the waves is small when compared to h_0 and transverse effects are negligible [12,16,32]. In the derivation of the KdV equation, the potential is written asymptotically as

$$\phi = f - \frac{z^2}{2} f_{xx}, \quad (1)$$

where $f(x, t)$ represents an approximation to the velocity potential evaluated at the bottom. In addition, the assumption of wave propagation in the direction of increasing x values (to the right) leads to the relation

$$f_x = \frac{g}{c_0} \left\{ \eta - \frac{1}{4h_0} \eta^2 + \frac{h_0^2}{3} \eta_{xx} \right\}. \quad (2)$$

Using (1) and (2) shows that the horizontal velocity can be expressed to second order as

$$u(x, z, t) = \phi_x(x, z, t) = \frac{g}{c_0} \left\{ \eta - \frac{1}{4h_0} \eta^2 + h_0^2 \left(\frac{1}{3} - \frac{z^2}{2} \right) \eta_{xx} \right\}.$$

That means if a solution η of the KdV equation is given either in closed form or numerically, the horizontal particle velocity can always be found at any point in the fluid column. For more details, the reader may consult [2,51]. In the case at hand, the velocity is evaluated at the free surface so that the breaking criterion can be tested. Using this approach, the authors of [14] found that the critical bore strength was $\alpha = 0.353$, improving earlier work where a Boussinesq model was used [10]. In the present work, we will incorporate a background shear flow to further improve the comparison.

In the presence of background vorticity, the horizontal velocity field may be defined as $U(x, z, t) = u(x, z, t) - (z + h_0)\Gamma$ (see Fig. 4). Model equations of KdV and Boussinesq type for surface waves in the presence of background shear can be derived in a similar fashion as in the irrotational case. The reader may consult for example [15,40,46,54]. Except for a minor modification, the equation to be used in the present study was derived in [40]. For background shear such as shown in Fig. 4, the appropriate

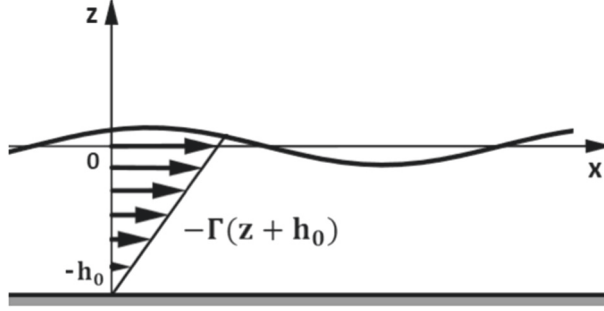


Fig. 4 Uniform shear flow with horizontal velocity $U = u - (z + h_0)\Gamma = \frac{\partial \phi}{\partial x} - (z + h_0)\Gamma$. In the figure, Γ is negative

KdV equation is

$$\eta_t + C_0^+ \sqrt{gh_0} \eta_x + \frac{C_0^+ (3 + \tilde{\Gamma}^2)}{1 + (C_0^+)^2} \frac{\sqrt{gh_0}}{h_0} \eta \eta_x + \frac{C_0^+ + \tilde{\Gamma}}{3(1 + (C_0^+)^2)} h_0^2 \sqrt{gh_0} \eta_{xxx} = 0.$$

This equation is given in dimensional form, with the non-dimensional parameter $C_0^+ = \frac{-\tilde{\Gamma}}{2} + \sqrt{\frac{\tilde{\Gamma}^2}{4} + 1}$ quantifying the strength of the background shear, and $\tilde{\Gamma}$ being the non-dimensional vorticity scaled with $\tilde{\Gamma} = \frac{\Gamma}{\sqrt{\frac{g}{h_0}}}$. The horizontal perturbation velocity field can be found in a similar way as for the irrotational case, and is given by

$$u = \frac{\sqrt{gh_0}}{h_0} \left\{ -C_0^- \eta + \frac{C_0^- + \tilde{\Gamma}}{2(1 + (C_0^+)^2)} \frac{\eta^2}{h_0} + \frac{C_0^+ + \tilde{\Gamma}}{3(1 + (C_0^+)^2)} h_0^2 \eta_{xx} - \frac{C_0^-}{6} h_0^2 \eta_{xx} + \frac{C_0^-}{2} h_0^2 \left(1 + \frac{z}{h_0}\right)^2 \eta_{xx} \right\},$$

where we have used $C_0^- = \frac{-\tilde{\Gamma}}{2} - \sqrt{\frac{\tilde{\Gamma}^2}{4} + 1}$.

4 Non-Dimensionalization and Numerical Discretization

To prepare for the numerical discretization, it is convenient to scale the variables appearing in the equation above as follows: $x \rightarrow \frac{x}{h_0}$, $z \rightarrow \frac{z}{h_0}$, $t \rightarrow \frac{t}{\sqrt{\frac{h_0}{g}}}$, $\eta \rightarrow \frac{\eta}{h_0}$, $u \rightarrow \frac{u}{\sqrt{gh_0}}$, $\Gamma \rightarrow \frac{\Gamma}{\sqrt{\frac{g}{h_0}}}$. Using this scaling, the non-dimensional KdV equation can be expressed as

$$\eta_t + C_0^+ \eta_x + \frac{C_0^+ (3 + \Gamma^2)}{1 + (C_0^+)^2} \eta \eta_x + \frac{C_0^+ + \Gamma}{3(1 + (C_0^+)^2)} \eta_{xxx} = 0. \quad (3)$$

The coefficients C_0^+ and C_0^- are defined in the same way as in the last section. In the scaled variables, the horizontal velocity field appears as

$$U(x, z, t) = -C_0^- \eta + \frac{C_0^- + \Gamma}{2(1+(C_0^+)^2)} \eta^2 + \frac{C_0^+ + \Gamma}{3(1+(C_0^+)^2)} \eta_{xx} \\ - \frac{C_0^-}{6} \eta_{xx} + \frac{C_0^-}{2} (1+z)^2 \eta_{xx} - (z+1)\Gamma.$$

It is well known that the KdV equation features exact solitary-wave solutions. If the coefficients of the KdV equation are defined such as in (3), the solitary wave has the form

$$\eta = \eta_0 \operatorname{sech}^2 \left(\sqrt{\frac{C_0^+(3+\Gamma^2)\eta_0}{4(C_0^+ + \Gamma)}} (x - x_0 - ct) \right), \quad (4)$$

with the phase speed c given in terms of the amplitude η_0 by $c = C_0^+ + \frac{C_0^+(3+\Gamma^2)\eta_0}{3(1+(C_0^+)^2)}$. This exact solution will be used later to validate the implementation of the numerical algorithm.

The numerical approximation of the solutions $\eta(x, t)$ and $U(x, \eta(x), t)$ is based on a finite-difference method for the spatial derivatives and a hybrid Adam–Bashforth/Crank–Nicolson time integration scheme, such as previously used in [14,42]. The local phase velocity C of the leading wavecrest is computed approximately by following the crest evolution and using a second-order central difference formula.

To define an appropriate numerical discretization, boundary conditions need to be imposed. In the far field upstream and downstream of the bore, the surface elevation η approaches the stipulated values α and 0, respectively. These boundary conditions are exact up to machine precision as long as the spatial domain is large enough. In addition, a Neumann boundary condition needs to be specified in the far field downstream (see for example [13]). Using a homogeneous Neumann boundary condition and the Dirichlet conditions as indicated above yields the initial-boundary-value problem

$$\eta_t + C_0^+ \eta_x + \frac{C_0^+(3+\Gamma^2)}{1+(C_0^+)^2} \eta \eta_x + \frac{C_0^+ + \Gamma}{3(1+(C_0^+)^2)} \eta_{xxx} = 0, \quad x \in [-l, l], \quad t \geq 0, \\ \eta(x, 0) = \eta_0(x), \\ \eta(-l, t) = \alpha, \\ \eta(l, t) = 0, \\ \eta_x(l, t) = 0.$$

The initial data are given by $\eta_0(x) = \frac{1}{2}a_0[1 - \tanh(kx)]$, where k is a model parameter denoting the steepness of the initial bore slope. In an idealized setting, one may take the limit as k approaches infinity, leading to the so-called dispersive shock problem [20,23]. However in the present case, we take the finite value $k = 1$.

It will be expedient to rewrite the problem to obtain homogeneous boundary conditions, and we define an auxiliary function $\zeta(x, t) \equiv \eta(x, t) - \eta_0(x)$. Using ζ , the problem can be reformulated as an inhomogeneous equation with a forcing given in

terms of ζ and η_0 , but with homogeneous boundary and initial conditions. The equation for ζ can then be written as

$$\zeta_t + C_0^+ \zeta_x + \frac{C_0^+(3+\Gamma^2)}{1+(C_0^+)^2} \left(\frac{1}{2} \zeta^2 + \eta_0 \zeta \right)_x + \frac{C_0^+ + \Gamma}{3(1+(C_0^+)^2)} \zeta_{xxx} = -F, \quad x \in [-l, l], \quad t \geq 0,$$

where

$$F \equiv C_0^+ \eta_0' + \frac{C_0^+(3+\Gamma^2)}{1+(C_0^+)^2} \eta_0 \eta_0' + \frac{C_0^+ + \Gamma}{3(1+(C_0^+)^2)} \eta_0''',$$

and homogeneous boundary and initial conditions are imposed. We discretize the spatial domain $[-l, l]$ using a finite set of points, $\{x_j\}_{j=0}^N \subset [-l, l]$, where $x_0 = -l$ and $x_N = l$, and $\delta x = 2l/N$ is the distance between two neighboring grid points. The time domain is also discretized uniformly by defining $t_n = n\delta t$, where t_0 is equal to zero. With this notation, the approximate function value at time t_n and grid point x_j is defined to be $v_j^n \approx \zeta(x_j, t_n)$.

Regarding the spatial discretization, the first and third derivatives at a point x_j are approximated by the central difference formulas

$$\zeta_x(x_j, t) \approx \frac{v_{j+1} - v_{j-1}}{2\delta x} \quad (5)$$

and

$$\zeta_{xxx}(x_j, t) \approx \frac{v_{j+2} - 2v_{j+1} + 2v_{j-1} - v_{j-2}}{2\delta x^3}. \quad (6)$$

Since we impose the Dirichlet conditions $v_0 = 0$ and $v_N = 0$, the equation can be solved for the grid points $\{x_j\}_{j=1}^{N-1}$, and that leaves us with just two points for which the third derivative approximation is not valid. Given the Neumann condition and the central difference approximation, we have $(v_{N+1} - v_{N-1})/2\delta x = 0$ which implies $v_{N+1} = v_{N-1}$. This enables us to use the third derivative approximation at the grid point x_{N-1} in the form

$$\zeta_{xxx}(x_{N-1}, t) \approx \frac{v_{N+1} - 2v_N + 2v_{N-2} - v_{N-3}}{2\delta x^3} = \frac{v_{N-1} + 2v_{N-2} - v_{N-3}}{2\delta x^3}. \quad (7)$$

As there is no Neumann condition on the left boundary, we employ a forward difference formula to approximate the third derivative at the grid point x_1 as follows:

$$\zeta_{xxx}(x_1, t) \approx \frac{-v_4 + 6v_3 - 12v_2 + 10v_1 - 3v_0}{2\delta x^3}. \quad (8)$$

Table 1 Discretization errors and error ratios for numerical approximations of the time evolution of a solitary wave of the KdV equation (3) with $\Gamma = -0.2$ and $\eta_0 = 0.5$

δt	L^2 -error	Ratio
0.100000	0.003953	
0.050000	0.000975	4.052
0.025000	0.000242	4.031
0.012500	0.000059	4.052
0.006250	0.000019	3.235
0.003125	0.000014	1.318

These computations were run up to final time $T = 1$, and with a spatial grid size of $\delta x = 0.01$

The difference formulas (5), (6), (7) and (8) applied at all grid points give rise to the discrete differentiation matrices D_1 and D_3 as follows:

$$D_1 = \frac{1}{2\delta x} \begin{pmatrix} 0 & 1 & 0 & \dots & 0 \\ -1 & 0 & 1 & 0 & \vdots \\ 0 & -1 & 0 & 1 & 0 \\ \vdots & & & \ddots & \\ 0 & \dots & & & 0 & 1 \\ 0 & \dots & & & -1 & 0 \end{pmatrix}, \quad D_3 = \frac{1}{2\delta x^3} \begin{pmatrix} 10 & -12 & 6 & -1 & 0 & \dots & 0 \\ 2 & 0 & -2 & 1 & 0 & \dots & 0 \\ -1 & 2 & 0 & -2 & 1 & 0 & \\ 0 & -1 & 2 & & \ddots & & \\ \vdots & & & \ddots & & \ddots & 1 \\ 0 & & & & \ddots & 0 & -2 \\ 0 & \dots & & -1 & 2 & 1 & \end{pmatrix}.$$

Applying a Crank–Nicolson method to the linear terms on the right-hand side of the equation, and an Adams–Bashforth method to the nonlinear terms, the difference equation for determining the vector \mathbf{v}^{n+1} is given by

$$\frac{\mathbf{v}^{n+1} - \mathbf{v}^n}{\delta t} = -\frac{C_0^+(3+\Gamma^2)}{2(1+(C_0^+)^2)} D_1 \left[3\left(\frac{1}{2}(\mathbf{v}^n)^2 + \mathbf{v}^n \mathbf{0}\right) - \left(\frac{1}{2}(\mathbf{v}^{n-1})^2 + \mathbf{v}^{n-1} \mathbf{0}\right) \right] - \frac{C_0^+ + \Gamma}{3(1+(C_0^+)^2)} D_3 (\mathbf{v}^{n+1} + \mathbf{v}^n) - \frac{1}{2} C_0^+ D_1 (\mathbf{v}^{n+1} + \mathbf{v}^n) - \mathbf{F},$$

where $\mathbf{v}^n = (v_1^n, v_2^n, \dots, v_{N-1}^n)^T$, $\mathbf{0} = (\eta_0(x_1), \eta_0(x_2), \dots, \eta_0(x_{N-1}))^T$ and $\mathbf{F} = (F(x_1), F(x_2), \dots, F(x_{N-1}))^T$. This $n \times n$ -system of equations can easily be solved for \mathbf{v}^{n+1} , and then to advance the numerical approximation by one time step, only three multiplications by sparse matrices are required.

The implementation is verified by using the well-known exact solitary-wave solution of the KdV equation which is given in the form (4). In Tables 1 and 2, the equation is solved in the case $\Gamma = -0.2$ and with the amplitude $\eta_0 = 0.5$ on the time interval $t \in [0, 1]$. It can be clearly seen that the second-order convergence is achieved in the spatial and the time discretization.

Table 2 Discretization errors and error ratios for numerical approximations of the time evolution of a solitary wave of the KdV equation (3) with $\Gamma = -0.2$ and $\eta_0 = 0.5$

δx	L^2 -error	Ratio
0.800000	0.0971178	
0.400000	0.0234826	4.136
0.020000	0.0057898	4.056
0.010000	0.0014419	4.015
0.005000	0.0003601	4.005
0.002500	0.0000899	4.004
0.001250	0.0000224	4.012
0.000625	0.0000055	4.042

These computations were run up to final time $T = 1$, and with a time step of $\delta t = 0.001$

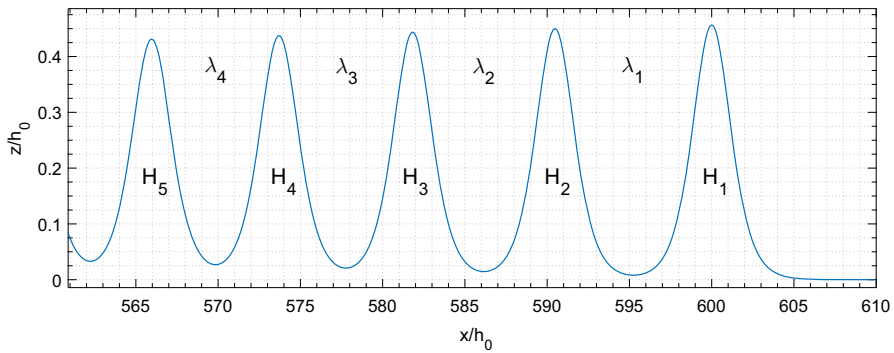


Fig. 5 Numerical approximation of the first five waves behind the borefront. The wave height and the wavelength of the leading wave are denoted by H_1 and λ_1 , respectively. For the second wave, the wave height and wavelength are denoted by H_2 and λ_2 , and so on

5 Simulations

To determine the critical bore ratio, the experiments of Favre are analyzed with regard to the strength of vorticity in the flow. We focus on Favre's experiments no. 22, no. 23 and no. 24 with bore strengths of $\frac{a_0}{h_0} = 0.1395$, $\frac{a_0}{h_0} = 0.2307$ and $\frac{a_0}{h_0} = 0.281$, respectively. A numerical domain $[-610, 610]$ was used, and some experiments were double checked on a larger domain to make sure that there was no detrimental effect of numerical instabilities due to the treatment of the boundary conditions. A comparison of the first five waves is made at a propagation distance of about 600 depths, similar to the analysis in [30]. A plot of the surface elevation is shown in Fig. 5. Tables 3 and 4 show the wave heights and wavelengths of the five waves behind the bore front for several values of the vorticity Γ . The experiments were generally checked by making runs with smaller spatial and temporal grid sizes to make sure that numerical errors did not contribute to the results.

With the numerical measurements of wavelengths and wave heights of the five leading waves in hand, a comparison with the measurements from Favre's experiment can be conducted. For each value of Γ in Tables 3 and 4, an estimate of the relative error

Table 3 Comparison of simulations with Favre's experiment no. 22

Γ	-0.10	-0.15	-0.20	-0.25	-0.30	-0.35	-0.40	Favre no. 22
H_1 (mm)	29.4	29.4	29.4	29.4	29.5	29.5	29.5	28
H_2 (mm)	28.6	28.6	28.6	28.6	28.7	28.7	28.7	27
H_3 (mm)	27.8	27.8	27.8	27.9	27.9	27.7	28.0	28.5
H_4 (mm)	27.0	27.0	27.0	27.1	27.1	27.2	27.2	27
H_5 (mm)	26.3	26.3	26.3	26.3	26.4	26.4	26.5	26
λ_1 (m)	1.24	1.21	1.19	1.15	1.12	1.09	1.06	1.10
λ_2 (m)	1.12	1.09	1.06	1.03	1.00	0.98	0.95	1.04
λ_3 (m)	1.04	1.01	0.99	0.97	0.95	0.91	0.90	0.94
λ_4 (m)	1.00	0.97	0.94	0.91	0.90	0.87	0.84	0.92

The seven columns in the center display the simulated wave heights and wavelengths of the first five waves behind the bore front for seven values of the vorticity Γ . The last column displays the corresponding measurements in Favre's experiment no. 22. Measurements were made at 600 depths

Table 4 Comparison of simulations with Favre's experiment no. 23

Γ	-0.10	-0.15	-0.20	-0.25	-0.30	-0.35	-0.40	Favre no. 23
H_1 (mm)	49.4	49.4	49.5	49.6	49.7	49.8	50.0	49.5
H_2 (mm)	48.7	48.7	48.8	48.9	49.0	49.1	49.2	47
H_3 (mm)	48.0	48.0	48.0	48.1	48.2	48.3	48.5	47
H_4 (mm)	47.2	47.3	47.4	47.5	47.6	47.7	47.8	44.5
H_5 (mm)	46.6	46.6	46.7	46.8	46.9	47.7	47.1	42
λ_1 (m)	1.09	1.06	1.03	1.01	0.98	0.96	0.94	0.94
λ_2 (m)	0.98	0.96	0.92	0.90	0.89	0.87	0.85	0.92
λ_3 (m)	0.92	0.89	0.88	0.86	0.83	0.81	0.78	0.91
λ_4 (m)	0.87	0.85	0.83	0.81	0.80	0.77	0.75	0.84

The seven columns in the center display the simulated wave heights and wavelengths of the first five waves behind the bore front for seven values of the vorticity Γ . The last column displays the corresponding measurements in Favre's experiment no. 23. Measurements were made at 600 depths

is calculated using the least-square method. The relative error for both the wavelength and the wave height are first calculated separately and then added together. In this way, for every value of Γ , the corresponding value of the relative error can be plotted as shown in Fig. 6. With polynomial curve fitting, the best approximate values of Γ for the experiments no. 22 and no. 23 are found to be $\Gamma_{22} = -0.2749$ and $\Gamma_{23} = -0.2316$, respectively. An estimate of Γ in Favre's experiment no. 24 with bore strength $\frac{a_0}{h_0} = 0.281$ was also made to obtain an overall better estimate of Γ in the critical case. In Fig. 7, the strength of vorticity is given in terms of the bore strength from Favre's experiments no. 22, no. 23 and no. 24. Using a straightforward regression analysis, an estimate of the strength of vorticity in Favre's experiment with a bore strength of 0.281 is found to be $\Gamma = -0.2213$.

By implementing this value in the numerical scheme, together with a range of values of a_0 around the critical ratio, and letting the waves travel a distance close to

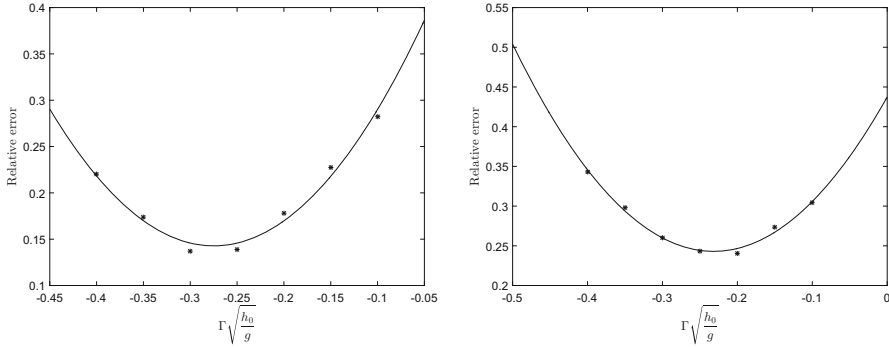


Fig. 6 Relative errors for different strengths of vorticity in Favre's experiments no. 22 (left panel) and no. 23 (right panel)

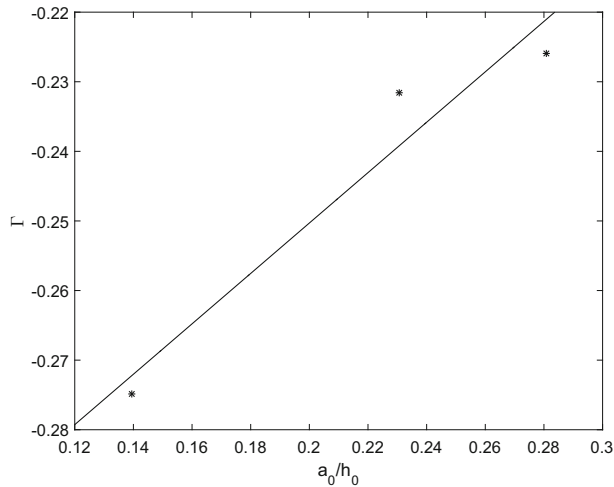


Fig. 7 This figure shows the relation between the bore strength a_0/h_0 and the strength of vorticity Γ . A straight line fit is made using data from experiments no. 22, no. 23 and no. 24

600 depths, we could observe whether the waves will break or not. In Fig. 8, the crest speed C and the horizontal velocity component at the free surface are plotted base on a computation with $\Gamma = -0.2213$ and $a_0 = 0.307$. The ratio between the crest speed and the horizontal particle velocity reaches $U/C \geq 1$ at about 600 depths, and this means that the leading wave is starting to spill which limits the further growth of the wave. Thus, with the inclusion of a background shear flow with constant vorticity the critical ratio is found to be 0.307.

6 Discussion

As mentioned in the introduction, the kinematic wave breaking criterion is one of the most commonly used criteria for the prediction of the onset of wave breaking. The

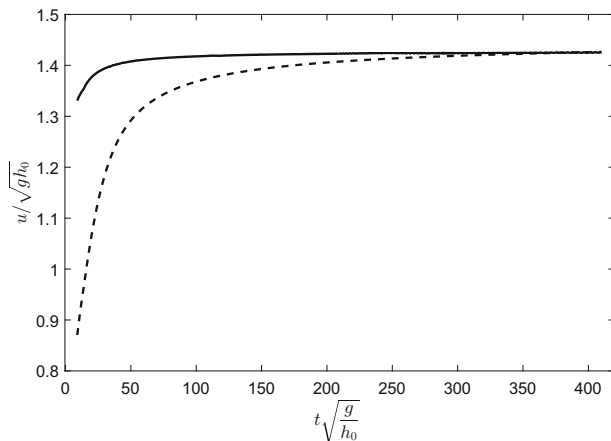


Fig. 8 The solid curve represents the phase speed and the dashed curve represents the horizontal particle velocity. The constant vorticity is $\Gamma = -0.2213$ and the bore strength is 0.307

criterion has been shown to pinpoint the commencement of wave breaking in various situations. In particular, the criterion was shown to perform well in deep water in [29,49], and in shallow water both on flat bathymetry [25] and on a sloping beach [27,50]. In some situations where the kinematic breaking criterion performs poorly, the problem can be ascribed to the difficulty of accurately finding the phase velocity of the waves from measurements [45], and the directionality of the waves in three-dimensional situations [53].

Some authors have attempted to use the kinematic criterion in connection with numerical codes to determine whether to switch from a dispersive Boussinesq-type scheme to a shallow-water scheme with numerical dissipation to capture energy loss in breaking waves. It was suggested in [5] that this approach works best for wave shoaling if the criterion is tightened by introducing a positive constant $\kappa < 1$, and to define breaking onset as the first time that $U/C > \kappa$. However, this approach requires the determination of the constant κ . If an appropriate value for κ can be found, then this breaking criterion can give excellent results [6,11,39].

Sharpening the kinematic criterion if used as a numerical switch makes sense as the numerical dissipation needs time to have an effect on the waves. In fact, tightening the kinematic criterion was already suggested earlier based on experimental evidence [45], and more recently based on studies of wave breaking in large and intermediate depth [7,18]. In these works, a new parameter B based on crest speed and local energy flux and density was put forward as a diagnostic for the initiation of wave breaking. In particular, as shown in [7], using this parameter reduces to a sharpened convective criterion when evaluated at the free surface. In a nutshell, the sharpened criterion based on the parameter B predicts wave breaking when $B \sim 0.87$, though breaking may not commence until B is actually close to 1. As already alluded to, the new criterion based on the parameter B is based on a dynamic or energetic criterion based on evaluation of energy flux and density, such as put forward for example in [44].

To complete this brief review, one may add that geometric breaking criteria are popular in some quarters. Geometric criteria are based on the shape and in particular the steepness of the waves close to breaking, such as reviewed in [4]. Among them the most used is the limiting wave steepness parameter $s \approx ak_{\max}$, which can be transformed into the kinematic limit $u \approx c$. For a detailed review on geometric, kinematic and dynamic criteria for breaking onset one can refer to [3].

To further improve comparison with experiments using the simple kinematic criterion used in the current work, one might use fully nonlinear Boussinesq systems, such as the Serre or Green–Naghdi equations [19,33] or higher-order KdV-type equations, such as the higher-order regularized long wave equation used in [55]. One possible obstacle with this approach is that the boundary-value problem must be shown to be stable to small perturbations.

Acknowledgements This research was supported in part by the Research Council of Norway under grant 239033/F20. The authors wish to thank the organizers of *B'WAVES 2018* in Marseilles, Olivier Kimmoun and Michel Benoit. The authors wish to thank Amutha Senthilkumar for help with the implementation of the numerical discretization.

Compliance with ethical standards

Conflict of interest There is no conflict of interest. Data sharing is not applicable to this article as no datasets were generated or analyzed during the current study.

Open Access This article is licensed under a Creative Commons Attribution 4.0 International License, which permits use, sharing, adaptation, distribution and reproduction in any medium or format, as long as you give appropriate credit to the original author(s) and the source, provide a link to the Creative Commons licence, and indicate if changes were made. The images or other third party material in this article are included in the article's Creative Commons licence, unless indicated otherwise in a credit line to the material. If material is not included in the article's Creative Commons licence and your intended use is not permitted by statutory regulation or exceeds the permitted use, you will need to obtain permission directly from the copyright holder. To view a copy of this licence, visit <http://creativecommons.org/licenses/by/4.0/>.

References

1. Ali, A., Kalisch, H.: Reconstruction of the pressure in long-wave models with constant vorticity. *Eur. J. Mech. B Fluids* **37**, 187–194 (2013)
2. Ali, A., Kalisch, H.: On the formulation of mass, momentum and energy conservation in the KdV equation. *Acta Appl. Math.* **133**, 113–131 (2014)
3. Babanin, A.: *Breaking and Dissipation of Ocean Surface Waves*. Cambridge University Press, Cambridge (2011)
4. Babanin, A., Chalikov, D., Young, I., Savelyev, I.: Predicting the breaking onset of surface water waves. *Geophys. Res. Lett.* **34**, L07605 (2007)
5. Bacigaluppi, P., Ricchiuto, M., Bonneton, P.: A 1D stabilized finite element model for non-hydrostatic wave breaking and run-up Finite Volumes for Complex Applications VII-Elliptic. *Parabol. Hyperbolic Probl. Springer Proc. Math. Stat.* **78**, 779–790 (2014)
6. Bacigaluppi, P., Ricchiuto, M., Bonneton, P.: Implementation and evaluation of breaking detection criteria for a hybrid boussinesq model. *Water waves* **2**, 207–241 (2020)
7. Barthelemy, X., Banner, M.L., Peirson, W.L., Fedele, F., Allis, M., Dias, F.: On a unified breaking onset threshold for gravity waves in deep and intermediate depth water. *J. Fluid Mech.* **841**, 463–488 (2018)
8. Berchet, A., Simon, B., Beaudoin, A., Lubin, P., Rousseaux, G., Huberson, S.: Flow fields and particle trajectories beneath a tidal bore: A numerical study. *Int. J. Sediment Res.* **33**, 351–370 (2018)

9. Bestehorn, M., Tyvand, P.A.: Merging and colliding bores. *Phys. Fluids* **21**, 042107 (2009)
10. Bjørkavåg, M., Kalisch, H.: Wave breaking in Boussinesq models for undular bores. *Phys. Lett. A* **375**, 1570–1578 (2011)
11. Bjørkavåg, M., Kalisch, H., Khorsand, Z., Mitsotakis, D.: Legendre pseudospectral approximation of Boussinesq systems and applications to wave breaking. *J. Math. Study* **49**, 221–237 (2016)
12. Bona, J.L., Colin, T., Lannes, D.: Long wave approximations for water waves. *Arch. Ration. Mech. Anal.* **178**, 373–410 (2005)
13. Bona, J.L., Sun, S.M., Zhang, B.-Y.: A nonhomogeneous boundary-value problem for the Korteweg-de Vries equation posed on a finite domain. *Commun. Partial Differ. Equations* **28**, 1391–1436 (2003)
14. Brun, M.K., Kalisch, H.: Convective wave breaking in the KdV equation. *Anal. Math. Phys.* **8**, 57–75 (2018)
15. Choi, W.: Strongly nonlinear long gravity waves in uniform shear flows. *Phys. Rev. E* **68**, 026305 (2003)
16. Craig, W.: An existence theory for water waves and the Boussinesq and Korteweg-de Vries scaling limits. *Commun. Partial Differ. Equations* **10**, 787–1003 (1985)
17. Da Silva, A.T., Peregrine, D.H.: Nonsteady computations of undular and breaking bores. In *Coastal Engineering 1990*, pp. 1019–1032 (1991)
18. Derakhti, M., Banner, M.L., Kirby, J.T.: Predicting the breaking strength of gravity water waves in deep and intermediate depth. *J. Fluid Mech.* **848**, R2 (2018)
19. El, G.A., Grimshaw, R.H.J., Smyth, N.F.: Unsteady undular bores in fully nonlinear shallow-water theory. *Phys. Fluids* **18**, 027104 (2006)
20. El, G., Hoefer, M.: Dispersive shock waves and modulation theory. *Phys. D* **333**, 11–65 (2016)
21. Favre, H.: *Ondes de Translation*. Dunod, Paris (1935)
22. Gavriluk, S.L., Liapidevskii, V.Y., Chesnokov, A.A.: Spilling breakers in shallow water: applications to Favre waves and to the shoaling and breaking of solitary waves. *J. Fluid Mech.* **808**, 441–468 (2016)
23. Gurevich, A.V., Pitaevskii, L.P.: Nonstationary structure of a collisionless shock wave, *Sov. Phys. JETP* **38**, 291–297 (1974) [**Translation from Russian of A.V. Gurevich and L.P. Pitaevskii, Zh. Eksp. Teor. Fiz.** **65**, 590–604 (1973)]
24. Guyenne, P., Grilli, S.: Numerical study of three-dimensional overturning waves in shallow water. *J. Fluid Mech.* **547**, 361–388 (2006)
25. Hatland, S., Kalisch, H.: Wave breaking in undular bores generated by a moving bottom. *Phys. Fluids* **31**, 033601 (2019)
26. Hornung, H.G., Willert, C., Turner, S.: The flow field downstream of a hydraulic jump. *J. Fluid Mech.* **287**, 299–316 (1995)
27. Itay, U., Liberzon, D.: Lagrangian kinematic criterion for the breaking of shoaling waves. *J. Phys. Ocean.* **47**, 827–833 (2017)
28. Kalisch, H., Ricchiuto, M., Bonneton, P., Colin, M., Lubin, P.: Introduction to the special issue on breaking waves. *Eur. J. Mech. B Fluids* **73**, 1–5 (2019)
29. Khait, A., Shemer, L.: On the kinematic criterion for the inception of breaking in surface gravity waves: Fully nonlinear numerical simulations and experimental verification. *Phys. Fluids* **30**, 057103 (2018)
30. Kharif, C., Abid, M.: Whitham approach for the study of nonlinear waves on a vertically sheared current in shallow water. *Eur. J. Mech. B Fluids* **72**, 12–22 (2018)
31. Korteweg, D.J., de Vries, G.: On the change of form of long waves advancing in a rectangular channel and on a new type of long stationary wave. *Philos. Mag.* **39**, 422–443 (1895)
32. Lannes, D.: *The Water Wave Problem*. Mathematical Surveys and Monographs. vol. 188. American Mathematical Society, Providence (2013)
33. Lannes, D., Bonneton, P.: Derivation of asymptotic two-dimensional time-dependent equations for surface water wave propagation. *Phys. Fluids* **21**, 016601 (2009)
34. Lin, C., Kao, M.J., Yuan, J.M., Raikar, R.V., Wong, W.-Y., Yang, J., Yang, R.Y.: Features of the flow velocity and pressure gradient of an undular bore on a horizontal bed. *Phys. Fluids* **32**, 043603 (2020)
35. Lin, C., Kao, M.J., Yuan, J.M., Raikar, R.V., Hsieh, S.C., Chuang, P.Y., Syu, J.M., Pan, W.C.: Similarities in the free-surface elevations and horizontal velocities of undular bores propagating over a horizontal bed. *Phys. Fluids* **32**, 063605 (2020)
36. Lubin, P., Chanson, H.: Are breaking waves, bores, surges and jumps the same flow? *Environ. Fluid Mech.* **17**, 47–77 (2017)
37. Peregrine, D.H.: Calculations of the development of an undular bore. *J. Fluid Mech.* **25**, 321–330 (1966)

38. Richard, G., Gavriluk, S.: The classical hydraulic jump in a model of shear shallow-water flows. *J. Fluid Mech.* **725**, 492–521 (2013)
39. Roeber, V., Cheung, K.F., Kobayashi, M.H.: Shock-capturing Boussinesq-type model for nearshore wave processes. *Coast. Eng.* **57**, 407–423 (2010)
40. Senthilkumar, A., Kalisch, H.: Wave breaking in the KdV equation on a flow with constant vorticity. *Eur. J. Mech. B Fluids* **73**, 48–54 (2019)
41. Shatah, J., Walsh, S., Zeng, C.: Travelling water waves with compactly supported vorticity. *Nonlinearity* **26**, 1529 (2013)
42. Skogestad, J.O., Kalisch, H.: A boundary value problem for the KdV equation: Comparison of finite-difference and Chebyshev methods. *Math. Comput. Simul.* **80**, 151–163 (2009)
43. Soares Frazao, S., Zech, Y.: Undular bores and secondary waves-Experiments and hybrid finite-volume modelling. *J. Hydraul. Res.* **40**, 33–43 (2002)
44. Song, J.B., Banner, M.L.: On determining the onset and strength of breaking for deep water waves. Part I: unforced irrotational wave groups. *J. Physical Oceanogr.* **32**, 2541–2558 (2002)
45. Stansell, P., MacFarlane, C.: Experimental investigation of wave breaking criteria based on wave phase speeds. *J. Phys. Oceanogr.* **32**, 1269–1283 (2002)
46. Stuhlmeier, R.: Effects of shear flow on KdV balance - applications to tsunami. *Commun. Pure Appl. Anal.* **11**, 1549–1561 (2012)
47. Sturtevant, B.: Implications of experiments on the weak undular bore. *Phys. Fluids* **6**, 1052–1055 (1965)
48. Thomas, R., Kharif, C., Manna, M.: A nonlinear Schrödinger equation for water waves on finite depth with constant vorticity *Phys. Fluids* **24**, 127102 (2012)
49. Tian, Z., Perlin, M., Choi, W.: Evaluation of a deep-water wave breaking criterion. *Phys. Fluids* **20**, 066604 (2008)
50. Varing, A., Filipot, J.F., Grilli, S., Duarte, R., Roeber, V., Yates, M.: A new definition of the kinematic breaking onset criterion validated with solitary and quasi-regular waves in shallow water. *Coastal Engineering* **164**, 103755 (2021)
51. Whitham, G.B.: *Linear and nonlinear waves*. Wiley, New York (1974)
52. Wilkinson, D.L., Banner, M.L.: Undular bores. In 6th Australian Hydraulics and Fluid Mechanics Conference. Adelaide, Australia (1977)
53. Wu, C.H., Nepf, H.M.: Breaking criteria and energy losses for three-dimensional wave breaking. *J. Geophys. Res. Oceans* **107**, C10 (2002)
54. Yaosong, C., Guocan, L., Tao, J.: Non-linear water waves on shearing flows. *Acta Mech. Sin.* **10**, 97–102 (1994)
55. Yuan, J.-M., Chen, H., Sun, S.-M.: Existence and orbital stability of solitary-wave solutions for higher-order BBM equations. *J. Math. Study* **49**, 293–318 (2016)

Paper F

Lagrangian Measurements of Orbital Velocities in the Surf Zone

M. BJØRNESTAD, M. BUCKLEY, H. KALISCH, M. STRESSER, J. HORSTMANN,
H.G. FRØYSA, O.E. IGE, M. CYSEWSKI, R. CARRASCO-ALVAREZ
Geophysical Research Letters, revision submitted (2021).

Lagrangian Measurements of Orbital Velocities in the Surf Zone

M. Bjørnstad¹, M. Buckley², H. Kalisch¹, M. Streßer², J. Horstmann², H.G. Frøysa¹, O.E. Ige¹, M. Cysewski², R. Carrasco-Alvarez²

¹Department of Mathematics, University of Bergen, PO Box 7800, 5020 Bergen, Norway
²Institute of Coastal Ocean Dynamics, Helmholtz-Zentrum Hereon, 21502 Geesthacht, Germany

Key Points:

- Measurements of Lagrangian and Eulerian velocities are combined with pressure sensor data to explore wave properties in the surf zone
- Wave-by-wave oscillations of mean-water level exert a strong influence on mass transport in the fluid column
- The motion of Lagrangian tracers is well matched by dispersive long-wave theory

Corresponding author: Henrik Kalisch, henrik.kalisch@uib.no

Abstract

[Eulerian and Lagrangian measurements of orbital velocities in waves approaching a beach are analyzed with the goal of understanding the relative influence of wave-by-wave variations in mean-water level, waveheight and incipient wave breaking on mass transport properties of waves in the surf zone. It is shown quantitatively that elevated local mean-water level correlates positively with increased Lagrangian mass transport at the free surface. Eulerian ADV measurements in the fluid column suggest that the depth-integrated wave-by-wave mass transport also correlates positively with the local mean-water level, and is only weakly linked to waveheight and wave-breaking events.]

Plain Language Summary

A sea state is defined broadly by an average wave period and an average perceived (significant) waveheight, but waveheights and periods of individual waves may differ significantly from these average values. The differences between individual waves are exacerbated as the waves approach the shore and interact with the bottom topography in shallow water. In particular, the mean water level may vary from wave to wave. In the present study, particle tracers are used in connection with stereo imaging to study particle trajectories in waves approaching a beach. Particle positions and trajectories are found using data analysis of individual camera frames. In addition, fluid velocities are measured directly using Acoustic Doppler Velocimetry. It is found that the most significant factor in the overall horizontal fluid velocity and net transport of particles by an individual wave towards the beach is not the waveheight or period, but the local mean-water level, that is how the average wave elevation in a single wave is situated with respect to the sea bed.

1 Introduction

Mass transport induced by wave motion is a major factor in the formation of circulation patterns in the nearshore zone which in turn affect beach erosion and resedimentation (Inman & Brush, 1973; Masselink et al., 2014). It is generally thought that the main cause of nearshore circulation are energetic breaking waves which can lead to significant nearshore wave set-up (increased mean water level) and in connection with bathymetric features lead to undertow, edge waves and rip currents (Longuet-Higgins & Stewart, 1964; Putrevu & Svendsen, 1999; Svendsen, 2006; Castelle et al., 2016; Davidson-Arnott et al., 2019). It is also well known that localized variations in the mean-water level may develop in non-breaking waves through self-modulation of wave groups (Longuet-Higgins & Stewart, 1962), leading to *bound* infragravity waves which propagate in sync with the wave group. In bound infragravity waves, the trough of the envelope is generally aligned with a wave set-up (higher mean water level), while the crest of the envelope is aligned with a wave set-down (Longuet-Higgins & Stewart, 1962). During the shoaling process, the alignment of the crests may change, and a phase shift between the wave group and the corresponding wave envelope may develop (List, 1992; Masselink, 1995; Janssen et al., 2003; Battjes et al., 2004; Inch et al., 2017). In addition, wave set-down through shoaling and the subsequent wave set-up in breaking waves may create low-frequency waves propagating sea-ward from the surf zone (Tucker, 1950; Longuet-Higgins & Stewart, 1964; Buckley et al., 2018).

Oscillations of the mean-water level at frequencies below the gravity-wave band are known to be important for a number of coastal processes such as beach and dune erosion (Russell, 1993; van Thiel de Vries et al., 2008) and can influence wave set-up, the structure of rip currents and storm surges (Castelle et al., 2016). Recent field studies also suggest the existence of low-frequency oscillations in currents (Elgar & Raubenheimer, 2020) in the surfzone.

62 In recent work, the authors of (Calvert et al., 2019) showed how set-down in wave
 63 groups affect the orbital velocities in the fluid column. The main purpose of the present
 64 study is to highlight how oscillations in the mean-water level influence kinematic flow
 65 properties of waves and mass transport in the fluid column under field conditions. As
 66 opposed to time-averaged measurements over long periods, such as used for example in
 67 studies of sand transport (see (Russell, 1993; De Bakker, Brinkkemper, et al., 2016) and
 68 many other studies), in the present study measurements of instantaneous velocities are
 69 more appropriate as this allows us to study flow properties featured by *individual* waves
 70 in the surf zone. While laboratory studies in shallow water have confirmed some theo-
 71 retical predictions about infragravity wave formation and shoaling (Lin & Hwung, 2012)
 72 as well as particle motion in gravity waves (Chen et al., 2010; Umeyama, 2012) and wave
 73 groups (Calvert et al., 2019), wave-by-wave properties of orbital velocities and mass trans-
 74 port remain largely unexplored in the field.

75 In order to illuminate the details of flow properties in individual waves under field
 76 conditions, a measurement campaign was conducted at a beach on the island of Sylt, lo-
 77 cated off the German North Sea Coast near the border with Denmark. Wave poles with
 78 graduation were mounted at low tide, together with pressure sensors and an Acoustic
 79 Doppler Velocimeter (ADV). In addition, oranges were used as surface tracers in con-
 80 nection with a two-camera stereo imaging system which was able to track the surface
 81 tracers. According to (Sharifi et al., 2007), oranges are slightly buoyant, and are about
 82 97% submerged in seawater. As a result, they are only marginally affected by wind drag
 83 while at the same time being easily visible due to their orange color. Moreover, these trac-
 84 ers are naturally bio-degradable.

85 Analysis of the measurements showed strong variation in mean-water level between
 86 consecutive waves. A spectral analysis revealed that the infragravity signal had a well
 87 defined peak at 28.6s and a smaller sideband at 13.8s, and bound infragravity waves were
 88 dominant. As will be laid out presently, the changes in mean-water level from one wave
 89 to the next have major implications on the underlying fluid flow. Indeed, the local mean-
 90 water level has a pronounced effect on the orbital velocities in the fluid, and an elevated
 91 mean-water level leads to strong mass transport both at the free surface and also in the
 92 fluid column. In particular, it will be shown that the wave-by-wave variations in the mean
 93 water level have a stronger effect on flow properties in individual waves than changes in
 94 the waveheight or even the commencement of wave breaking.

95 2 Field measurements

96 The main measurement system in this study was a two-camera stereo imaging sys-
 97 tem, that was able to resolve the motions of buoyant surface tracers (oranges) at the wavy
 98 water surface within the surf zone. Additional supporting wind and wave data were ob-
 99 tained from a combination of both in situ and remote sensing measurement systems, in-
 100 cluding bottom-mounted pressure wave gauges, a bottom-mounted acoustic doppler ve-
 101 locimeter, optical bottom-mounted pole wave gauges, and drone imagery.

102 2.1 Stereo imaging system

103 A long-range, high resolution two-camera stereo imaging system was specifically
 104 developed for this study. A pair of 5MP, global shutter CMOS digital cameras (Victorem
 105 51B163-CX, IO Industries) were each fitted with a EF 200 mm f/2.8L lens. The two cam-
 106 eras were placed on the ridge overlooking the beach, at a distance of 35m from one an-
 107 other. The cameras were focused on a portion of water surface within the surf zone, lo-
 108 cated at a distance of approximately 150m from the cameras. They were triggered si-
 109 multaneously by a computer-controlled function generator (National Instruments PCIE
 110 6612). A sketch of the instrument set-up is provided in Figure 1. Stereo observations of
 111 the sea surface have been used previously with the purpose of describing wave motion

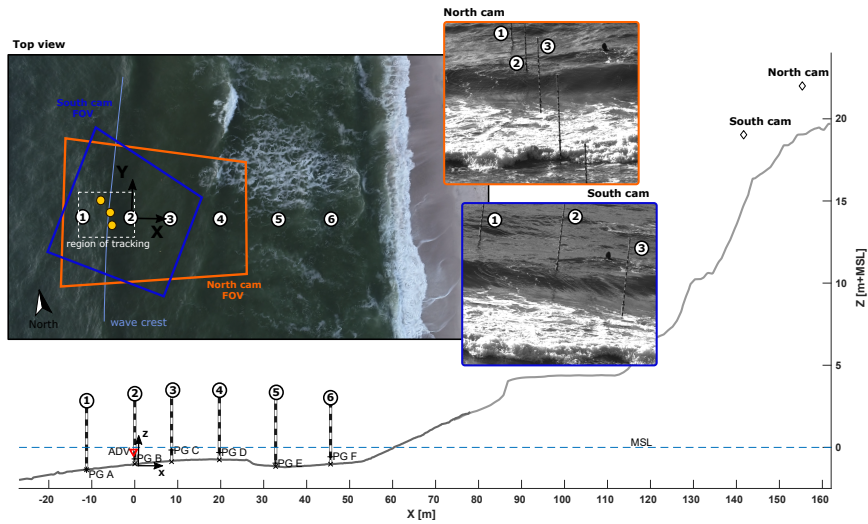


Figure 1. Experimental set-up: Six wave staffs were lined up in the direction of the incoming wavefield. Two cameras (North cam and South cam) were mounted on solid foundations atop dunes overlooking the beach. The two fields of view overlapped in a region including the first three wave staffs. Pressure sensors (PG) were mounted near the base of each pole. An Acoustic Doppler Velocimeter (ADV) was mounted at the sea bed near Pole 2.

112 offshore and in the surf zone (see (Benetazzo, 2006; de Vries et al., 2011; Benetazzo et
 113 al., 2012; Bergamasco et al., 2017) and references therein). Here, the cameras are used
 114 primarily for locating the orange tracers which simplifies the data analysis.

115 2.2 Supporting measurements

116 Six graduated aluminum poles were jettied into the sand of an intertidal sandbar
 117 at low tide. The array of poles was delineated at an angle of about 281° which made them
 118 approximately perpendicular to the crests of incoming waves, although there were some
 119 slight variations in the angles of the wave crests. The most seaward pole (Pole 1) was
 120 about 80m from the shore, and the closest pole (Pole 6) was about 20m from the shore-
 121 line. At the base of each pole, a pressure gauge measured absolute pressure at 10 Hz sam-
 122 pling frequency. The recorded pressure signal was subdivided into 7-10 minute data bursts
 123 and then transformed to surface excursion using the nonlinear, weakly dispersive method
 124 described in (Bonneton et al., 2018) (see also (Mouragues et al., 2019)). Since the gradu-
 125 ated poles were within the field of view of the stereo cameras (acquiring at 30 frames/second),
 126 these were also used as optical wave gauges.

127 At Pole 2, an upward looking, 6 MHz Nortek Vector Acoustic Doppler Velocimeter
 128 (ADV) was deployed and measured Eulerian flow velocities at a sampling rate of 64
 129 Hz. The elevation of the sensors with respect to the local datum as well the beach profile
 130 in the intertidal region was measured using an RTK-PDGPS. The elevation of the dry beach
 131 was extracted from photogrammetric digital elevation model (DEM), that was
 132 computed from airborne drone imagery using a DJI Matrice 210 RTK quadcopter.

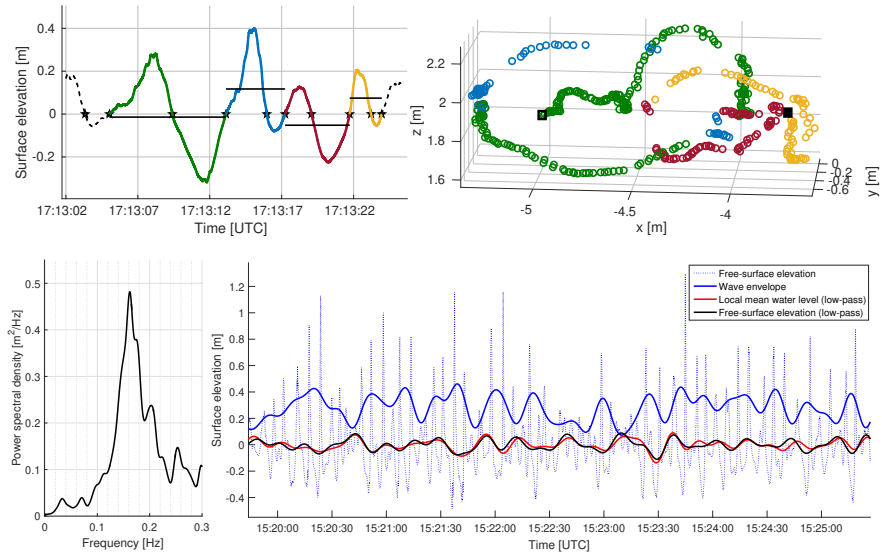


Figure 2. Upper left: Time series of free-surface elevation for non-breaking waves. The surface excursion is reconstructed from pressure data collected by pressure gauge mounted at the base of Pole 2. The black lines represent the average of the free surface elevation over the zero-crossing period. Upper right: Lagrangian motion of a particle tracer in the same time window as the free surface data in the left panel. The blue and yellow waves feature instantaneous wave set-up and corresponding strong shoreward Lagrangian transport while the red wave features set-down and backward drift. The black rectangle indicates the tracer position when tracking commenced, and the solid black square indicates the final tracer position. There are some gaps in the tracer positions in cases when the tracer was not visible in both cameras. Lower left: The power spectral density as a function of frequency. Lower right: The blue dashed curve is the free-surface elevation calculated from the pressure data measured by pressure gauge mounted at Pole 1 and with a lowpass Butterworth filter with a cutoff frequency of 0.075 Hz, the free-surface elevation is plotted as the black curve. The red curve represents the local mean water level obtained by zero-crossing analysis and the blue solid curve shows the wave envelope computed using the Hilbert transform (Janssen et al., 2003).

2.3 Experimental Procedure

Oranges were deployed by a swimmer near Pole 1. These tracers are slightly buoyant, so that they always stayed at the free surface, and were well visible in the image frames. Images were acquired at 30 frames/second from both cameras. The data used in this article were acquired between 17:00 and 17:30 UTC on the 7th of September, 2019. The sea state was characterized by records from a buoy moored 1km offshore in depth of 10m which showed 1m significant waveheight and 7s peak period. The incoming wavefield had a peak direction of 284.17° , and the mean wind speed was approximately 5 m/s from NNW.

2.4 Data analysis

In order to obtain the intrinsic and extrinsic parameters for the two 200mm cameras, a stereo camera calibration was conducted with the Matlab toolbox Stereo Camera Calibrator. The calibration result was validated with distances estimated using both pole graduations and the stereo imaging system. The root mean squared (RMS) difference for time series at Pole 1 obtained by pole graduation and by the stereo camera system is found to be less than 0.015m.

Pairs of individual frames from camera footage were examined visually, and orange positions were recorded. A triangulation with the input of the stored pixel positions together with the calibration parameters was then done to construct 3D world-coordinate points. In order to create an appropriate coordinate system, a reasonable assumption is to assume that the crests are perpendicular to the line of poles such as indicated in Figure 1. A horizontal vector was found by using two known GPS-positions at Pole 2 and Pole 3, and with this a vertical vector along Pole 2 was found. With the described vectors, a 3D coordinate system can be created where the origin is placed at the bottom of Pole 2, the x -axis is pointing along the poles towards the beach, the y -axis is pointing along the wave crests and the z -axis is pointing upwards. With the three orthogonal basis vectors, the orange positions are placed in the described coordinate system and then projected onto the xz -plane.

Several Lagrangian trajectories are plotted together with free-surface elevation at the nearest wave pole in Figure 2. The full three-dimensional paths are plotted in the right panel, but for the purpose of analyzing the cross-shore movement, these paths are projected into the xz -plane. The waveheight of the waves can be gauged from the left panel of Figure 2. For example for the wave indicated with blue, the waveheight is $H = 0.48\text{m}$. Since the distance between the poles is known, the wavelength can be calculated from the phase velocity and period to be 21.2m. For the wave indicated in red, the waveheight is $H = 0.35\text{m}$, and the wavelength is 17.6m. From Figure 2, it can be seen that the particle drift during one wave cycle is strongly correlated to the mean-water level in one wave. Indeed, the wave colored in green has a slight set-down, i.e. the mean level is $\bar{\eta}_0 = -0.014\text{m}$, and the net displacement of the tracer as shown in the right panel of Figure 2 is -0.30m . For the blue wave, the mean level is $\bar{\eta}_0 = 0.117\text{m}$, and the net cross-shore displacement is 1.23m. Similarly, the red wave features a negative mean level and a negative net displacement while the yellow wave features a positive mean level and a positive net displacement. The relation between mean water level and net drift will be quantified using a complete wave record below.

In the lower left panel of Figure 2 the two spectral peaks at 28.6s and 13.8s are clearly visible. A representative 5-minute window of the wave record is shown in the lower right panel of Figure 2. The wave group structure is visible though it is somewhat irregular. Nevertheless, the wave envelope (shown in solid blue) has the property that the troughs are approximately aligned with the peaks of the mean-water level (shown in red), and the peaks are approximately aligned with the troughs of the mean-water level. This is what is expected from theoretical studies and laboratory experiments (Longuet-Higgins & Stewart, 1962; Calvert et al., 2019).

3 Discussion

In the present work, Lagrangian particle paths in individual waves in the surf zone were recorded. As shown in the previous section, the data acquisition methods and data processing procedures utilized in this study resulted in highly accurate measurements of the tracer positions. In order to better understand the observed in situ particle paths, comparisons with a theoretical wave model were performed. At present, only the cross-shore movement is analyzed, and the data points are projected as described above.

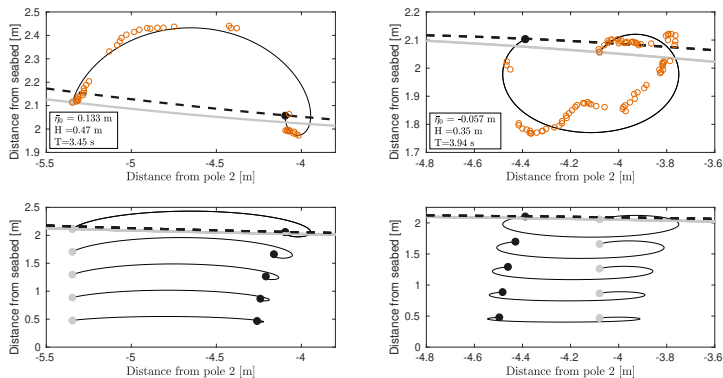


Figure 3. Comparison between measured particle trajectories using buoyant tracers, and particle trajectories in the nonlinear KdV approximation for the blue wave (left panels) and red wave (right panels) from Figure 2. The orange circles indicate the measured tracer positions. The thin black solid lines represent numerically computed particle paths with the gray dot representing the initial tracer position used in the comparison, and the black dot representing the final computed particle position. The gray thick lines represent the free surface in the KdV approximation at the start of the comparison, and the black dashed lines represent the free surface in the KdV approximation at the final time. Strong net shoreward transport throughout the fluid column is observed in the left panel while slight seaward transport is observed in the right panel.

191 Typical wavelengths λ in the datasets considered here are in the range from 10 meters
 192 to about 40 meters, and waveheights H for non-breaking waves range from 0.2m to
 193 about 1m, though as can be seen in the upper left panel in Figure 4, most non-breaking
 194 waves in the record considered there have a waveheight below 0.7m. Given that the
 195 local water depth h_0 was on the order of 2 meters, the Ursell number defined by $\mathcal{U} = H\lambda^2/h_0^3$
 196 at the measurement location is generally larger than 5, and for such values, nonlinear
 197 theory should be used (Dingemans, 1997). There are many numerical models used in coastal
 198 modeling of shoaling waves, most of which use some form of the Boussinesq equations
 199 (see for example (Roeber et al., 2010)). In the present case, we are interested in particle
 200 motion and orbital velocities in the fluid at a fixed site and for waves traveling to-
 201 wards the shore, and we therefore choose the Korteweg-de Vries (KdV) equation

$$\eta_t + \left(c_0 + \frac{3}{2} \frac{c_0}{h_0} \eta\right) \eta_x + \frac{1}{6} c_0 h_0^2 \eta_{xxx} = 0, \quad (1)$$

202 where h_0 is the local water depth, and $c_0 = \sqrt{gh_0}$ is the limiting long-wave speed. This
 203 equation is the simplest nonlinear shallow-water equation which also incorporates dis-
 204 persive effects. Assuming long-crested waves, a cross-section (such as along the measure-
 205 ment poles) of the free surface can be expressed for one period as

$$\eta(x, t) = f_2 - (f_2 - f_1) \operatorname{cn}^2\left(2K(m)\left(\frac{t}{T} - \frac{x}{\lambda}\right), m\right), \quad (2)$$

206 where f_1 , f_2 and f_3 are three parameters that can be chosen arbitrarily, m is the elliptic
 207 modulus defined by $m = \frac{f_1 - f_2}{f_1 - f_3}$, and $K(m)$ is an elliptic integral¹. The wavespeed

¹ $K(m)$ and $E(m)$ are the complete elliptic integrals of the first and second kind, (Lawden, 2013).

c, the wavelength λ and period T are then given by

$$c = c_0 \left(1 + \frac{f_1 + f_2 + f_3}{2h_0} \right), \quad \lambda = K(m) \sqrt{\frac{16h_0^3}{3(f_1 - f_3)}}, \quad T = \lambda/c. \quad (3)$$

In order to use these formulas in the current context to fit the wave-by-wave particle paths, it is convenient to take the waveheight H , the mean surface level $\bar{\eta}_0$ and the elliptic parameter m as the defining parameters. These are related to f_1 , f_2 and f_3 via the equations

$$f_3 = \bar{\eta}_0 - \frac{HE(m)}{mK(m)}, \quad f_1 = f_3 + \frac{H}{m}, \quad f_2 = f_1 - H. \quad (4)$$

This representation may be found in (Dingemans, 1997) for the case $\bar{\eta}_0 = 0$. Due to the oscillations of the mean-water level, it is essential in the present context to allow for non-zero η_0 . Note that the depth h_0 also appears in (3), but can be removed by dimensional analysis.

The procedure used to obtain comparisons with the field data can be summarized as follows. First, individual waves are identified using a zero-crossing segmentation of the wave field such as shown in the left panel of Figure 2. Since the waveheight is known from the data, we have to fit the parameters m and $\bar{\eta}_0$. In order to fit these parameters, we first need to compute particle paths associated with the solution (2). Taking the functions $\xi(t)$ and $\zeta(t)$ to describe the x -coordinate and z -coordinate, respectively, of a particle originally located at a point $(x, z) = (\xi_0, \zeta_0)$ given from the tracer position, the particle motion is described by the differential equations

$$\frac{\partial \xi}{\partial t} = u(\xi(t), \zeta(t), t), \quad \frac{\partial \zeta}{\partial t} = v(\xi(t), \zeta(t), t), \quad (5)$$

with initial conditions $\xi(0) = \xi_0$ and $\zeta(0) = \zeta_0$. As shown in (Borluk & Kalisch, 2012), the velocity field u, v can be written in terms of the free surface excursion η and various derivatives, and these equations can be solved numerically. The optimal parameters m and $\bar{\eta}_0$ are then found by minimizing the error between the tracer positions and the numerical simulations of the particle paths.

One feature which is clearly brought out by the black average bars in the upper left panel of Figure 2 and the mean-water level $\bar{\eta}_0$ computed for the waves shown in Figure 3 (left) is that strong forward transport coincides with elevated mean water level. In addition, the numerical approximations of particle paths further down in the fluid column shown in Figure 3, suggest that the local mean-water level affects transport properties not only near the free surface, but also farther down in the fluid column. Indeed, the two cases shown in Figure 3, clearly show the difference in average horizontal velocities for a wave with set-down, and a wave with set-up. The large particle drift at all depths which can be seen in the numerical simulations of the wave with positive set-up (lower left panel of Figure 3) is a clear departure from the case of a breaking or pre-breaking wave which features strong forward transport near the free surface. Indeed, it has been observed in wave flume experiments and numerical simulations that wave breaking induces a slight backward drift at depths about halfway down from the surface (Harms & Schlurmann, 2005; Deike et al., 2017).

In order to ensure that this strong mass transport throughout the fluid column is not a theoretical artifact, we analyzed data from ADV current measurements which are about 1m below the free surface. Usually, ADV measurements are taken near the bottom in order to study sediment transport and undertow. In the present case, the ADV was pointing upwards in order to capture the flow velocity in the center of the fluid column.

As mentioned above, time series of the free surface at poles 1, 2 and 3 were reconstructed from pressure gauge data using a nonlinear weakly dispersive approximation

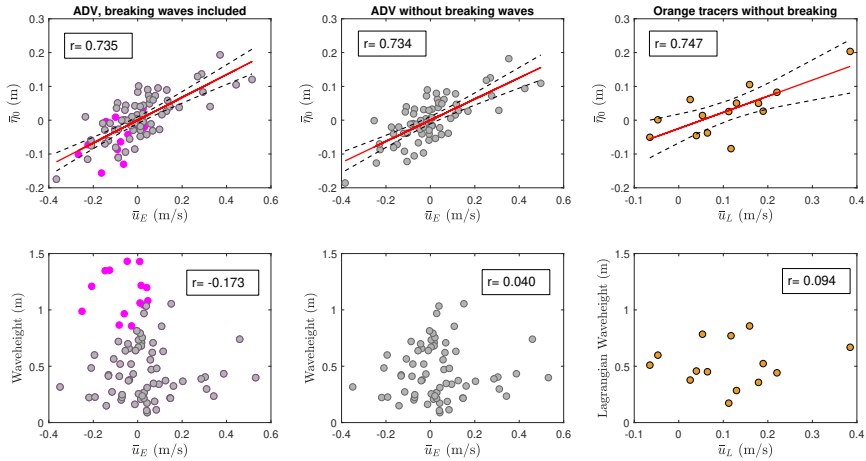


Figure 4. Upper panels: Correlation between wave-by-wave values of mean free surface elevation $\bar{\eta}_0$ and mean Eulerian velocity including breaking waves (left, $r=0.735$), mean Eulerian velocity exclusive of breaking waves (center $r=0.734$), mean Lagrangian velocity at the free surface (right $r=0.747$). The red lines are the regression lines and the black dotted curves show the 95 % confidence interval for the regression line estimate. Lower panels: Correlation between waveheight and mean Eulerian velocity including breaking waves (left), mean Eulerian velocity exclusive of breaking waves (center), mean Lagrangian velocity at the free surface (right). Gray dots indicate Eulerian measurements in non-breaking waves, magenta dots indicate Eulerian measurements in waves which are spilling or breaking. Orange dots indicate Lagrangian measurements of orange tracers at the free surface (non-breaking).

introduced in (Bonneton et al., 2018) and termed SNL (shallow non-linear) approximation. Waves which were breaking or close to breaking were identified by visual inspection and flagged for possible exclusion. Data based on a representative 7–1/2-minute wave record are evaluated in Figure 4. As indicated by the scatter plot relating wave-by-wave mean water level and forward transport in Figure 4, the correlation between average Eulerian velocity \bar{u}_E during one wave period and mean-water level $\bar{\eta}_0$ is strong. In contrast, the correlation between the average Eulerian velocity and the waveheight H is weak. These numbers are nearly unchanged if breaking waves are excluded from the computations. The upper right panel of Figure 4 shows the correlation between wave-by-wave mean water level and average Lagrangian drift \bar{u}_L during one wave period. The strong correlation of about 0.75 between $\bar{\eta}_0$ and \bar{u}_L represents quantitative confirmation of the dependence of the mass transport in the fluid column on the local mean-water level which was indicated in Figure 3 for a particular case.

It is clear from the analysis provided here that short-term oscillations in the wave set-up may constitute a significant factor in shoreward mass transport. In contrast, the waveheights of the individual waves were not found to be a good indicator of shoreward mass transport either at the free surface or otherwise.

In addition to affecting shoreward mass transport, it is possible that the observed oscillations of the mean-water level also constitute a mechanism for infragravity wave dissipation as the higher orbital velocities may facilitate wave breaking in waves with relatively smaller waveheight and wave celerity. Infragravity wave dissipation may be at-

273 tributed to bottom friction, transfer of energy to shorter waves through quadratic cou-
 274 pling, direct infragravity wave self-interaction resulting in steepening and the eventual
 275 breaking and bore formation (Battjes et al., 2004; Van Dongeren et al., 2007; Rijnsdorp
 276 et al., 2015; De Bakker, Tissier, & Ruessink, 2016).

277 The close correlation between Lagrangian velocities at the free surface and oscil-
 278 lations of the mean water level observed here suggest that dissipation of infragravity waves
 279 may also be achieved by gravity-wave breaking and subsequent smearing out of the in-
 280 infragravity wave field by broken shorter waves. Indeed, the increased Lagrangian veloc-
 281 ity at the free surface can be easily seen to facilitate short wave breaking in view of the
 282 the kinematic criterion for wave breaking (see (Itay & Liberzon, 2017; Hatland & Kalisch,
 283 2019) and references therein). Unfortunately, the size of the FOV of the stereo camera
 284 system and the length of the array of wave poles and pressure sensors did not provide
 285 spatial extent to test this hypothesis. In fact, decay and reflection of infragravity waves
 286 is highly dependent on environmental characteristics such as beach slope, sand bar struc-
 287 ture, and many other factors (Bertin et al., 2018), and a precise understanding of this
 288 hypothesis will require future field campaigns on a variety of beach profiles and wave con-
 289 ditions as well as laboratory experiments.

290 Acknowledgments

291 We thank Jan Bödewadt, Jurij Stell, and Lennart Zorn for technical support. We acknowl-
 292 edge funding from the Research Council of Norway under grant no. 239033/F20, from
 293 the Coasts in the Changing Earth System (PACES II) program of the Helmholtz Asso-
 294 ciation, and support from the Deutsche Forschungsgemeinschaft (DFG, German Research
 295 Foundation, project number 274762653, Collaborative Research Centre TRR 181 *En-
 296 ergy Transfers in Atmosphere and Ocean*).

297 We would also like to thank two anonymous reviewers whose constructive criticism
 298 helped us improve the paper significantly.

299 Wave buoy data and data of particle trajectories acquired during this study are avail-
 300 able for public access at <https://zenodo.org/record/5211265>

301 References

- 302 Battjes, J., Bakkenes, H., Janssen, T., & van Dongeren, A. R. (2004). Shoaling of
 303 subharmonic gravity waves. *Journal of Geophysical Research*, *109*(C2).
 304 Benetazzo, A. (2006). Measurements of short water waves using stereo matched im-
 305 age sequences. *Coastal engineering*, *53*(12), 1013–1032.
 306 Benetazzo, A., Fedele, F., Gallego, G., Shih, P.-C., & Yezzi, A. (2012). Offshore
 307 stereo measurements of gravity waves. *Coastal Engineering*, *64*, 127–138.
 308 Bergamasco, F., Torsello, A., Sclavo, M., Barbariol, F., & Benetazzo, A. (2017).
 309 Wass: An open-source pipeline for 3d stereo reconstruction of ocean waves.
 310 *Computers & Geosciences*, *107*, 28–36.
 311 Bertin, X., De Bakker, A., Van Dongeren, A., Coco, G., Andre, G., Arduin, F.,
 312 ... others (2018). Infragravity waves: From driving mechanisms to impacts.
 313 *Earth-Science Reviews*, *177*, 774–799.
 314 Bonneton, P., Lannes, D., Martins, K., & Michallet, H. (2018). A nonlinear weakly
 315 dispersive method for recovering the elevation of irrotational surface waves
 316 from pressure measurements. *Coastal Engineering*, *138*, 1–8.
 317 Borluk, H., & Kalisch, H. (2012). Particle dynamics in the kdv approximation. *Wave
 318 Motion*, *49*(8), 691–709.
 319 Buckley, M. L., Lowe, R. J., Hansen, J. E., van Dongeren, A. R., & Storlazzi, C. D.
 320 (2018). Mechanisms of wave-driven water level variability on reef-fringed
 321 coastlines. *Journal of Geophysical Research: Oceans*, *123*(5), 3811–3831.
 322 Calvert, R., Whittaker, C., Raby, A., Taylor, P. H., Borthwick, A., & Van Den Bre-
 323 mer, T. (2019). Laboratory study of the wave-induced mean flow and set-down

- 324 in unidirectional surface gravity wave packets on finite water depth. *Physical*
 325 *Review Fluids*, 4(11), 114801.
- 326 Castelle, B., Scott, T., Brander, R., & McCarroll, R. (2016). Rip current types, cir-
 327 culation and hazard. *Earth-Science Reviews*, 163, 1–21.
- 328 Chen, Y.-Y., Hsu, H.-C., & Chen, G.-Y. (2010). Lagrangian experiment and solution
 329 for irrotational finite-amplitude progressive gravity waves at uniform depth.
 330 *Fluid dynamics research*, 42(4), 045511.
- 331 Davidson-Arnott, R., Bauer, B., & Houser, C. (2019). *Introduction to coastal pro-*
 332 *cesses and geomorphology*. Cambridge university press.
- 333 De Bakker, A., Brinkkemper, J., Van der Steen, F., Tissier, M., & Ruessink, B.
 334 (2016). Cross-shore sand transport by infragravity waves as a function of
 335 beach steepness. *Journal of Geophysical Research*, 121(10), 1786–1799.
- 336 De Bakker, A., Tissier, M., & Ruessink, B. (2016). Beach steepness effects on non-
 337 linear infragravity-wave interactions: A numerical study. *Journal of Geophysi-*
 338 *cal Research: Oceans*, 121(1), 554–570.
- 339 Deike, L., Pizzo, N., & Melville, W. K. (2017). Lagrangian transport by breaking
 340 surface waves. *Journal of Fluid Mechanics*, 829, 364–391.
- 341 de Vries, S., Hill, D., De Schipper, M., & Stive, M. (2011). Remote sensing of surf
 342 zone waves using stereo imaging. *Coastal Engineering*, 58(3), 239–250.
- 343 Dingemans, M. W. (1997). *Water wave propagation over uneven bottoms* (Vol. 13).
 344 World Scientific.
- 345 Elgar, S., & Raubenheimer, B. (2020). Field evidence of inverse energy cascades in
 346 the surfzone. *Journal of Physical Oceanography*, 50(8), 2315–2321.
- 347 Harms, J., & Schlurmann, T. (2005). Time-variant mass transport beneath breaking
 348 waves. In *Coastal engineering 2004: (in 4 volumes)* (pp. 441–453). World Sci-
 349 entific.
- 350 Hatland, S. D., & Kalisch, H. (2019). Wave breaking in undular bores generated by
 351 a moving weir. *Physics of Fluids*, 31(3), 033601.
- 352 Inch, K., Davidson, M., Masselink, G., & Russell, P. (2017). Observations of
 353 nearshore infragravity wave dynamics under high energy swell and wind-wave
 354 conditions. *Continental Shelf Research*, 138, 19–31.
- 355 Inman, D. L., & Brush, B. M. (1973). The coastal challenge. *Science*, 181(4094),
 356 20–32.
- 357 Itay, U., & Liberzon, D. (2017). Lagrangian kinematic criterion for the breaking of
 358 shoaling waves. *Journal of Physical Oceanography*, 47(4), 827–833.
- 359 Janssen, T., Battjes, J., & Van Dongeren, A. (2003). Long waves induced by
 360 short-wave groups over a sloping bottom. *Journal of Geophysical Research*,
 361 108(C8).
- 362 Lawden, D. F. (2013). *Elliptic functions and applications* (Vol. 80). Springer Science
 363 & Business Media.
- 364 Lin, Y.-H., & Hwung, H.-H. (2012). Infra-gravity wave generation by the shoaling
 365 wave groups over beaches. *China Ocean Engineering*, 26(1), 1–18.
- 366 List, J. H. (1992). A model for the generation of two-dimensional surf beat. *Journal*
 367 *of Geophysical Research: Oceans*, 97(C4), 5623–5635.
- 368 Longuet-Higgins, M. S., & Stewart, R. (1962). Radiation stress and mass trans-
 369 port in gravity waves, with application to surf beats. *Journal of Fluid Mechan-*
 370 *ics*, 13(4), 481–504.
- 371 Longuet-Higgins, M. S., & Stewart, R. (1964). Radiation stresses in water waves; a
 372 physical discussion, with applications. In *Deep sea research and oceanographic*
 373 *abstracts* (Vol. 11, pp. 529–562).
- 374 Masselink, G. (1995). Group bound long waves as a source of infragravity energy in
 375 the surf zone. *Continental Shelf Research*, 15(13), 1525–1547.
- 376 Masselink, G., Hughes, M., & Knight, J. (2014). *Introduction to coastal processes*
 377 *and geomorphology*. Routledge.

- 378 Mouragues, A., Bonneton, P., Lannes, D., Castelle, B., & Marieu, V. (2019). Field
 379 data-based evaluation of methods for recovering surface wave elevation from
 380 pressure measurements. *Coastal Engineering*, *150*, 147–159.
- 381 Putrevu, U., & Svendsen, I. A. (1999). Three-dimensional dispersion of momentum
 382 in wave-induced nearshore currents. *European Journal of Mechanics-B/Fluids*,
 383 *18*(3), 409–427.
- 384 Rijnsdorp, D. P., Ruessink, G., & Zijlema, M. (2015). Infragravity-wave dynamics
 385 in a barred coastal region, a numerical study. *Journal of Geophysical Research:*
 386 *Oceans*, *120*(6), 4068–4089.
- 387 Roeber, V., Cheung, K. F., & Kobayashi, M. H. (2010). Shock-capturing boussinesq-
 388 type model for nearshore wave processes. *Coastal Engineering*, *57*(4), 407–
 389 423.
- 390 Russell, P. E. (1993). Mechanisms for beach erosion during storms. *Continental*
 391 *Shelf Research*, *13*(11), 1243–1265.
- 392 Sharifi, M., Rafiee, S., Keyhani, A., Jafari, A., Mobli, H., Rajabipour, A., & Akram,
 393 A. (2007). Some physical properties of orange [var. tompson]. *International*
 394 *Agrophysics*, *21*(4), 391–397.
- 395 Svendsen, I. A. (2006). *Introduction to nearshore hydrodynamics* (Vol. 24). World
 396 Scientific.
- 397 Tucker, M. (1950). Surf beats: Sea waves of 1 to 5 min. period. *Proceedings of*
 398 *the Royal Society of London. Series A. Mathematical and Physical Sciences*,
 399 *202*(1071), 565–573.
- 400 Umeyama, M. (2012). Eulerian–lagrangian analysis for particle velocities and tra-
 401 jectories in a pure wave motion using particle image velocimetry. *Philosophical*
 402 *Transactions of the Royal Society A: Mathematical, Physical and Engineering*
 403 *Sciences*, *370*(1964), 1687–1702.
- 404 Van Dongeren, A., Battjes, J., Janssen, T., Van Noorloos, J., Steenhauer, K., Steen-
 405 bergen, G., & Reniers, A. (2007). Shoaling and shoreline dissipation of low-
 406 frequency waves. *Journal of Geophysical Research: Oceans*, *112*(C2).
- 407 van Thiel de Vries, J. S. M., Van Gent, M., Walstra, D., & Reniers, A. (2008). Anal-
 408 ysis of dune erosion processes in large-scale flume experiments. *Coastal Engi-*
 409 *neering*, *55*(12), 1028–1040.



Graphic design: Communication Division, UIB / Print: Skjipes Kommunikasjon AS



uib.no

ISBN: 9788230851920 (print)
9788230851074 (PDF)